INVESTIGATING IMPACTS OF MODEL HORIZONTAL RESOLUTION ON SEA SURFACE TEMPERATURE BIASES AND OCEAN HEAT UPTAKE PROJECTIONS

A Dissertation

by

GAOPENG XU

Submitted to the Graduate and Professional School of
Texas A&M University
in partial fulfillment of the requirements for the degree of

DOCTOR OF PHILOSOPHY

Chair of Committee,	Ping Chang
Co-Chair of Committee,	Lixin Wu
Committee Members,	Ramalingam Saravanan
	Achim Stössel
Head of Department,	Shari Yvon-Lewis

May 2022

Major Subject: Oceanography

ABSTRACT

Impact of model horizontal resolution on sea-surface temperature (SST) biases and ocean heat uptake (OHU) projections are studied by comparing high-resolution (HR) and low-resolution (LR) Community Earth System Model (CESM) multi-century simulations.

Results indicate that except over the eastern boundary upwelling systems SST is warmer in HR than LR. Globally averaged SST is 1^{o}C warmer in HR than LR which is mainly attributed to stronger nonlocal vertical mixing and solar heat flux. The impact of nonlocal vertical mixing prevails over solar heat flux in eddy-active regions. In the tropics, nonlocal vertical mixing and solar heat flux contribute equally to the warmer SST in HR. The stronger nonlocal mixing in HR can be attributed to both the surface heat flux and shape function used in the nonlocal vertical mixing parameterization, and these two show a nonlinear relationship. The stronger solar heat flux in HR is mainly caused by less clouds in the tropics. The improved western boundary currents in HR also contribute to the reduction of SST biases in eddy-active regions.

The full-depth integrated OHU in HR and LR show small differences while vertical distributions of OHU are different. HR shows larger OHU in the upper 250 m than LR, but weaker OHU below 250 m. This difference is largely blamed to the difference in the eddy induced vertical heat transport (EVHT) between HR and LR. Moreover, the parameterized EVHT in LR is found to be more sensitive to the ocean stratification changes than the resolved EVHT in HR. The stronger OHU in the upper

250 m in HR is found to be distributed to the north of 35^{o}S (NR). To the south of 35^{o}S, OHU in HR is less than LR from the surface to seafloor which is attributed to the difference in the mean-flow induced meridional heat transport (MMHT) changes across 35^{o}S in the Indian Ocean. Compared with the difference in gyre circulation changes between HR and LR, the difference in the meridional overturning circulation changes shows a dominant contribution to the difference in MMHT changes in the Indian Ocean. In the upper 250 m, the Arctic can explain 26.32% of OHU difference in NR between HR and LR although the volume only accounts for 4% of that of NR. The difference in Arctic OHU is caused by the difference of MHT changes across 65^{o}N between HR and LR.

Overall, this study sheds new light on how resolved ocean eddy processes in HR and parameterized eddy processes in LR contribute differently to modeling SST and OHU. These new results can have important implications to improve simulations and projections of future climate change.

ACKNOWLEDGEMENTS

I would like to express my heartfelt gratitude to my advisor, Dr. Ping Chang, for his invaluable encouragement and guidance in my academic and research work. I am always inspired by his rigorous academic attitude, broad knowledge, and perceptive insight into the science from the past to the future. Without Dr. Ping Chang, I cannot finish this dissertation and achieve the full transition from a mathematician to a physical oceanographer. I would also like to thank my Co-Chair, Dr. Lixin Wu, as well as my committee members Dr. Ramalingam Saravanan and Dr. Achim Stössel for their solid supports.

I would like to thank my classmates, Qiuying Zhang and Xiaoqing Liu. We three became friends after we arrived in U.S. in 2016 and gained many wonderful memories in the past six years. I also want to thank Qiuying Zhang for teaching me to run CESM experiments on supercomputers. A special thank goes to Dr. Sanjiv Ramachandran who provided extremely helpful suggestions to my dissertation work. And to my colleagues Dr. Xue Liu, Dr. Dan Fu, Dr. Yun Liu, Dr. Jaison Kurian, Ms. Kelly Williams, Dr. Dapeng Li who have helped me in so many ways during my Ph.D. life in TAMU.

CONTRIBUTORS AND FUNDING SOURCES

Contributors

This work was supervised by a dissertation committee consisting of Professors Ping Chang (advisor), Lixin Wu (co-advisor) and Achim Stössel of the Department of Oceanography, and Professor Ramalingam Saravanan of the Department of Atmospheric Sciences.

The CESM data used in Chapter 2 and 3 were generated by iHESP and provided by Professor Ping Chang. The 2-D surface heat budget diagnostic tool used in Chapter 2 was provided by Dr. Stephen Yeager at NCAR.

All other work conducted for the dissertation was completed by the student independently.

Funding Sources

Graduate study was supported by a scholarship from China Scholarship Council.

NOMENCLATURE

AFC	Atmospheric flux convergence
CESM	Community Earth System Model
CNTL	1950-Control experiment
EBUS	Eastern boundary upwelling systems
EMHT	Eddy induced meridional heat transport
EVHT	Eddy induced vertical heat transport
GSE	Gulf Stream extension
HBLT	Boundary layer thickness
HF-TNST	1850 transient simulation
HR	High resolution model
KE	Kuroshio extension
KPP	K-profile parameterization
LR	Low resolution model
MHT	Meridional heat transport
MMHT	Mean-flow induced meridional heat transport
MVHT	Mean-flow induced vertical heat transport
OHTC	Ocean heat transport convergence
OHU	Ocean heat uptake
PI-CNTL	Preindustrial control simulation
PW	Petawatt

SPIN	spinup-1950 experiment
SST	Sea surface temperature
TW	Terawatt
VHT	Vertical heat transport
VHTC	Vertical heat transport convergence
VMFC	Vertical mixing flux convergence

TABLE OF CONTENTS

Page

LIST OF FIGURES

LIST OF TABLES

1. INTRODUCTION

1.1. Background

1.1.1. Sea-Surface Temperature in Climate Models

1.1.1.1. Sea-Surface Temperature Bias

Sea-surface temperature (SST) is the seawater temperature close to the atmosphere-ocean interface and is regarded as the key variable in reflecting air-sea interactions in the climate system (Joseph and Pillai, 1984; Lindzen and Nigam, 1987; Krishnamurti et al., 1988; Chang et al., 2000; Chelton et al., 2001; Alexander et al., 2002; Chang et al., 2006; O'Neill et al., 2012). SST is one of the best measured ocean variables, obtained by ships (Woodruff et al, 2005; Smith et al, 2019), mooring buoys (TAO/TRITON, PIRATA, RAMA), Argo floats, and satellites (Reynolds and Smith, 1994). To date, the quasi-global observation available to the public is from satellites since 1981 and Argo floats since 2006 (Roemmich et al., 2019) which help to understand the climate system in last four decades (Legeckis 1977; Cornillon, 1986; Bane et al., 1989; Xie et al., 2005; Small et al., 2008; Wang et al., 2012; Bishop et al., 2020).

SST is primarily determined by three physical processes: 1) oceanic advection driven by ocean circulations, 2) oceanic mixing associated with ocean turbulence, and 3) surface heat flux capturing the heat exchange between the atmosphere and ocean. With the limitation of equipment accuracy, it is still challenging to reconstruct the global observations of vertical seawater velocity with a magnitude order of 10^{-5} m/s near the surface (Liang et al., 2017), which is much weaker than the horizontal currents with an order of 1 m/s, implying the SST budget cannot be closed based only on observations. Therefore, numerical models, also named general circulation models (GCMs), become essential in studying physical processes associated with SST. Basically, numerical models aim to simulate the earth system by discretizing a set of partial differential equations, including Navier-Stokes momentum equation, tracer (temperature and salinity) equation, and continuity equation in both the atmosphere and ocean, where the sub-grid processes need to be parameterized based on the resolved processes (Smith et al., 2010; Eaton, 2012). The imperfections of such parameterizations lead simulated SST to deviate from the reality. The departure of simulated long-term mean SST from observations is defined as SST bias, which is the basic metric to evaluate model performance.

Beginning in 1995, the Coupled Models Intercomparison Project (CMIP) established a platform to compare simulated climate across different models (https://www.wcrp-climate.org/wgcm-cmip) playing a vital role in supporting IPCC Assessment Reports for climate variability and changes (Pachauri and Reisinger, 2008; Pachauri et al., 2014). Consistent climatological SST biases emerge across climate models in CMIP phase 5 (CMIP5) with ocean and atmosphere resolutions of ~1^o (referred to as low-resolution models (LR)), including significant warm biases in the eastern boundary upwelling systems (EBUS), Antarctic Circumpolar Current (ACC), east coast of the U.S. and Japan, and cold biases in tropics (also known as the cold tongue bias) and midlatitudes in the Northern Hemisphere.

1.1.1.2. Impacts of SST Bias on Climate Simulations

SST biases have a profound impact on climate simulations including present climate and future projections. El Niño-Southern Oscillation (ENSO), one of the most important climate variabilities due to the strong modulation on global precipitations (Ropelewski and Halpert, 1987; Wang et al., 2020), can be strengthened by the warm SST bias in the Southeast Pacific in climate models (Manganello and Huang, 2009). Meanwhile, the thermocline feedback associated with ENSO can be modified by the cold tongue bias (Xiang et al., 2012). Tropical cyclones are another natural system causing enormous economic losses (Emanuel 2017; Klotzbach et al., 2018), the global frequency of which is underestimated by CMIP5 models (Camargo, 2013). The under-representation of tropical cyclones in the Pacific is mainly caused by both warm SST bias in the Pacific and cold SST bias in the Atlantic, whereas that in the Atlantic is caused only by cold SST biases in the Atlantic alone (Hsu et al., 2019).

In addition to ENSO and tropical cyclones, the midlatitude stationary wave in the Southern Hemisphere can be affected by warm SST bias in the Tropical Pacific through erroneous double ITCZ (Garfinkel et al., 2020). In the Northern Hemisphere, the SST bias in the Gulf Stream region can excite Rossby waves in the troposphere (Lee et al., 2018). Furthermore, Bayr et al. (2019) suggested the cold tongue bias can modulate the precipitation over California through the atmospheric teleconnection. Additionally, Johnson et al., (2020) revealed the precipitation in the northern North America is modulated by the SST bias in the Tropical and North Pacific, while the precipitation in the southern North America is influenced by the Tropical Atlantic SST bias.

In terms of climate projections, it is found the cold tongue bias can lead to La Niña-like warming patterns in the future (Ying et al., 2020). Dutheil et al. (2020) revealed the biased warming pattern in the equatorial Pacific can reduce the reliability of tropical cyclone projections in the South Pacific. In addition, the projected atmospheric moisture content is significantly different in atmosphere models with and without SST bias correction (Ashfaq et al., 2010). Therefore, understanding the source of SST biases in models is vital to improve climate simulations and projections.

1.1.1.3. Origins of SST Bias

The understanding of origins of SST biases has been advanced in the recent decade. Gent and Yeager (2010) showed the importance of atmosphere resolution in reducing warm SST biases in EBUS by increasing the atmosphere resolution from 2^o to 0.5^o in the Community Climate System Model, version 3.5 (CCSM3.5). Following Gent and Yeager (2010), Small et al. (2015) confirmed the reduction of warm SST biases in CCSM4 with finer atmosphere resolutions (0.5^o, 1^o, 2^o), and suggested the reduction of SST biases is attributed to the improved coastal wind stress curl in EBUS through Sverdrup transport, which carries equatorial warm water to upwelling regions. The wind stress curl in 1^o and 2^o CCSM4 has broader coastal bands than in 0.5^o CCSM4, leading to the domination of Sverdrup transport in upwelling regions and therefore warmer SST (Small et al., 2015). Xu et al. (2014) also stated realistic coastal winds are essential to reduce SST biases in the southeastern Atlantic. A recent study by Kurian et al. (2021) demonstrated improvements in the magnitude and spatial structure of Benguela coastal low-level jet play a primary role in reducing SST bias in the upwelling region.

In contrast to the warm SST biases in EBUS, origins of cold SST biases in the tropics are still under debate. Some studies suggest the convection scheme in the atmosphere model is responsible for the tropical SST biases. Evidence shown in Song and Zhang (2009) revealed tropical SST biases are reduced after the convection schemes are modified in CCSM3. Li and Xie (2012) also argued tropical SSST biases are mainly attributed to the misrepresented cloud cover in CMIP3 and CMIP5 models. Woelfle et al. (2018) showed evidence the cold tongue bias is directly induced by the ocean advection which is associated with the surface wind while the surface wind is further sensitive to the convection schemes in Community Earth System Model version 1 (CESM1). On the other hand, some studies emphasize the role of oceanic processes in generating tropical SST biases. Vannière et al. (2014) proposed the remote origin of tropical SST biases which are advected into the tropics from the extratropics, and Burls et al. (2016) further showed it is the subtropical cell that brings cold SST biases to the tropics. Additionally, local processes are also responsible for the cold biases, such as the vertical advection, the displacement of isotherms, and vertical mixing (Siongco et al., 2020; Moum et al., 2013; Jia et al., 2015; Zhu and Zhang, 2018). A systematic study by Jia et al. (2015) illustrates the equatorial thermocline is sensitive to vertical diffusivity changes. Zhu and Zhang (2018) further presented the improvements of SST in the tropical Pacific after replacing the constant vertical background diffusivity with Argo-derived background diffusivity in coupled model, implying the importance of vertical mixing in reducing tropical SST biases. Moreover, the increased vertical resolution also helps to reduce the cold tongue bias in MITgcm, which is primarily through vertical mixing (Jia et al., 2021).

The investigation of SST biases in the midlatitudes remains scarce. Kirtman et al. (2012) showed SST in midlatitudes gets warmer after increasing ocean resolution from 1^{o} to 0.1^{o} with the same atmosphere resolution of 0.5^{o} in CCSM3.5. Small et al. (2014) performed high-resolution CESM simulations with atmosphere resolution of 0.25^{o} and ocean resolution of 0.1^{o} (hereafter HR), and found SST biases in western boundary current regions are substantially reduced compared with low-resolution CESM with ocean and atmosphere resolution of 1^{o} (hereafter LR). The ongoing High-Resolution Model Intercomparison Project (HighResMIP, Haarsma et al, 2016) as a part of CMIP6 is designed to shed further light on the impact of horizontal model resolutions on climate simulations. Models participated in HighResMIP have ocean resolution finer than 0.25^{o} and atmosphere resolution finer than 0.5^{o}. Gutjahr et al. (2019) conducted a suite of experiments using the Max Planck Institute Earth System Model (MPI-ESM1.2) for HighResMIP and showed increasing atmosphere resolution tends to decrease SST almost globally while increasing ocean resolution tends to increase SST everywhere except in the upwelling regions, which is consistent with previous CCSM and CESM studies (Gent and Yeager, 2010; Kirtman et al., 2012; Small et al., 2014; Small et al., 2015), as well as the Hadley Centre Global Environment Model 3 – Global Coupled version 3.1 (HadGEM3-GC3.1) (Roberts et al., 2019). However, the underlying mechanism for these SST changes in HR models is still unclear in the midlatitudes, especially in eddy-active regions, which is one of the main objectives to investigate in this dissertation.

1.1.2. Ocean Heat Uptake

1.1.2.1. Earth's Energy Budget

Figure 1.1 shows the energy budget averaged over Mar 2000 to May 2004 taken from Trenberth et al. (2009). Incoming solar radiation provides energy for life on Earth and acts as the driver of its climate system, while outgoing longwave radiation emits heat to the space. In an equilibrium climate, the absorbed incoming solar radiation, defined as the difference of incoming and reflected solar radiation, is necessarily balanced by the outgoing longwave radiation at the top of the atmosphere (TOA). The greenhouse gases including carbon dioxide (CO_2), methane (CH_4) and nitrous oxide (N_2O) can absorb the surface longwave radiation and reemit 93% of that back to the Earth surface, keeping the Earth warm in the equilibrium.

Since the Industrial Revolution, greenhouse gases continue to rise due to increased usage of fossil fuel. By 2011, CO_2 had increased to 390.5 parts per million (ppm) from 278 ppm in 1750 and Methane had increased to 1803 parts per billion (ppb) from 722 ppt in 1750 (Myhre et al., 2013), absorbing and reemitting back more surface longwave radiation, which has destroyed the equilibrium of the climate system causing TOA imbalance and therefore global warming (Manabe and Wetherald, 1975; Manabe and Stouffer, 1980; Taylor and Penner, 1994; Mitchell et al., 1995b; Mitchell et al., 1995a; Cox et al., 2000; Houghton et al., 2001). In the IPCC AR2, the agreement has been achieved on the surface temperature increasing since the beginning of twentieth century (Houghton, 1996).

1.1.2.2. Ocean Warming in Transient Climate

Based on observations, Levitus et al. (2000) first showed ocean subsurface warming is also associated with anthropogenic forcing (Barnett et al., 2005). With advancements in measurement techniques, studies confirmed the ocean warming in the upper 700 m (Lyman et al., 2010; Gleckler et al., 2012; Loeb et al., 2012). In the 21st century, more heat starts to gradually move to the deeper ocean (Purkey and Johnson, 2010; Chen and Tung, 2014; Cheng at al., 2017). With the large heat capacity and mass of seawater, 93% of the anthropogenic heat is stored in the ocean (Hoegh-Guldberg et al., 2014).

Ocean warming has profound impacts on different marine ecosystems, such as kelp forest (Smale, 2020) and coral reefs (Cantin et al., 2010; Bleuel et al., 2021). Studies show evidence that distributions of fish species have shifted poleward after ocean warming (Perry et al., 2005; Last et al., 2011; Vergés et al., 2016), becoming a critical challenge for fisheries and fish management worldwide (Link et al., 2011; Cheung et., 2010). In addition to ecological systems, sea level rise induced by global warming (Roemmich, 1992; Domingues et al., 2008; Levitus et al., 2012) is threatening coastal communities with flooding (Heberger et al., 2011; Woodruff et al., 2013; Buchanan et al., 2020), groundwater hazards (Befus et al., 2020), and coast erosion (Bruun., 1962; Leatherman et al., 2000; Reimann et al., 2018). Understanding and projecting ocean warming are both paramount to the study of climate systems.

1.1.2.3. Oceanic Processes Modulating Ocean Warming

Once the anthropogenic heat is injected into the ocean, the oceanic advection, working with diffusion, will redistribute the heat spatially. From a global average perspective, vertical heat transport (VHT) is a key process to move the absorbed heat into the deep ocean, and therefore balancing the heat budget (Griffies et al., 2015). Munk (1966) introduced the classical VHT model which represents the vertical advection-diffusion balance, including the upward advection and downward diffusion, yet it can only be applied to the interior ocean, not to the near surface ocean. A similar one-dimensional upwelling-diffusion ocean model was introduced by Hoffert et al. (1980) to emphasize the balance between the upwelling of cold water and heat diffusing from the surface to subsurface, however, this simple mechanism can be only properly applied to low-latitude ocean rather than the global ocean (Gregory, 2000).

As numerical modelling becomes more advanced, more details of VHT processes have been studied. In contrast to Munk (1966), Gregory (2000) found the global VHT balance is held by the downward heat advection and upward heat transport induced by the isopycnal mixing in a 3^{o} numerical model named HadCM2. As pointed out by Gnanadesikan et at. (2005), the downward VHT implies a negative buoyancy transport, indicating the horizontal pressure gradients are against mean flow. Geostrophic and frictional flows are impossible to be against pressure gradients because the former is perpendicular to pressure gradient by definition while the latter always goes from high pressure to low pressure. Therefore, the only possibility is the direct wind-driven flow which is also referred to Ekman flow. Ekman suction brings cold water upward whereas

Ekman pumping takes warm water downward, leading to a downward heat transport in the stratified ocean. In the deep ocean where Ekman suction and pumping are no longer important, the downward heat transport is mainly accomplished by meridional overturning circulation (Zika et al., 2013).

The upward heat transport induced by isopycnal mixing is associated with baroclinic mesoscale eddies with a horizontal scale of 50-300 kilometers (Gent and McWilliams, 1990; Gnanadesikan et al., 2015), and is regarded as the counter-gradient process because temperature is cold in the deeper ocean. They act to reduce the available potential energy by slumping isopycnals which are steepened by the lateral variations of mean VHT. Although numerical climate models have been improving rapidly for the past few decades, the majority of present generation models still cannot explicitly resolve oceanic mesoscale eddies due to the high computational costs. To include the physics of mesoscale eddies in non-eddy-resolving climate models, eddy-induced VHT (EVHT) needs to be parameterized based on background information. Gent-McWilliams sub-grid parametrization (GM90) was developed to represent mesoscale eddy fluxes in non-eddy-resolving climate models (Gent and McWilliams, 1990). It is shown that the VHT parameterized by GM90 in MOM3 is upward and dominates in the upper 1500 m (Gnanadesikan et at., 2005).

In addition to mesoscale eddies, submesoscale eddies (less than 50 kilometers) can produce upward EVHT in near-surface ocean with values larger than those of mesoscale eddies (Su et al. 2018). Siegelman et al. (2020) confirmed the upward submesoscale EVHT in the Antarctic Circumpolar Currents and demonstrated that it has a similar magnitude with the local air-sea heat fluxes. Fox-Kemper et al. (2008) proposed a parametrization of submesoscale EVHT generated by ageostrophic baroclinic instabilities in the mixed layer (hereafter, FK08).

Griffies et al. (2015) conducted three numerical experiments with explicitly resolved and GM90- and FK08-parameterized eddies in GFDL models. They found that, when averaged globally, the downward heat transport is dominated by mean VHT and diabatic mixing while the upward transport is accomplished through mesoscale, submesoscale EVHT and vertical nonlocal convection parameterized by K-profile parametrization (hereafter KPP, Large et al., 1994), consistent with Wolfe et al. (2008). Although these parameterizations have been effective in representing EVHT in non-eddy resolving climate models, Griffies et al. (2015) found that the magnitude of model resolved mesoscale EVHT increases while the parameterized submesoscale EVHT decreases as horizontal ocean model resolution increases from 1^o to $1/10^o$, implying the strong dependence of GM90 and FK08 on horizontal model resolutions, which can in turn affect vertical heat distribution.

Meridional heat transport (MHT), consisting of poleward MHT in the Indo-Pacific and northward MHT in the Atlantic, is another important process moving heat poleward, primarily through the wind-driven and thermohaline circulations, except between 40^oS and 50^oS where eddies are more important (Bryan, 1996; Phillips and Rintoul, 2000; Jayne and Marotzke, 2002; Yang et al., 2015). The poleward MHT reaches maximum in the subtropics in both hemispheres (Trenberth et al., 2019). Eddy-induced MHT (EMHT) in non-eddy resolving models is parameterized by GM90, the response of which to the doubled CO_2 forcing has the opposite sign with the resolved EVHT in Antarctic Circumpolar Current region (ACC) (Bryan et al., 2014). In the Atlantic, MHT is mainly driven by the Atlantic Meridional Overturning Circulation (AMOC). With finer horizontal model resolutions, AMOC and the related MHT tends to be stronger, as well as the decline in the future (Roberts et al., 2020), which can modulate the sea ice area in the Arctic (Docquier et al., 2019). More studies are needed to investigate the impacts of model resolutions on the heat redistributions through MHT.

1.2. Motivations and Objectives

High-resolution climate models are vital tools for studying mesoscale or submesoscale processes, as direct observations are very limited at these spatial scales. Recently, the Coupled Model Intercomparison Project 6 (CMIP6) endorsed a high-resolution modeling project called High Resolution Model Intercomparison Project (HighResMIP) (Haarsma et al., 2016). In HighResMIP, each participating model performed a short (30-50 years) spin-up experiment (SPIN) under a constant 1950 climate forcing condition. Then two 100-year experiments were branched from SPIN, with one 100-years control run (CTRL) under the same constant 1950 forcing and the other 100-year transient run (TNST) forced by the observed 1950-2014 historical forcing followed by a 2015-2050 Shared Socioeconomic Pathway (SSP) scenario forcing. Each model conducts at least two sets of simulations: a low-resolution (LR) and a high-resolution (HR) run. Motivated by the availability of these new simulations and the improvements of SST simulations shown in HR CESM (Small et al., 2014), MPI-ESM1.2 (Gutjahr et al., 2019), and HadGEM3-GC3.1 (Roberts et al., 2019), we will investigate the mechanisms modulating the improvements of SST simulations in HR CESM in Chapter II.

A set of high-resolution CESM simulations with a spin-up period of 250 years has recently been completed at the International Laboratory for High-Resolution Earth System Prediction (iHESP, Chang et al., 2020), consisting of a 500-year preindustrial control simulation and a 250-year transient climate simulation from 1850 to 2100 branched from year 250 in preindustrial control run and forced by historical forcing from 1850 to 2005 and RCP8.5 forcing from 2006 to 2100, having three ensembles in 1920-2100. These long simulations can help to address the concerns about potential model drifts in the short HighResMIP simulations and provide more reliable statistics in evaluating the role of VHT and MHT in climate change, which motivates us to investigate the following question in Chapter III: To What Extent Can Model Resolutions Affect the Heat Distribution Through VHT and MHT Under RCP8.5 Scenario Forcing?

Each Section will provide an introduction, data and method description, as well results and discussion. In the end of this dissertation, i.e., Chapter IV, we summarize the main findings and discuss the future work.

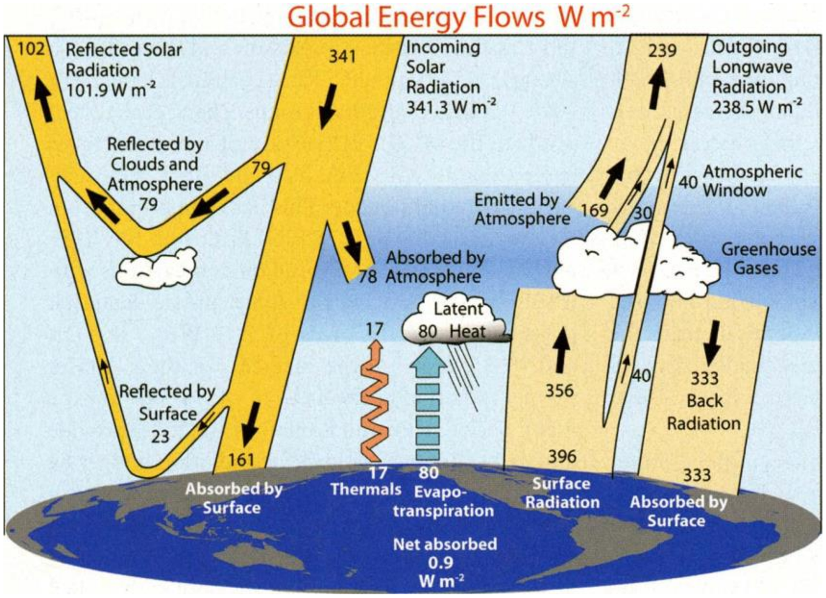

Figure 1.1 The global annual mean Earth’s energy budget from Mar 2000 to May 2004 taken from Trenberth et al. (2009).

2. IMPACT OF MODEL HORIZONTAL RESOLUTION ON MEAN SEA-SURFACE TEMPERATURE BIASES

2.1. Introduction

Sea-surface temperature (SST) is crucial to study the climate system since it is the key variable linking changes in the ocean to the atmosphere. For instance, Liu et al (2021) found that mesoscale SST anomalies in the northwestern Pacific can influence heavy rainfall in the western North America. SST anomalies associated with El Niño-Southern Oscillation (ENSO), Pacific Decadal Oscillation (PDO) and the Atlantic Multidecadal Oscillation (AMO) are all shown capable of modulating extreme weather globally (McPhaden et al, 2006; McCabe et al, 2004; Di Lorenzo and Mantua, 2016). SST is also among the best measured climate variable, obtained by ships (Woodruff et al, 2005; Smith et al, 2019), mooring buoys (TAO/TRITON, PIRATA, RAMA), Argo floats, and satellites (Reynolds and Smith, 1994).

Despite that these observations help to understand the climate system globally, it is still challenging to understand the physical process driving SST balance, such as, ocean mixing and advection, which are related to ocean circulations and eddy formations. Numerical models have therefore become extremely important tools to study mechanisms of maintaining SST and causes for its variability. SST bias defined as the departure of simulated long-term mean SST from the observations is an important metric to assess model performance. The Coupled Models Intercomparison Project (CMIP), which began in 1995, provides a platform to compare simulated climate across different models (https://www.wcrp-climate.org/wgcm-cmip). The climate models in CMIP phase

5 (CMIP5), most of which have ocean and atmosphere resolutions of ~1° (referred to as low-resolution models (LR)), show consistent biases in simulated climatological mean SST (Figure 1a). The biases can be divided into two groups: warm biases primarily occur in the eastern boundary upwelling systems (EBUS), Antarctic Circumpolar Current (ACC) region, east coast of the U.S. and Japan, and cold biases mainly occur in tropics (also known as the cold tongue bias) and midlatitudes in the Northern Hemisphere.

The impacts of SST biases on the simulated climate system have been extensively studied in recent decade (Ashfaq et al., 2011; Camargo, 2013; He and Soden, 2016; McGregor et al., 2018; Lee et al.,2018; Hsu et al., 2019; Johnson et al., 2020; Dutheil et al., 2020; Garfinkel et al., 2020). These studies show that climatological SST biases can strongly affect global precipitation distributions, as well as future projections of precipitation over ocean and land (Ashfaq et al., 2011; He and Soden, 2016; Johnson et al., 2020). In addition, tropical cyclone biases, including frequency, locations, and intensity, are largely impacted by SST in the Tropics (Camargo, 2013; Hsu et al., 2019; Dutheil et al., 2020). Hsu et al. (2019) found that warm biases in the Pacific and cold biases in the Atlantic both can lead to overrepresentation of tropical cyclones in the Pacific. McGregor et al. (2018) also suggested that SST biases in the Atlantic basin can affect the wind and surface temperature in the Pacific via atmospheric teleconnection. Furthermore, the warm SST bias in the tropical east Pacific tends to cause a biased midlatitude stationary wave in the Southern Hemisphere through erroneous double ITCZ (Garfinkel et al., 2020). Lee et al. (2018) demonstrated that the SST bias in Gulf Stream region can induce Rossby wave responses in the troposphere in the Northern Hemisphere. Moreover, Ying et al. (2019) revealed that cold biases in the central equatorial Pacific can lead to La Niña-like warming patterns. Therefore, understanding the source of SST biases in models is vital for improving climate simulations and projections.

Gent and Yeager (2010) showed that warm biases in EBUS have been significantly reduced after increasing the atmosphere resolution from 2^o to 0.5^o using Community Climate System Model, version 3.5 (CCSM3.5), pointing to the importance of atmosphere resolution in improving SST simulations in the upwelling regions. Xu et al. (2014) revealed that realistic coastal winds in the models are important to reduce SST biases in the southeastern Atlantic. Based on three CCSM4 experiments with different atmosphere resolutions (0.5^o, 1^o, 2^o), Small et al. (2015) showed that coastal wind stress curl is a dominant factor to reduce SST biases via Sverdrup transport in EBUS, which carries warm tropical water poleward. It is found that wind stress curl in 0.5^o CCSM4 has narrower coastal bands than that in 1^o and 2^o CCSM4, leading to stronger dominance of Sverdrup transport in 1^o and 2^o CCSM4 compared to 0.5^o CCSM4 (Small et al., 2015). Kurian et al. (2021) demonstrated that improving magnitude and spatial pattern of Benguela coastal low-level jet plays a primary role in reducing SST biases in Benguela upwelling region.

In contrast to the warm SST bias in EBUS, the source of cold SST biases in the tropics is still unclear. Song and Zhang (2009) found that SST biases are reduced after the convection schemes are modified in CCSM3, implying importance of atmosphere convection processes. Li and Xie (2012) also argued that misrepresented cloud cover may be the main source of tropical SST biases CMIP3 and CMIP5 models. Woelfle et al. (2018) presented evidence that the equatorial cold SST biases are directly generated by the anomalous ocean advection driven by surface wind, which is further sensitive to the underlying convection parameterization in Community Earth System Model version 1 (CESM1). On the other hand, Moum et al. (2013) proposed that vertical ocean mixing can also modulate SST biases in the equatorial Pacific. Moreover, Vannière et al. (2014) argued that the tropical cold SST biases are advected into the tropics from extratropics. Burls et al. (2016) further showed that it is the subtropical cell that brings cold SST biases to the tropics.

Studies of cold biases in the midlatitudes started in recent decade and still remain sparse. Kirtman et al. (2012) illustrated that CCSM3.5 generates warmer SST in the western boundary current regions and Southern Ocean after increasing ocean resolution from 1^o to 0.1^o with the same atmosphere resolution of 0.5^o. Small et al. (2014) performed high-resolution CESM simulations with atmosphere resolution of 0.25^o and ocean resolution of 0.1^o (hereafter HR), and found that SST biases in western boundary currents are substantially reduced compared with low-resolution CESM with ocean and atmosphere resolution of 1^o (hereafter LR). The reduced SST bias is mainly due to the finer ocean resolution (personal communication to Justin Small). The ongoing High-Resolution Model intercomparison Project (HighResMIP, Haarsma et al, 2016) as a part of CMIP6 is designed to shed further light on the impact of horizontal model resolutions on climate simulations. Models participated in HighResMIP have ocean resolution finer than 0.25° and atmosphere resolution finer than 0.5°. Gutjahr et al. (2019) conducted a suite of experiments using Max Planck Institute Earth System Model (MPI-ESM1.2) for HighResMIP and showed that increasing atmosphere resolution tends to decrease SST almost globally while increasing ocean resolution tends to increase SST everywhere except in the upwelling regions, which is consistent with previous CCSM and CESM studies (Gent and Yeager, 2010; Kirtman et al., 2012; Small et al., 2014; Small et al., 2015), as well as Hadley Centre Global Environment Model 3 – Global Coupled version 3.1 (HadGEM3-GC3.1) (Roberts et al., 2019). However, the underlying mechanism for these SST changes in HR models is still unclear in the midlatitude, especially in eddy-active regions.

LR and HR performed by International Laboratory of High-resolution Earth System Prediction (iHESP) contributed to HighResMIP (Roberts et al. 2020). Using these simulations, this study aims to investigate the processes that impact SST simulations in the tropics and midlatitudes in CESM by increasing model horizontal resolution. This paper is organized as follows. Models and method are described in Section 2. SST biases in HR models are shown in Section 3. Section 4 shows a surface ocean heat budget analysis in HR and LR followed by an analysis of ocean mixing and advection in Section 5. Summary and discussion are given in Section 6.

2.2. Model and Method

2.2.1. HighResMIP Simulations

In HighResMIP, ocean/sea-ice component models are all finer than 0.25 ° and atmosphere/land component models are all finer than 0.5 °. Among the eight participating models, there are six running at 0.25 ^{o} and two running at 0.1^{o} or finer (Table 2.1). Based on the protocol of HighResMIP, each of these models performed three simulations: (i) spinup-1950 (hereafter, SPIN) – a short (30-50 year) simulation starting from observed estimates of 3D ocean temperature and salinity dataset EN4.0 averaged over the period of 1950–1954 (Good et al., 2013), which provided initial conditions to both control-1950 (hereafter, CNTL) and hist-1950 (hereafter, TNST), (ii) CNTL – a 100-year continuation of SPIN with the same climate forcing in 1950, (iii) TNST – a 100-year simulation from 1950 to 2050 starting from the initial condition as CNTL but forced by the 1950-2014 historical forcing and 2015-2050 Shared Socioeconomic Pathway (SSP) 585 scenario forcing (details referred readers to Figure 1 in Roberts et al., 2019). The following analysis will be mainly based on CNTL to investigate climatological SST biases.

2.2.2. CESM

Given that we have access to full model output only from CESM but not from other models in HighResMIP, we will primarily analyze HR and LR to address our scientific questions. CESM1.3 is an open source fully coupled climate model developed by National Center for Atmospheric Research (NCAR). CESM1.3 is composed of the Community Atmosphere Model version 5 (CAM5, Neale et al., 2012), the Parallel Ocean Program version 2 (POP2, Danabasoglu et al., 2012; Smith et al., 2010), the Community Land Model version 4 (CLM4, Lawrence et al., 2011) and the Community Ice Code version 4 (CICE4, Hunke and Lipscomb, 2008). As in Small et al (2014), HR has a nominal resolution of 0.1^{o} for POP2 and CICE4 and 0.25^{o} for CAM5 and CLM4.

In POP2, vertical mixing is represented by K-Profile Parameterization (hereafter KPP, Large et al., 1994), which consists of local and nonlocal mixing components. For more detailed descriptions of CESM1.3, we refer the reader to earlier studies (Danabasoglu et al., 2012; Small et al., 2014; Chang et al., 2020).

LR is used for comparison with HR. LR has a standard horizontal resolution of 1o for all component models, where the mesoscale (50 km-300 km, Gent and McWilliams, 1990, hereafter, GM90) and submesoscale (less than 50 km, Fox-Kemper et al., 2008, hereafter, FK08) eddy tracer flux parameterizations are implemented in POP2. But GM90 and FK08 are turned off in HR CESM. However, the same KPP vertical mixing is used in both HR and LR.

Following the protocol of HighResMIP and the tuning process, the first 54 years are used as SPIN in HR. CNTL spans from year 55 to year 155 as the standard simulation period. A 5-year extension from year 156 to year 160 was added to the standard period to form a 106-year CNTL (Hereafter CNTL-HR). Unlike HR, only 30 years is used for SPIN in LR and CNTL is integrated from year 31 to year 131. To save the storage, only the first 20 years of SPIN output in HR (SPIN-HR) and LR (SPIN-LR) are saved. Note that both SPIN-HR and SPIN-LR start from the same EN4.0 dataset. Therefore, a comparison between SPIN-HR and SPIN-LR allows us to examine the difference in the development of SST biases in HR and LR.

Since 20-year output of SPIN-HR and SPIN-LR is quite short to study the development of the SST biases, we made another 106-year LR to compare directly with CNTL-HR. This simulation was initialized by 3-D temperature and salinity fields obtained from the first day of year 55 in CNTL-HR, and thus is referred to as CNTL-LR-HRIC. Note that CNTL-HR and CNTL-LR-HRIC have the same initial condition for temperature and salinity. Therefore, we can examine the development of SST biases by comparing CNTL-HR and CNTL-LR-HRIC.

2.2.3. Method

The temperature equation at a model grid can be written as

$$\frac{\partial T}{\partial t} = -\frac{\partial uT}{\partial x} - \frac{\partial vT}{\partial y} - \frac{\partial wT}{\partial z} + \frac{1}{c_P\rho}\frac{\partial Q}{\partial z} + \kappa_H\left(\frac{\partial^2}{\partial x^2} + \frac{\partial^2}{\partial y^2}\right)T + \frac{\partial}{\partial z}\kappa_z\left(\frac{\partial T}{\partial z} - \gamma_x\right), \qquad (2.1)$$

where T is potential temperature; u, v, and w are velocity along x, y, z axes; Q is the heat flux including solar and nonsolar component; c_P is the heat capacity taken as 3996 J/kg/°C; ρ is the density of sea water taken as 1026 kg/m^3; $\kappa_H$and κ_z are horizontal and vertical diffusivity where κ_H is spatially constant; γ_x represents nonlocal turbulent heat transport in KPP parameterization. As eddies are not resolved in LR, total heat transport (uT, vT, wT) is taken as the sum of resolved transport and parameterized transport by GM90 and FK08.

2.2.3.1. Surface Ocean Heat Budget

After integrating Eq.2.1 with time and depth from the surface to H=10 m, which is the first vertical layer in CESM, the evolution of SST can be expressed as

$$\frac{1}{H}\int_{-H}^{0} T(t) - T(0)\,dz = \frac{1}{H}\int_0^t\int_{-H}^{0}\left(-\frac{\partial uT}{\partial x} - \frac{\partial vT}{\partial y} - \frac{\partial wT}{\partial z}\right)dz\,dt + \frac{1}{H}\int_0^t \frac{Q_{net} - SW|_{-H}}{c_P\rho}\,dt +$$

$$\frac{1}{H}\int_0^t\int_{-H}^{0}\kappa_H\left(\frac{\partial^2}{\partial x^2} + \frac{\partial^2}{\partial y^2}\right)T\,dz\,dt - \frac{1}{H}\int_0^t \kappa_z\left(\frac{\partial T}{\partial z} - \gamma_x\right)_{-H} dt.$$

The equation of climatological mean SST is obtained as

$$\frac{1}{t_0 H}\int_0^{t_0}\int_{-H}^{0} T(t) - T(0)\, dz\, dt = \frac{1}{t_0 H}\int_0^{t_0}\int_0^{t}\int_{-H}^{0}\left(-\frac{\partial uT}{\partial x} - \frac{\partial vT}{\partial y} - \frac{\partial wT}{\partial z}\right) + \kappa_H\left(\frac{\partial^2}{\partial x^2} + \frac{\partial^2}{\partial y^2}\right) T dz\, ds\, dt + \frac{1}{t_0 H}\int_0^{t_0}\int_0^{t}\frac{Q_{net} - SW|_{-H}}{c_P \rho}\, ds\, dt + \frac{1}{t_0 H}\int_0^{t_0}\int_0^{t}\kappa_z\left(\frac{\partial T}{\partial z} - \gamma_x\right)_{-H} ds\, dt, \qquad (2.2)$$

where t_0 is the length of interested period. Since the long-term mean of horizontal mixing is generally quite small compared with other terms near surface, it will be lumped with the advection term together. Q_{net} is net surface heat flux including latent, sensible, longwave and shortwave heat flux at surface and positive denotes the heat into the ocean. $SW|_{-H}$ represents penetrative shortwave flux at z=-H. Since each term in Eq.2.2 is only a function of latitude and longitude, the balance in Eq.2.2 will be referred to as 2-D surface ocean heat budget, among which the first term on the right-hand side is the ocean heat transport convergence (OHTC) followed by atmospheric flux convergence (AFC) and ocean vertical mixing flux convergence (VMFC). VMFC is not output in CNTL-HR but in SPIN-HR. Therefore, it will be calculated as the residual in CNTL-HR. To gain a complete understanding of ocean mixing in HR and LR, SPIN-HR and SPIN-LR will be used to discuss VMFC in details.

2.2.3.2. Globally Averaged Heat Budget

After taking a global average and time integration of Eq.2.1, the globally averaged T can be expressed as

$$\langle T(t)\rangle - \langle T(0)\rangle = \int_0^t -\frac{\partial\langle wT\rangle}{\partial z} dt + \int_0^t \frac{1}{c_P\rho}\frac{\partial\langle Q\rangle}{\partial z} dt + \int_0^t \frac{\partial}{\partial z}\left(\langle \kappa_z \frac{\partial T}{\partial z}\rangle - \langle \kappa_z \gamma_x\rangle\right) dt, \qquad (2.3)$$

where angle bracket <> represents global average. The heat balance in Eq.2.3 is a function of time and depth because horizontal processes are eliminated by the global average. Globally averaged T is controlled by the globally averaged (i) vertical heat transport (VHTC), (ii) AFC, (iii) VMFC. Since VMFC is not save in the CNTL-HR output, it will be calculated as the residual. The SST is approximated as the temperature at the first model layer located midway between $z=0\ m$ and $z=-10\ m$. Therefore, the globally averaged surface ocean heat budget for SST can be written as

$$\frac{1}{H}\int_{-H}^{0}\langle T(t)\rangle - \langle T(0)\rangle dz = \frac{1}{H}\int_{0}^{t}\langle wT\rangle|_{-H}\,dt + \frac{1}{H}\int_{0}^{t}\frac{<Q_{net}>-<SW|_{-H}>}{c_P\rho}\,dt + \frac{1}{H}\int_{0}^{t} - \left(\langle \kappa_z \frac{\partial T}{\partial z}\rangle - \langle \kappa_z \gamma_x\rangle\right)|_{-H}\,dt, \tag{2.4}$$

where $\langle wT\rangle$ and $\left(\langle \kappa_z \frac{\partial T}{\partial z}\rangle - \langle \kappa_z \gamma_x\rangle\right)$ are zero at $z=0\ m$.

2.3. Mean SST in HighResMIP

Models in HighResMIP used in this study are CMCC-CM2-(V)HR4 (Cherchi et al., 2019), ECMWF-IFS (C. D. Roberts et al., 2018), CNRM-CM6-1 (Voldoire et al., 2019), EC-Earth3P (Haarsma et al, 2019), HadGEM3-GC31 (M. J. Roberts et al., 2019), MPI-ESM1.2 (Gutjahr et al., 2019), CESM1-3 (Danabasoglu et al., 2012; Small et al., 2014; Meehl et al., 2019), AWI-CM1-0 (Semmler et al., 2019). Resolutions of each model are shown in Table 2.1. Six of the eight HighResMIP models (HadGEM3-GC31, ECMWF-IFS, CNRM-CM6-1, EC-Earth3P, CESM1-3 and AWI-CM1-0) have configurations with different ocean resolutions, which can be used to assess the role of ocean resolutions in improving SST biases.

Figure 2.1a and Figure 2.1b demonstrate SST bias in CMIP5 and CMIP6 piControl simulations using the anthropogenic emissions in 1850, where SST observation is taken from HadISST1.0 averaged in 1870-1880. There are 25 CMIP5 models and 34 CMIP6 models and 34 CMIP6 models used here, whose information is shown in Table A1 and Table A2, respectively. Most CMIP6 models keep similar horizontal resolutions with their CMIP5 counterpart, around 1^{o} in both atmosphere and ocean. It is evident that SST simulations show very little improvement from CMIP5 to CMIP6 without many changes in model horizontal resolution.

Figure 2.1c shows the SST biases of LR averaged in HadGEM3-GC31, ECMWF-IFS, CNRM-CM6-1, EC-Earth3P, CESM1-3 and AWI-CM1-0, where 100 years after the spin-up period are used. This set of LR are conducted following the HighResMIP protocol, forced by anthropogenic emissions in 1950, which is different from piControl simulations in Figure 2.1a&b. Therefore, the observation used in Figure 2.1c is taken from HadISST1.0 averaged from 1950 to 1960. Results show similar bias pattern and magnitude to CMIP5 and CMIP6 piControl simulations, indicating that the climatological SST biases are not sensitive to the choice of anthropogenic forcing in 1850 or 1950.

SST biases averaged in HR from 6 HighResMIP models and the corresponding differences between HR and LR are shown in Figure 2.1d&e, respectively. It is shown that cold SST biases are reduced in most regions of the tropics and midlatitudes, but the bias turns to positive from negative in the North Pacific as well as the equatorial Pacific and Indian ocean in HR (Figure 2.1d), indicating overcorrections of SST biases in these regions. In addition, SST still suffers warm biases in EBUS in HR (Figure 2.1d), even though the magnitude of the warm bias is significantly reduced in HR than in LR (Figure 2.1e), suggesting a positive impact of resolution increase on SST biases in all EBUS. As discussed in Small et al. (2015) and Kurian et al. (2021), the bias improvements in

EBUS are mainly induced by the better representation of the alongshore wind structures due to atmosphere resolution increase in HR. Additionally, there is a noticeable improvement of SST biases in eddy-active regions, including Kuroshio extension (KE), Gulf Stream extension (GSE), Agulhas current, and Brazil current regions (Figure 2.1e). Roberts et al. (2019) also pointed out that cold SST biases in boundary current regions can be reduced by increasing ocean resolution, which is seen in Small et al. (2019) and Gutjahr et al. (2019) as well. Finally, the warm SST biases in the SubAntarctic region becomes worse in HR (Figure 2.1d&e), which may be related to net surface flux changes, especially the cloud-related shortwave fluxes (Hyder et al., 2018).

The magnitudes of cold biases in LR can be more than 4^{o}C in the North Atlantic (Figure 2.1a,b,c). As shown in Danabasoglu et al. (2010), SST in the North Atlantic is warmer in CCSM4 with Nordic Sea overflow parameterization than that without overflow parameterization. Zhang et al. (2011) also pointed out that stronger Nordic Sea overflow can lead to warmer SST in the subpolar Atlantic, indicating the importance of overflow to SST simulations. Another point worth noticing is the warm SST biases in the east coast of the U.S and Japan where Gulf Stream and Kuroshio currents separate from the coastlines, which is associated with misrepresentation of currents paths (Hasumi, 2014). It is clearly shown that these biases have been larger improved from LR (Figure 2.1c) to HR (Figure 2.1d).

As shown in Figure A1, HighResMIP models still show uncertainties in SST improvements. All HR show improvements of SST in the EBUS after increasing the atmosphere horizontal resolutions, especially MPI-ESM1-2 and CMCC-CM2. By contrast, only four of the six models with different ocean resolution configurations (HadGEM3-GC31, ECMWF-IFS, CESM1-3 and AWI-CM1-0) show warmer SST outside of EBUS. In addition, amplitudes of the SST difference between HR and LR vary from model to model in KE and GSE regions, ranging from about 0.5^{o}C in ECMWF-IFS to 3^{o}C in CESM1-3. The consistency of warmer SST in HR between CESM and other eddy-resolving and eddy-permitting models suggest that CESM is appropriate to study SST biases.

Figure 2.2a shows SST difference between CNTL-HR and CNTL-LR-HRIC CESM which is consistent with that shown in Figure A1. Globally averaged SST in CNTL-HR and CNTL-LR-HRIC are shown in Figure 2.2c, where year 55 in CNTL-HR is regarded as the first year. The global SST in CNTL-LR-HRIC (blue) is about 1^{o}C cooler than CNTL-HR (red) after 30-year integration. By the end of year 106, CNTL-LR-HRIC reaches a stable state with <SST> oscillating between 17.7 ^{o}C and 17.9 ^{o}C, while CNTL-HR still shows warming trend with 0.2 ^{o}C per century. As shown in Eq.2.2 and Eq.2.4, SST is determined by Q_{net} and other oceanic processes. Q_{net} difference between CNTL-HR and CNTL-LR-HRIC is shown in Figure 2.2b. Note that there is more heat loss from the ocean in CNTL-HR in the eddy-active regions. This strongly suggests that the warmer SST in CNTL-HR is mainly associated with oceanic processes instead of Q_{net} in eddy-active regions. But Q_{net} can be a candidate to explain the warmer SST in the tropics. The 106-year mean of globally averaged Q_{net} is about 0.4 W/m^2 in CNTL-HR and 0.51 W/m^2 in CNTL-LR-HRIC (Figure 2.2d), which indicates the warmer SST in CNTL-HR is induced by oceanic processes in global average sense.

SST and Q_{net} differences between SPIN-HR and SPIN-LR (Figure A2) are consistent with those between CNTL-HR and CNTL-LR-HRIC in the tropics and midlatitudes (Figure 2.2a,b), indicating robust SST bias is already generated after 20 years integration. But negative SST difference is larger and broader in the 20 years SPIN experiments in the subpolar Pacific and SubAntarctic region, indicating that the system is still under adjustment. To investigate details of physical processes controlling SST in the tropics and midlatitudes, heat budget analysis described in Section 2.3 will be applied to HR and LR in next section.

2.4. Heat Balance in CNTL-HR and CNTL-LR-HRIC

2.4.1. Globally Averaged Heat Budget

To diagnose the cause for the 1°C warmer < SST> in CNTL-HR than in CNTL-LR-HRIC (Figure 2.2c), globally averaged surface ocean heat budget analysis is conducted. As shown in Figure 2.3a, the leading-order balance is between VMFC and AFC that includes non-solar heat flux AFC_tur (including sensible, latent and longwave heat flux) and short-wave heat flux AFC_SW. As mentioned in Section 2, VMFC is calculated as the residual in CNTL-HR, as well as in CNTL-LR-HRIC for consistency. Averaged over 106 years, AFC tends to cool down SST by 1916 °C while VMFC and VHTC tend to warm up SST by 1815 °C and 101 °C, respectively. The cooling induced by AFC is the net effect between AFC_SW and AFC_tur. Further decomposition of AFC indicates that AFC_tur tends to cool down SST by 7180°C which is compensated by AFC_SW with 5264°C warming. Furthermore, the cooling induced by AFC_tur is mainly attributed to the heat release by evaporation (See Figure A7). Since the amplitude of SST change is much smaller than other terms, it is plotted in Figure 2.3 with 10 times lager amplitude to visually check its sign.

Figure 2.3b shows the difference of each term in 1-D SST heat balance (Eq.2.5) between CNTL-HR and CNTL-LR-HRIC. Averaged over the 106 years, <SST> in CNTL-HR is 0.86^{o}C warmer than CNTL-LR-HRIC. It is also clear that warming effects of VMFC and AFC_SW are stronger in CNTL-HR than CNTL-LR-HRIC, generating 104.58 ^{o}C and 148.31 ^{o}C warmer SST in CNTL-HR. By contrast, AFC_tur generates 237.36 ^{o}C more cooling in CNTL-HR than new-LR, 62.48% (44.06%) of which is compensated by AFC_SW (VMFC). The warming effect of VHTC is 14.68 ^{o}C weaker in CNTL-HR than CNTL-LR-HRIC, showing negative contribution to warmer <SST> in CNTL-HR.

As shown in Large et al. (1994), VMFC parameterized by KPP includes local mixing (i.e., diffusive mixing, VMFC_lc) and nonlocal mixing (i.e., convective mixing, VMFC_nonlc). Diffusive mixing is proportional to the local vertical T gradient, while convective mixing is induced by convective instability within the boundary layer, which is nonzero only with unstable surface forcing. Therefore, the stronger warming induced by VMFC in HR is the net effect of the local and nonlocal mixing. To study the details of VMFC, the same globally averaged SST heat budget is also applied to 20-year SPIN-HR and SPIN-LR (Figure 2.3c&d) in which output of local and nonlocal KPP mixing are saved as model output. Solid lines in Figure 2.3c&d are exactly balanced and two components of VMFC are represented by blue dashed lines. Results in SPIN-HR and SPIN-LR essentially reproduce those of CNTL-HR and CNTL-LR-HRIC, suggesting that we can use the shorter simulations from SPIN-HR and SPIN-LR to further decompose VMFC into VMFC_lc and VMFC_nonlc and understand how each of the processes contribute the SST difference between HR and LR.

In SPIN-HR (Figure 2.3c), one can see that VMFC_nonlc tends to warm up SST, but VMFC_lc tends to cool down SST. Compared with SPIN-LR, VMFC_nonlc and VMFC_lc are both stronger in SPIN-HR (Figure 2.3d). Table 2.2 shows the 20-year average of heat balance in SPIN-HR and SPIN-LR. SST in SPIN-HR is 0.49°C warmer than SPIN-LR on the 20-year average, which is attributed to stronger VMFC_nonlc and AFC_SW. Contributions to the warmer SST from VMFC_nonlc and AFC_SW are 22.82°C and 23.02°C, respectively. Therefore, VMFC_nonlc and AFC_SW are both important in generating warmer SST in HR simulations from a global average perspective. Further details of why VMFC_nonlc differs between HR and LR will be discussed in Section 2.5.

2.4.2. Surface Ocean Heat Budget

2-d surface ocean heat budget analysis is useful to examine how the balance among various terms governing SST differences between HR and LR varies in geographic locations. Similar to globally averaged heat budget, there are three main factors contributing to the evolution of 2-D SST heat budget: OHTC, AFC and VMFC. OHTC here includes both vertical and horizontal advection processes. To investigate contributions of these three factors, 2-D heat budget analysis given by Eq.2.2 is applied to HR-CNTL and CNTL-LR-HRIC, as well as SPIN-HR and SPIN-LR. The 106-year mean of each term in Eq.2.2 in CNTL-HR and CNTL-LR-HRIC are shown in Figure 2.4, where VMFC is calculated as the residual.

As shown in Figure 2.4a, SST changes relative to year 55 in CNTL-HR are small (less than 1^{o}C) in 106 years, indicating a negligible model drift in CNTL-HR. Consistent with the global-average heat budget (Figure 2.3a), the balance in 2-D surface ocean heat budget is dominated by AFC (Figure 2.4c) and VMFC in majority parts of the global ocean (Figure 2.4d). Ocean advection, OHTC, only shows large contributions in eddy-active regions (Figure 2.4b). From Figure 2.4c, it is clear that heat loss within the upper 10 m of the ocean occurs everywhere, except in the equatorial regions, EBUS, and some Subantarctic regions (Figure 2.4c). The heat loss indicates that the net shortwave heat flux within the upper 10 m is less than the outgoing non-solar heat fluxes. Due to the large compensation among OHTC, TFC, and VMFC, the scale of SST change is much smaller than the other three, similar to the global-average heat budget.

The differences between CNTL-HR and CNTL-LR-HRIC are demonstrated in Figure 2.4e-h. In much of the western and tropical basins, SST is warmer in CNTL-HR, especially in the eddy-active regions where the difference can reach to 4^{o}C (Figure 2.4e). The cooling induced by AFC is stronger in CNTL-HR in the eddy-active regions (Figure 4g), which is mainly contributed by the non-solar component AFC_tur (Figure 2.5b). On the other hand, AFC_SW is larger in CNTL-HR in the tropical and polar regions, but smaller in the EBUS and the Southern Ocean (Figure 2.5a), which is similar to the SST difference pattern in Figure 2.4e. The spatial correlation coefficient of SST difference (Figure 2.4e) and AFC_SW difference (Figure 2.5a) is 0.48, indicating the shortwave heat flux and the spatial pattern of SST differences are closely related, but it cannot fully explain SST differences. Compared with AFC_SW, OHTC also shows stronger warming in CNTL-HR than CNTL-LR-HRIC in the eddy-active regions (Figure 2.4f). By contrast, VMFC differences between CNTL-HR and CNTL-LR-HRIC, which is the net effect of VMFC_lc and VMFC_nonlc, show the opposite sign to AFC (Figure 2.4h).

The relative importance of VMFC_lc *vs*. VMFC_nonlc in the SST difference between HR and LR can be further investigated using direct model output from SPIN-HR and SPIN-LR. Figure A3 shows the results of a similar surface ocean heat budget analysis using the 20-year simulations from SPIN-HR and SPIN-LR. Despite of shorter simulation length, the heat balance in SPIN-HR and SPIN-LR shows a similar structure to that of CNTL-HR and CNTL-LR-HRIC. In both cases, OHTC and VMFC are primarily responsible for the warmer SST in HR in eddy-active regions (Figure A3, Figure 2.4), and AFC_SW and VMFC for the warmer SST in tropical regions (Figure 2.5c). This general agreement between results from SPIN-HR and SPIN-LR and from CNTL-HR and CNTL-LR-HRIC provides strong support to further study VMFC_lc and VMFC_nonlc using SPIN-HR and SPIN-LR, even though they were only integrated for 20 years.

In SPIN-HR, VMFC_lc tends to cool surface temperature except in the ice-covered areas, and the strongest cooling occurs in equatorial regions (Figure 2.6a). In contrast, VMFC_nonlc tends to warm up the surface layer, with large amplitudes in eddy-active regions (Figure 2.6b). An examination of the differences of these two terms between SPIN-HR and SPIN-LR shows that VMFC_nonlc is stronger in SPIN-HR in eddy-active and tropical regions, while the difference of VMFC_lc shows opposite sign to that of VMFC_nonlc (Figure 2.6c&d).

Figure 2.7a shows 20-year mean of area-averaged heat balance in four eddy-active regions shown in boxes in Figure 2.4f. OHTC, VMFC_nonlc and AFC_SW all contribute positively to the heat budget of SPIN-HR (cyan) and SPIN-LR (blue), while VMFC_lc and AFC_tur contribute negatively. SST is about 2.42°C warmer in SPIN-HR than SPIN-LR in these eddy-active regions (red in Figure 2.7a), which is considerably larger than the globally averaged difference of 0.49°C. The stronger AFC_tur in SPIN-HR tends to cool down SST more by 300.63°C, which is counterbalanced by the stronger OHTC (98.9 °C), weaker local mixing (VMFC_lc, 20.48 °C), stronger nonlocal mixing (VMFC_nonlc, 160.09 °C) and stronger TFC_SW (23.56 °C). Therefore, OHTC and VMFC_nonlc are the two most dominant factors in generating warmer SST in eddy-active regions, while TFC_SW plays a secondary role. This result also holds in each eddy-active region as shown in Figure A4. Similar results from 106-year CNTL-HR and CNTL-LR-HRIC are shown in Figure A5a, confirming that vertical mixing and advection are the most important for warmer SST in the eddy-active regions in HR.

In the tropics (30°S-30°N), OHTC shows the smallest contribution to the heat budget in SPIN-HR (cyan) and SPIN-LR (blue, Figure 2.7b). The SST in SPIN-HR is about 0.45 °C warmer than SPIN-LR (red in Figure 2.7b), comparable to the global average of 0.49 °C. Different from eddy-active regions, VMFC_lc is stronger in SPIN-HR than SPIN-LR in the tropics, generating cooler SST of 39.92 °C, which is comparable with -53.38 °C induced by stronger AFC_tur. In addition, VMFC_nonlc and

AFC_SW are the only two processes contributing to warmer SST in SPIN-HR, producing 45.5 °C and 53.71 °C warming, respectively. Therefore, VMFC_nonlc and TFC_SW are equally important for the warmer SST in the tropics in HR. On the other hand, since there is strong compensation between VMFC_lc (-39.92 °C) and VMFC_nonlc (45.5 °C), the net warming effect of VMFC is only 5.58 °C, which is much smaller than TFC_SW. This is consistent with 106-year results shown in Figure A5b.

As shown in Figure A6, there is less low cloud in regions where shortwave heat flux is larger in HR (Figure 2.5a&c), which may be related to model resolution effects on deep and shallow convection schemes in CAM5. We note that convection-related parameters in HR are kept the same to those in LR, which may be responsible for higher tropical precipitation in HR (Chang et al. 2020). Future studies, which is beyond the scope of this work, are needed to investigate differences in parameterized clouds between HR and LR. In the next section, we will focus more on the discussion of causes for upper ocean vertical mixing and advection differences between SPIN-HR and SPIN-LR.

2.5. Vertical Mixing and Advection

2.5.1. Vertical Mixing

As shown in Large et al. (1994) and Van Roekel et al. (2018), nonlocal KPP flux is parameterized as $\kappa_z\gamma_x = C_*\kappa(c_s\kappa\varepsilon)^{1/3}G(\sigma)\overline{(wT)}_{sfc}$, where C_*, κ, c_s and ε are constants defined in Large et al. (1994). In the following discussion, $C_*\kappa(c_s\kappa\varepsilon)^{1/3}$ is expressed as C for convenience. The nonlocal KPP flux is non-zero only under the unstable stratification caused by surface heat flux. In CESM, the unstable condition occurs when the sum of nonsolar heat flux and shortwave heat flux absorbed in the boundary layer is negative, indicating a net loss of heat from the surface. $\overline{(wT)}_{sfc}$ is the non-solar surface heat flux, including longwave heat flux, sensible and latent heat flux (hereafter, referred to as Q_{ns}). Therefore, nonlocal KPP flux can be simply rewritten as

$$\kappa_z \gamma_x = CG(\sigma)Q_{ns}. \tag{2.5}$$

$G(\sigma)$ is the shape function expressed as a cubic polynomial

$$G(\sigma) = c_1 + c_2\sigma + c_3\sigma^2 + c_4\sigma^3, \tag{2.6}$$

where $\sigma = -\frac{z}{h}, c_1 = 0, c_2 = 1,\ c_3 = -2 + 3G(1) - \left(\frac{\partial G}{\partial \sigma}\right)_{\sigma=1}, c_4 = 1 - 2G(1) + \left(\frac{\partial G}{\partial \sigma}\right)_{\sigma=1},$ h is the boundary layer thickness (HBLT) and σ varies from 0 to 1. The boundary conditions of the shape function at $\sigma = 1$ are determined by the mixing below boundary layer (see details in Appendix B1 and B2 in Van Roekel et al. (2018)).

From Eq.2.5, the response of nonlocal KPP flux to surface heat forcing can be broken down into a direct response through Q_{ns} and an indirect response through shape function $G(\sigma)$. To diagnose differences of direct and indirect response between HR and LR, we can rewrite shape function and Q_{ns} in HR as $G_h = \Delta G + G_l$ and $Q_{nsh} = \Delta Q_{ns} + Q_{nsl}$, where h and *l* represent HR and LR and $\Delta(\cdot)$ denotes the difference between HR and LR. Therefore, the difference of nonlocal KPP flux between HR and LR can be expressed as

$$(\kappa_z\gamma_x)_h - (\kappa_z\gamma_x)_l = C[(\Delta G + G_l)(\Delta Q_{ns} + Q_{nsl})] - CG_lQ_{nsl} = C[\Delta G Q_{nsh} + G_l \Delta Q_{ns}]. \tag{2.7}$$

On the right side of Eq.2.7, the first term represents the impact of changes of shape function in HR from LR, which includes the neglectable cross term (indirect response, hereafter VMFC_nonlcG), and the second term represents the impact of differences of nonsolar heat flux (direct response, hereafter VMFC_nonlcQ).

Figure 2.8a shows the breakdown of globally averaged VMFC_nonlc differences between SPIN-HR and SPIN-LR, from which it is clear that VMFC_nonlcQ is larger than VMFC_nonlcG. The 20-year mean of VMFC_nonlcQ difference is 14.01 ^{o}C, accounting for 63% of the total VMFC_nonlc difference. The ratio of VMFC_nonlcQ and VMFC_nonlcG over VMFC_nonlc are shown in Figure 8b with green and red dashed lines, respectively. The contribution of VMFC_nonlcQ to VMFC_nonlc is between 60%-70%.

Figure 2.9a&b display spatial patterns of ratio of VMFC_nonlcQ over VMFC_nonlc and ratio of VMFC_nonlcG over VMFC_nonlc, respectively. In the eddy-active regions, VMFC_nonlcQ can explain more than 90% of VMFC_nonlc differences. But in the regions where the Gulf Stream separates from the U.S. coast, contributions of VMFC_nonlcQ and VMFC_nonlcG to VMFC_nonlc are similar (50%). In the tropics, VMFC_nonlcQ and VMFC_nonlcG both play an important role, accounting for 60% and 40% of VMFC_nonlc differences, respectively. These results reveal that VMFC_nonlcG cannot be neglected when we study the nonlocal KPP flux differences. In the following, we will investigate how the shape function can differ between HR and LR.

As shown in Eq.2.7, the shape function is modulated by the boundary layer depth, which is defined as the shallowest depth where the bulk Richardson number Ri_b (referred to Eq.7 in Van Roekel et al. (2018)) reaches 0.3. By definition, Ri_b can be influenced by the surface buoyancy forcing including freshwater and heat fluxes, indicating a nonlinear relationship between nonlocal KPP flux and surface heat flux. Figure 2.10a-c show shape function estimated as nonlocal KPP flux divided by nonsolar heat flux using monthly CESM output in the Tropics, KE and GSE, respectively, where it is assumed that shape function has small variations within one month. It is clearly shown that the shape function varies strongly with respect to nonsolar heat flux in both tropics and eddy-active regions, confirming that nonlocal KPP flux is not a linear function of nonsolar heat flux.

To mathematically quantify the nonlinearity, binned averages of the estimated shape function in the three regions are shown as dots with bin width of 5 W/m^2 in Figure 2.10d-f, and solid lines are the corresponding quartic fits to the data. The fitting coefficients are labelled in the legends in each panel. Results indicate that shape function and Q_{ns} are highly nonlinear in strong Q_{ns} regime (stronger than 200 W/m^2) in both HR (red) and LR (blue). It is also shown that LR is less capable of simulating extremely strong Q_{ns} in the tropics (stronger than 750 W/m^2) and KE (stronger than 800 W/m^2). In these extreme Q_{ns} regimes, the shape function shows higher values in HR than LR, suggesting a larger contribution of VMFC_nonlcG. Since the shape function is physically related to Richardson number, the quartic fit can only show the nonlinearity between nonlocal KPP flux and Q_{ns} mathematically. The possible oceanic processes that give rise to this nonlinearity will be discussed in Section 6.2

2.5.2. Ocean Advection

As shown in Figure 2.7a, OHTC is the second largest factor in generating warmer SST in HR in eddy-active regions, accounting for 62% of the contribution from VMFC_nonlc. To investigate more details of OHTC, OHTC is further decomposed into mean-flow-induced OHTC (MOHTC) and eddy-induced OHTC (EOHTC), where eddies are defined as the deviation from the monthly mean. Since KE and GSE are two largest eddy-active regions, analysis in this section will be mainly conducted in KE and GSE.

Differences of MOHTC and EOHTC between SPIN-HR and SPIN-LR in KE and GSE are shown in Figure 2.11. Same with Figure 2.4, boxes are regions where OHTC in HR and LR show large differences. In KE, the warming induced by MOHTC can extend more northward and eastward compared with LR (Figure 2.11a&b), leading to warmer MOHTC-related SST difference between HR and LR in the boxed region (Figure 2.11c). In contrast, EOHTC in HR and LR shares similar spatial patterns in KE (Figure 2.11d&e), but produces a stronger warming in HR in the regions where Kuroshio current separates from Japan coasts (Figure 2.11f). In the boxed region, MOHTC tends to generate 69.51 ^{o}C warmer SST in SPIN-HR than SPIN-LR, which is more than 8 times larger than the contribution from EOHTC (8.42 ^{o}C).

In GSE, MOHTC and EOHTC in LR both indicate a more severe overshooting problem of the Gulf Stream (Figure 2.11j&k) compared with those in HR (Figure 2.11g&h) (see also Small et al., 2014). The overshooting problem is improved in HR, leading to a dipole pattern in the differences of MOHTC and EOHTC between HR and LR (Figure 2.11i&l). Different from KE, MOHTC in the GSE box only contributes to warmer SST by 32.75 ^{o}C (Figure 2.11i), which is smaller than the contribution from EOHTC (58.27 ^{o}C, Figure 2.11l).

To investigate more details of the mean circulation in KE and GSE, sea surface height (SSH) is shown in Figure 2.12. In KE, the boundary between subpolar gyre and subtropical gyre is along 42^{o}N in SPIN-HR, which is to the north of that in SPIN-LR (zero lines in Figure 2.12a&b). In addition, the strength of currents just separated from the coast of Japan is stronger in SPIN-HR than SPIN-LR, as well as the recirculation strength. These differences can lead to more warm water advected into the boxed region in SPIN-HR than LR. In GSE, the recirculation in HR is stronger and extends more eastward than in LR. The overshooting problem is improved in HR, which is consistent with the advection patterns in Figure 2.11j&k. The improvement of the Gulf Stream in POP simulations has also been noted by Bryan et al (2007) by increasing horizontal resolution to 0.1^{o}. They showed that the separation of GS is sensitive to dissipation parameter choices. As summarized in Chassignet and Marshall (2008), there are many other factors that can influence GS separation, for instance, subpolar gyre strength, Deep western boundary current, and representation of topography.

2.6. Summary and Discussion

2.6.1. Summary

A recent study by Ma et al. (2020) shows that CMIP6 models share the same SST biases as previous CMIP5 models. Given that these two generations of climate models have similar horizontal resolution of ~1^{o}, it raises the question of to what extent the SST biases are related to insufficient model resolution in these climate models. This study attempts to address this question by analyzing and comparing the HighResMIP ensemble, which is a new model intercomparison project endorsed by CMIP6, aiming at assessing the impact of horizontal resolution of climate models on climate system simulations. The focus of this study is on examination of a set of HighResMIP simulations conducted by iHESP using CESM1.3, which includes a pair of 106-year high- and low-resolution control simulations (CNTL-HR and CNTL-LR-HRIC), and another pair of 20-year high- and low-resolution spin-up simulations (SPIN-HR and SPIN-LR). In each pair, the simulations have identical temperature and salinity state at the initial state, so that initial state differences will not have an impact on ocean heat budget analysis. Three other eddy-resolving and eddy-permitting models in the HighResMIP ensemble, including HadGEM3-GC31, AWI-CM and ECMWF, are also analyzed and compared to CESM1.3. The results confirmed that increasing model resolution can substantially reduce SST biases, including the warm bias in EBUS and cold bias in the western basins and tropics. The focus of this study is on the cold bias as it has not been thoroughly investigated by previous studies.

To investigate SST bias differences between HR and LR, globally averaged and 2-D surface ocean heat budget analyses are applied to HR and LR simulations. The globally averaged heat budget analysis reveals that the heat balance in the uppermost 10 m is mainly held between atmospheric fluxes (i.e., AFC) and oceanic vertical mixing (i.e., VMFC) in both HR and LR, while vertical advection (i.e., VHTC) plays a secondary role. At the surface, non-solar heat flux brings heat out of the ocean. The solar radiation trapped in the top 10 m cannot completely compensate the cooling induced by nonsolar heat flux. Therefore, vertical mixing is important to close the balance by generating warming in the upper 10 m. Further decomposition indicates that it is nonlocal vertical mixing that accounts for the warming in the top 10 m through convective heat flux from the subsurface to the uppermost layer.

The differences of each term in heat budget between HR and LR suggest that it is solar heat flux and nonlocal vertical mixing that account for the 1^{o}C warmer SST in HR, two of which quantitively show equal importance in globally averaged sense. The physical interpretation of nonlocal vertical mixing difference between HR and LR will be discussed in Section 6.2.

2-D surface ocean heat budget analysis demonstrates that stronger VMFC_nonlc and AFC_SW in HR than LR are mainly distributed in the eddy-active regions and tropics, but the most dominant process shows differences between eddy-active regions and the tropics. In the eddy-active regions, VMFC_nonlc (160.09 ^{o}C) contributes the most to warmer SST in HR, followed by OHTC (98.9 ^{o}C) and AFC_SW (23.56 ^{o}C), the importance of which is different from globally averaged results. Further analysis depicts that the stronger VMFC_nonlc in eddy-active regions in HR is mainly induced by the direct impact of nonsolar heat flux instead of indirect impact via shape function. Regarding OHTC, it is found that the improvements of amplitudes and positions of western boundary currents favor warmer SST in HR, especially in KE and GSE. In the tropics, VMFC_nonlc and AFC_SW both contribute to warmer SST in HR by 45.6 ^{o}C and 53.71 ^{o}C, respectively, consistent with globally averaged results which indicates the large contribution of AFC_SW in the tropics to the global average. The stronger AFC_SW is likely induced by less clouds in HR, which may be related to model resolution impacts on cloud parameterization. Different from the eddy-active regions, both the direct and indirect impact of nonsolar heat flux on nonlocal KPP flux contribute to the warmer SST in HR, accounting for 60% and 40% of the nonlocal VMFC difference between HR and LR. It is also found that shape function responds to surface heat flux forcing in a nonlinear manner in both eddy-active regions and tropics, indicating oceanic processes can strongly modulate shape function.

2.6.2. Discussion

Although HadGEM3-GC31, AWI-CM-1-1 and ECMWF show consistency of SST differences between HR and LR with CESM, only AWI-CM-1-1 employs the same vertical mixing parameterization with CESM and the other two use turbulent kinetic energy (TKE) parameterization. In TKE scheme, turbulent tracer flux is nonzero only with nonzero vertical gradient of mean quantities, which is not determined by the surface trace forcing at all (Pandey and Dwivedi, 2021). Therefore, more analysis should be conducted to confirm the impact of vertical mixing on the SST difference between HR and LR in HadGEM3-GC31 and ECMWF.

The fitting polynomial shown in Figure 2.8 is a mathematical approximation of the relationship between shape function and nonsolar heat flux, which differs from the calculation of the shape function in CESM. But this simple analysis shows that the shape function is a nonlinear function of nonsolar heat flux, indicating that it is difficult separate the contribution of shape function to nonlocal KPP flux from that of surface heat flux precisely. The method used in this study is just a diagnostic approach to quantify the impact of shape function and surface heat flux on nonlocal KPP flux. Zhu et al. (2020) found that SST in the North Pacific will get warmer after increasing the strength of convective mixing in LR ocean-only model named Modular Ocean Model version 5 (MOM5), which supports that convective mixing is important to reduce the cold SST biases.

As shown in Eq.2.6, shape function is modulated by HBLT, which is determined by the bulk Richardson number, indicating that oceanic process can influence nonlocal KPP flux through local stratification. In the vertical direction, vertical heat transport (VHT) in the ocean acts to redistribution heat, which has the impact on bulk Richardson number. As shown in Wolfe et al (2008), mean-flow induced vertical heat transport (MVHT) is downward and eddy-induced vertical heat transport (EVHT) is upward in globally averaged sense, which is also seen in other studies (Hieronymus and Nycander, 2013; Banks and Gregory, 2005; Brierley et al., 2010; Griffies et al., 2015; von Storch et al., 2016; Su et al., 2018, 2020; Jing et al., 2020). To shed light on the influence of VHT on nonlocal KPP flux, we conducted sensitivity experiments by changing the strength of submesoscale parameterization in LR CESM. In CESM, the parameter that controls the strength of submesoscale parameterization is the horizontal length scale (HLS) of the front (Smith et al., 2010). Experiments with smaller HLS have stronger submesoscale eddy fluxes in the extratropics. The default value is 5 km (EXP5km), and we conducted two sensitivity experiments with HLS reduced to 3 km for 50 years (EXP3km) and 800 m (EXP800m) for 20 years. Both of these runs started from the first day of year 31 in CNTL-LR and other model settings were kept the same.

The 50-year averaged results in EXP5km and EXP3km are shown in Figure 2.13. As demonstrated in Figure 2.13a, MVHT averaged over KE (145^{o}E-170^{o}E, 34^{o}N-39^{o}N) and GSE (65^{o}W-50^{o}W, 33^{o}N-41^{o}N) is slightly changed from EXP5km to EXP3km, but EVHT shows significant increase with a maximum of 12.69 W/m^2 at 60 m (about 29.71% of EVHT in EXP5km). Figure 2.13b shows nonlocal KPP flux, Q_{net}, shortwave heat flux (SW), and HBLT in KE and GSE in EXP5km (blue) and EXP3km (cyan) on the left y-axis, as well as EXP3km minus EXP5km (red) on the right y-axis. Nonlocal KPP flux is increased by 4% (4.16 W/m^2), and HBLT is decreased by 7% (3.99 m) from EXP5km to EXP3km. Similar results for 20-year mean in EXP5km, EXP3km, and EXP800m are shown in Figure A8. KPP nonlocal flux (HBLT) keeps increasing (decreasing) from EXP5km, EXP3km to EXP800, indicating that the response of nonlocal KPP flux and HBLT to EVHT are monotonic. The stratification defined as the difference temperature at 5 m and that at 45 m also monotonically increases as submesoscale eddies are strengthened. In contrast, Q_{net} is strengthened by about 2% (Figure 2.13b) or 3% (Figure A8b) from EXP5km to EXP3km, but it is weakened by 3.6% (Figure A8b) from EXP3km to EXP800m. In addition, SW shows little changes across three experiments. Therefore, the atmosphere response to submesoscale parameterization is weaker.

The connection of EVHT and KPP nonlocal flux can be connected as following. From Figure 2.13a, it is clear that there is a stronger VHT-induced local warming above

60 m and stronger VHT-induced local cooling below 60 m from EXP5km to EXP3km because the difference of EVHT reaches maximum at 60 m, indicating more thermally stratified upper 100 m in EXP3km. Therefore, HBLT which is defined as the shallowest depth where bulk Richardson number reaches 0.3 is shallower in EXP3km than EXP5km. This result also held in the 20-year results, especially the stratification change, during which the system is still under adjustment, as well as held from EXP3km to EXP800m shown in Figure A8a. On the other hand, in Eq.2.6, shape function can be approximated by $\sigma = -\frac{z}{h}$ as it approaches the sea surface (i.e., σ is small). Therefore, shallower HBLT will lead to larger $|\sigma|$, i.e., larger shape function (larger nonlocal KPP flux) near the sea surface, which can be seen in Figure 2.13b and Figure A8b.

Although HBLT is not save in the output in CNTL-HR and CNTL-LR-HRIC, we can check the contrast of temperature at 45 m (T45m) difference and SST difference between CNTL-HR and CNTL-LR-HRIC as shown in Figure 2.14a. It is clear that the T45m difference is larger than SST difference in most regions, especially in eddy-active regions, indicating there is more heat for nonlocal KPP mixing to move into upper 10 m from the beneath in HR than LR. Combining with the finding in Jing et al. (2020), we propose the mechanism of nonlocal KPP mixing modulating SST as follows. As shown in Figure 2.14b, the stronger heat loss will lead to stronger eddy vertical heat transport ($w'T'$) based on the theory in Jing et al. (2020). Since $w'T'$ peaks around 50 m (Jing et al., 2020) and is decreased to zero at the sea surface, the heat taken by $w'T'$ is mostly stored between 10 m and 50 m, which can be regarded as the heat reservoir for the upper 10 m. Based on Figure 2.4g and Figure 2.14b, the cooling at the surface and the warming below 10 m is both stronger in HR than LR, which feeds stronger nonlocal KPP flux to bring more heat to the upper 10 m. Although nonlocal KPP flux is parametrized in CESM, the determination of HBLT is essentially the reflection of this physical process. More detailed composition analysis should be conducted in the future to verify this mechanism.

The dominant component of nonsolar heat flux difference between LR and HR-CESM is latent heat flux, especially in the midlatitudes. Wu et al. (2018) showed that the latent heat flux becomes stronger in the midlatitudes as they increase the atmosphere resolution from 130km, 60km to 25 km using the atmosphere component of Met Office's Unified Model. Minobe et al. (2008) pointed out the sharp SST gradient is vital to generate surface wind convergence which induces stronger latent heat flux. Small et al. (2013) also confirmed that SST fronts can modulate turbulent heat fluxes through changes of the surface stability using CAM4. Although previous studies were based on atmosphere only experiments, they provide hints that differences of turbulent heat fluxes between LR- and HR-CESM are highly associated with SST fronts in the midlatitudes, which needs more analysis to be confirmed in the future work.

Table 2.1 Models in HighResMIP: CMCC-CM2-(V)HR4 (Cherchi et al., 2019); ECMWF-IFS (C. D. Roberts et al., 2018); CNRM-CM6-1 (Voldoire et al., 2019); EC-Earth3P (Haarsma et al, 2019); HadGEM3-GC31 (M. J. Roberts et al., 2019); MPI-ESM1.2 (Gutjahr et al., 2019);CESM1-3 (Danabasoglu et al., 2012; Small et al., 2014; Meehl et al., 2019); AWI-CM1-0 (Semmler et al., 2019).

Parameter/ model	HadGEM3-GC31	ECMWF-IFS	CNRM-CM6-1	EC-Earth3P	CMCC-CM2-(V) HR4	MPI-ESM1-2	CESM1-3	AWI-CM1-0
Resolution names	LL, HM, HH	LR, HR	LR, HR	LR, HR	HR4, VHR4	HR, XR	LR, HR	LR, HR
Atmosphere resolution (km)	250, 50, 50	50, 25	250, 50	100, 50	100, 25	100, 50	100,25	100, 100
Ocean model	NEMO3.6	NEMO3.4	NEMO3.6	NEMO3.6	NEMO3.6	MPIOM	POP	FESOM1.4
Ocean horizontal resolution	1°, ¼°, 1/12°;	1°, ¼°;	1°, ¼°;	1°, ¼°;	¼°. ¼°;	0.4°, 0.4°;	1º, 1/10°	1°, ¼°;
Ocean levels	75	75	75	75	50	40	62	46

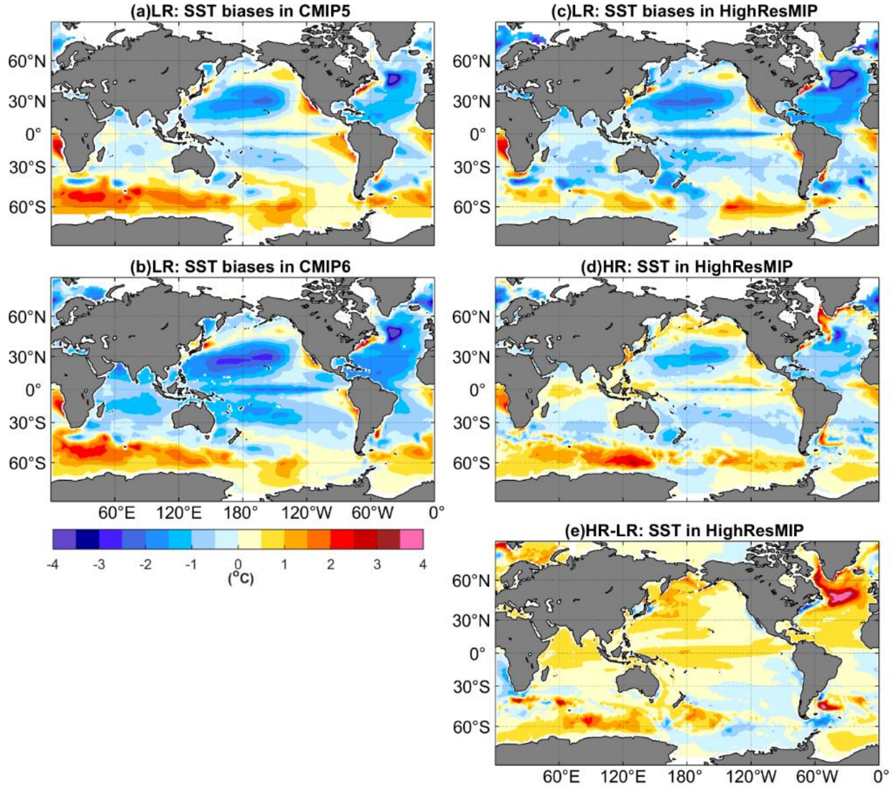
(a)LR: SST biases in CMIP5

(b)LR: SST biases in CMIP6

(c)LR: SST biases in HighResMIP

(d)HR: SST in HighResMIP

(e)HR-LR: SST in HighResMIP

Figure 2.1 SST biases in **(a)** CMIP5, **(b)** CMIP6, **(c)** LR (counterpart of HR) in HighResMIP, **(d)** HR in HighResMIP simulations. 500-years or less SST in piControl CMIP5 and CMIP6 simulations are used. 100-years 1950-control simulations in HighResMIP are used. Climatological SST of HadISST1.0 in 1870-1880 is used in (a)(b) and that in 1950-1960 is used in (c)(d). (e) SST differences between higher resolution and lower resolution HighResMIP models. HadGEM3-GC31, ECMWF-IFS, CNRM-CM6-1, EC-Earth3P, CESM1-3 and AWI-CM1-0 in HighResMIP are used. CMIP5 and CMIP6 models used here are listed in Table A1 and Table A2

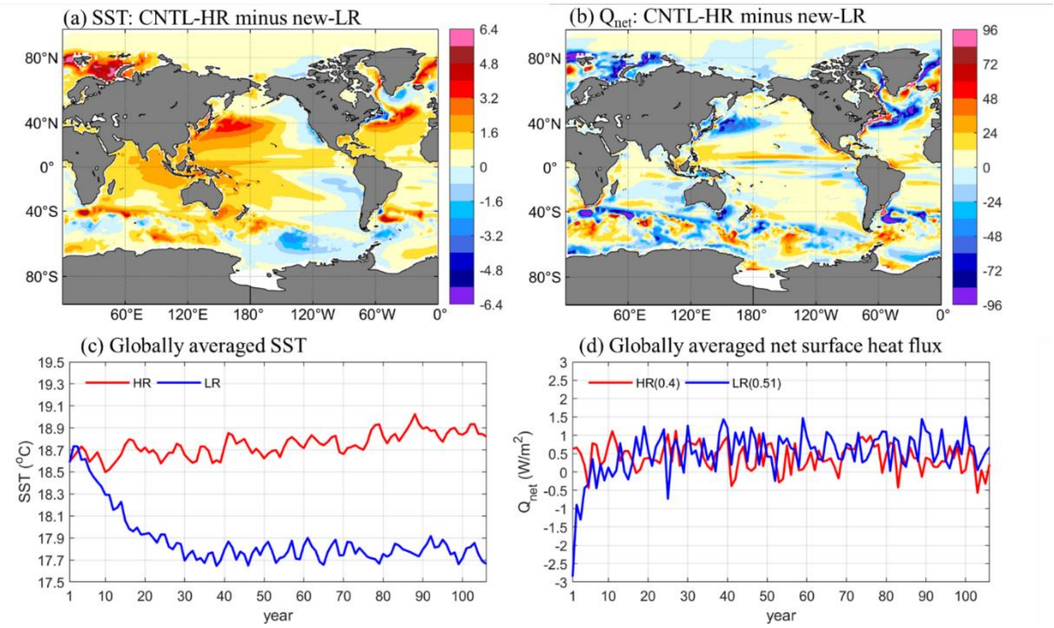

Figure 2.2 Differences of **(a)** SST and **(b)** Qnet between CNTL-HR and CNTL-LR-HRIC (106 years mean); globally averaged **(c)** SST and **(d)** Qnet in CNTL-HR and CNTL-LR-HRIC.

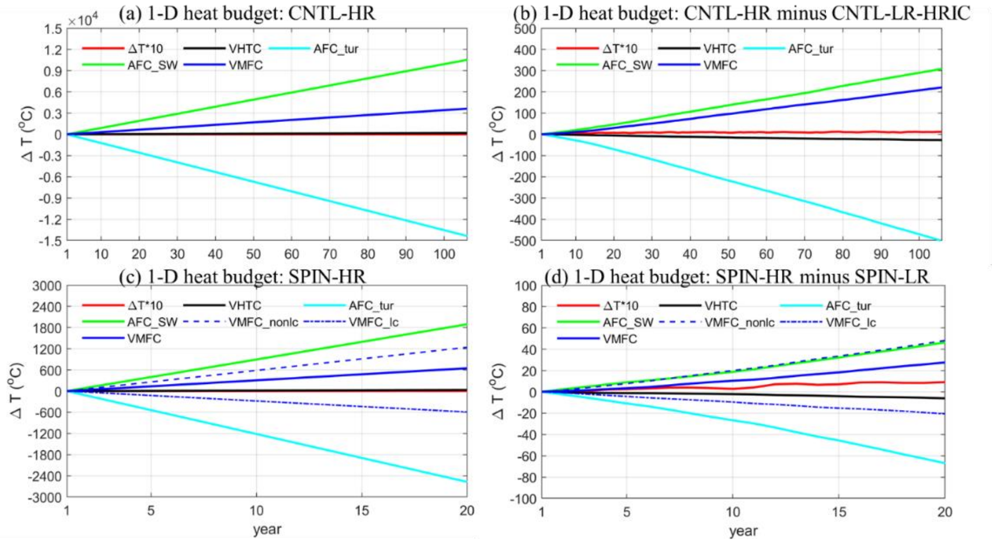

Figure 2.3 Heat budget of globally averaged SST in CNTL-HR **(a)**, CNTL-HR minus CNTL-LR-HRIC **(b)**, SPIN-HR **(c)**, and SPIN-HR minus SPIN-LR **(d)**. Red for SST changes, black for VHTC, green for AFC_tur, green for AFC_SW and blue for VMFC. Units are ^{o}C.

Table 2.2 20-year average of each term in the heat budget of SPIN-HR and SPIN-LR (Unit: ^{o}C).

	ΔSST	**VHTC**	**VMFC**		**AFC_SW**	**AFC_tur**
			Local	nonlocal		
HR	0.34	17.31	296.44	618.70	945.46	-1284.69
LR	-0.15	20.05	-286.21	596.48	923.81	-1254.28
HR-LR	0.49	-3.52	-10.22	22.82	23.02	-31.80

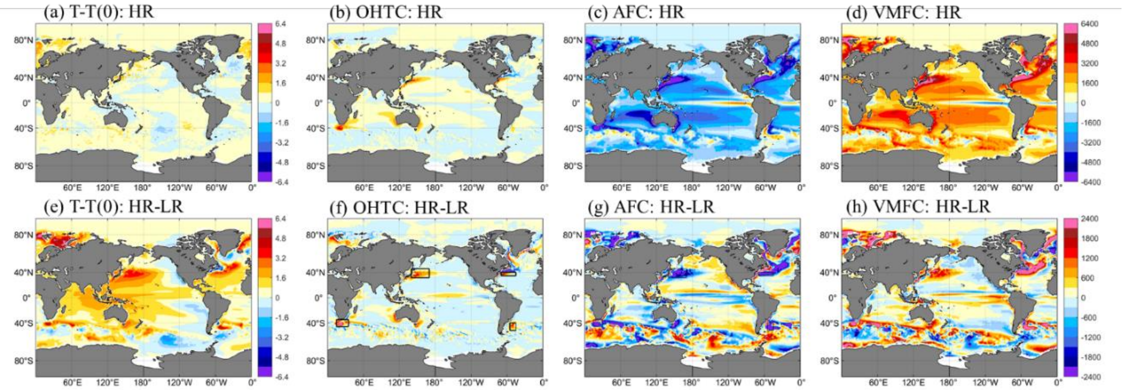

Figure 2.4 106-year mean of **(a)** SST change in CNTL-HR; **(b)** OHTC in CNTL-HR; **(c)** AFC in CNTL-HR; **(d)** VMFC in CNTL-HR; **(e)-(h)** similar to (a)-(d) but for CNTL-HR minus CNTL-LR-HRIC. 2-D heat budget is applied to the upper 10 m. Units are ^{o}C. Notice the scale of (a)(e) is smaller than other panels. Boxes in (f) indicates eddy-active regions with large OHTC differences.

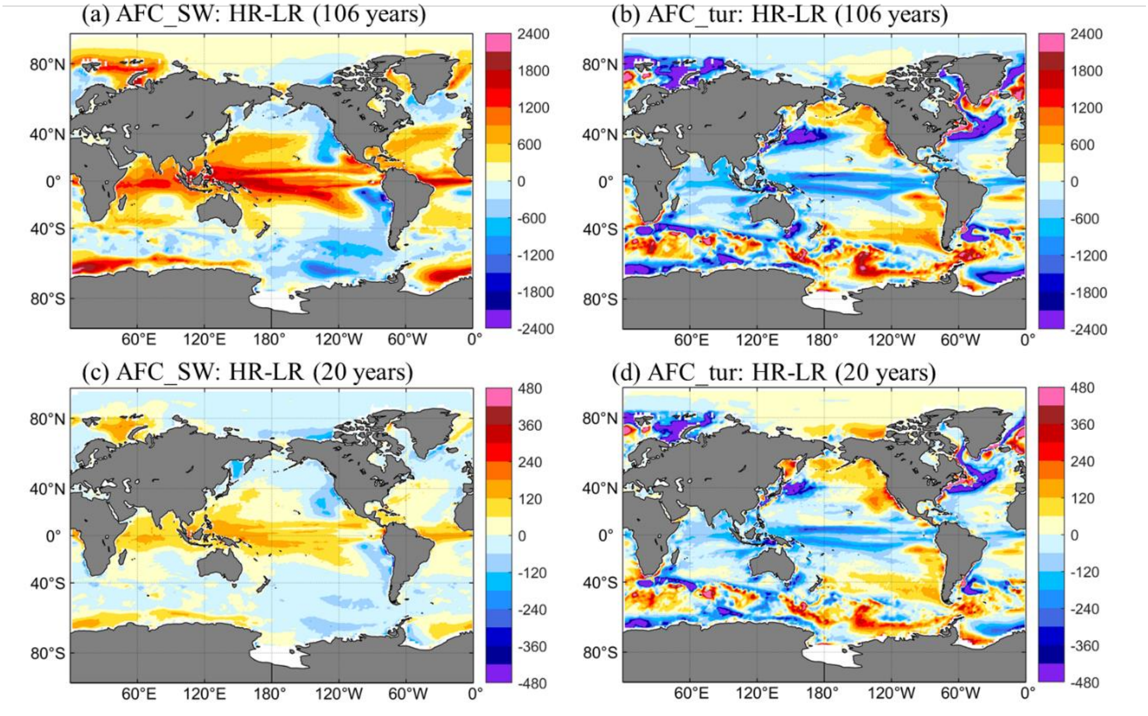

Figure 2.5 Difference of **(a)** AFC_SW and **(b)** AFC_tur between CNTL-HR and CNTL-LR-HRIC; **(c)** AFC_SW and **(d)** AFC_tur between SPIN-HR and SPIN-LR.

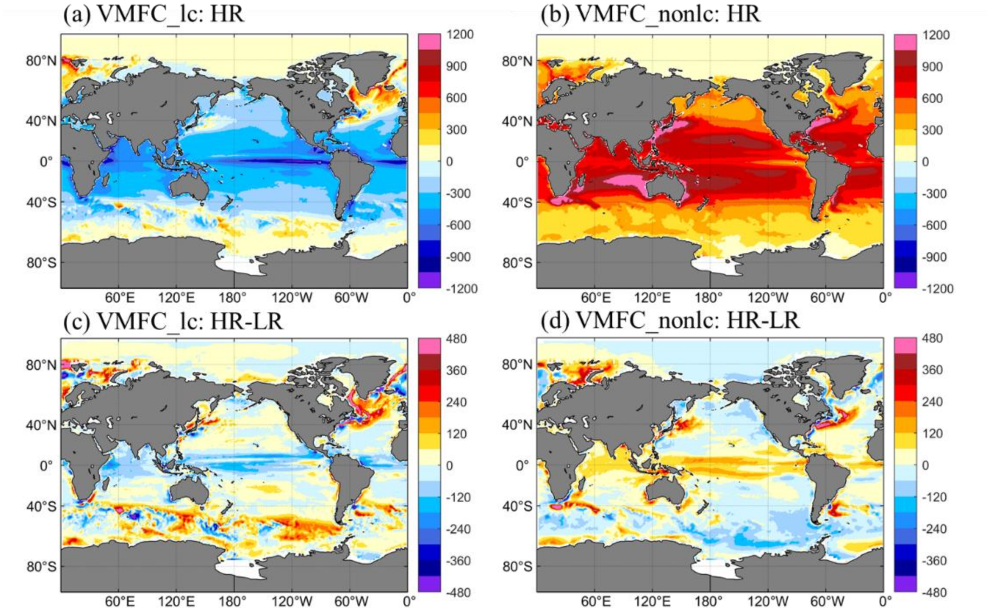

Figure 2.6 Breakdown of VMFC into **(a)** local and **(b)** nonlocal components in SPIN-HR. Difference of **(c)** VMFC_lc and **(d)** VMFC_nonlc between SPIN-HR and SPIN-LR. Units: ^{o}C.

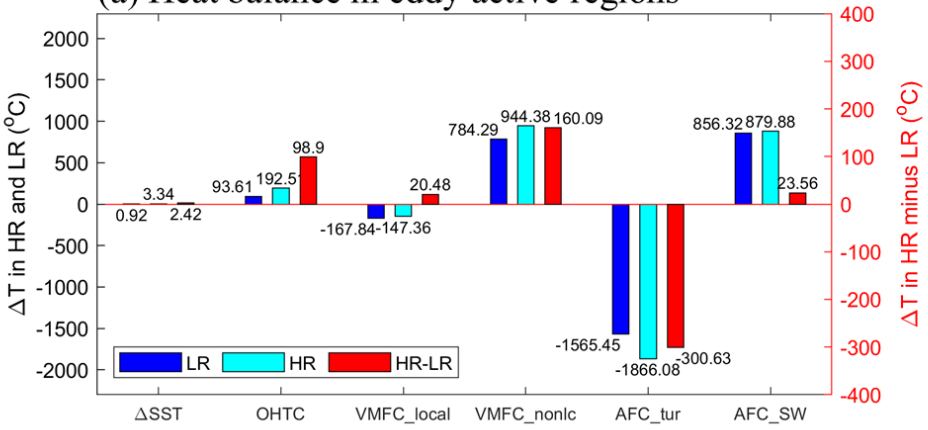
(a) Heat balance in eddy-active regions

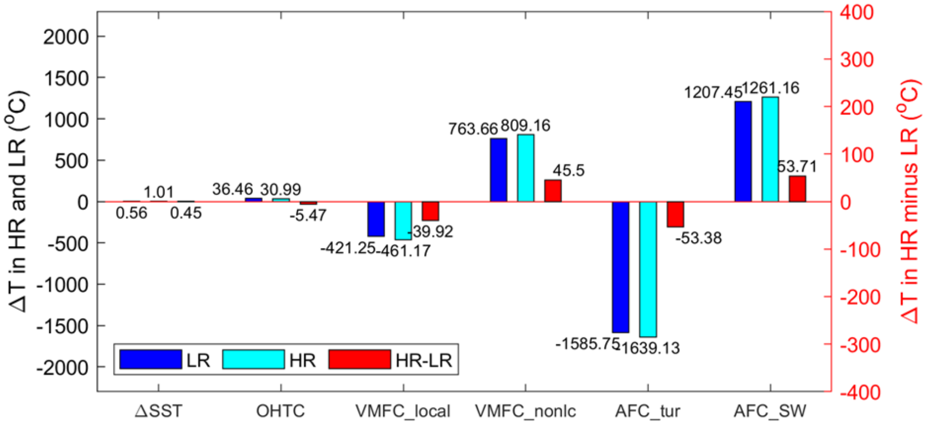
(b) Heat balance in tropical regions

Figure 2.7 20-year mean of heat balance **(a)** in 4 eddy-active regions labelled by black boxes in Figure 4(f) and **(b)** tropical regions. Blue for SPIN-LR, cyan for SPIN-HR and red for SPIN-HR minus SPIN-LR.

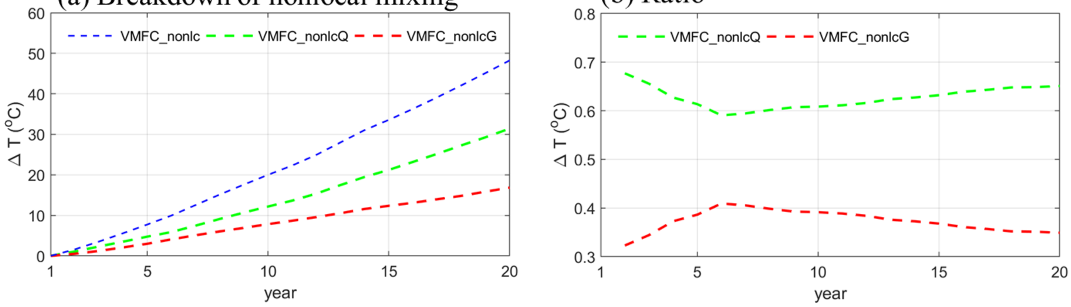
(a) Breakdown of nonlocal mixing
(b) Ratio

Figure 2.8 **(a)** Breakdown of VMFC_nonlc difference between SPIN-HR and SPIN-LR as shown Figure 2.3d, blue dashed for VMFC_nonlc, green dashed for direct impact (VMFC_nonlcQ), red dashed for indirect impact (VMFC_nonlcG); **(b)** Ratio of VMFC_nonlcQ (green) and VMFC_nonlcG (red) over VMFC_nonlc. VMFC_nonlc is the sum of VMFC_nonlcQ and VMFC_nonlcG.

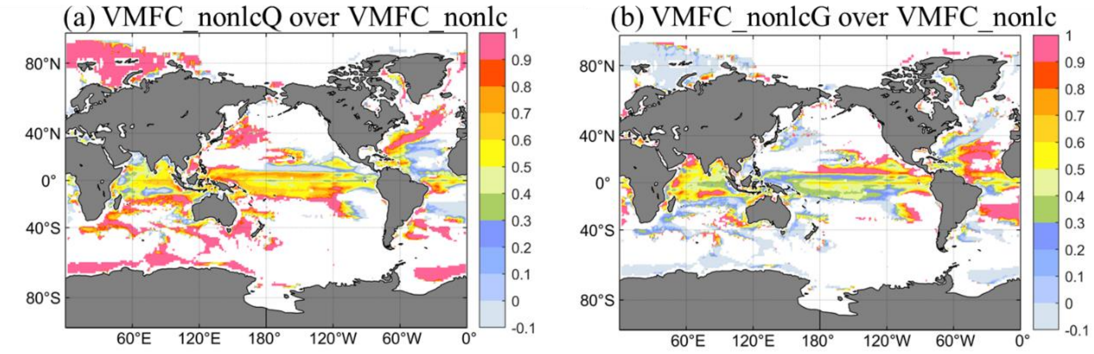

Figure 2.9 **(a)** Ratio of VMFC_nonlcQ over VMFC_nonlc, **(b)** ratio of VMFC_nonlcG over VMFC_nonlc in SPIN-HR and SPIN-LR. Only regions where positive difference of VMFC_nonlc between SPIN-HR and SPIN-LR occurs (Figure 2.6) are shown.

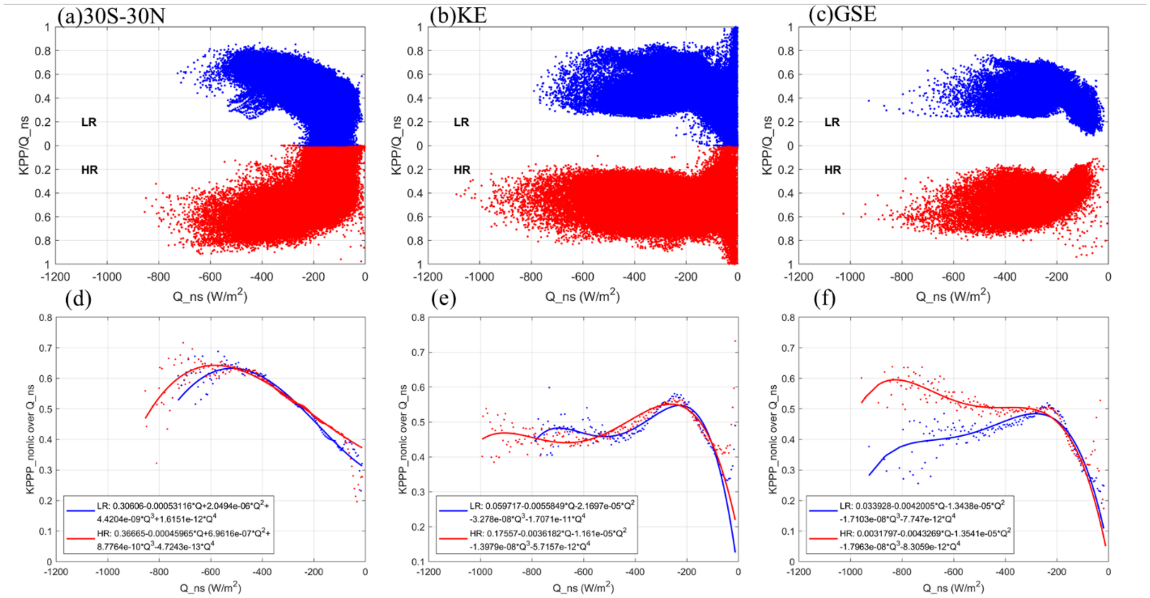

Figure 2.10 Shape function in **(a)** tropics **(b)** KE **(c)** GSE; heat flux-binned shape function in **(d)** tropics **(e)** KE **(f)** GSE, each bin with width of 5 W/m^2. Dots for CESM results, solid lines for quartic fitting. Red for HR and blue for LR.

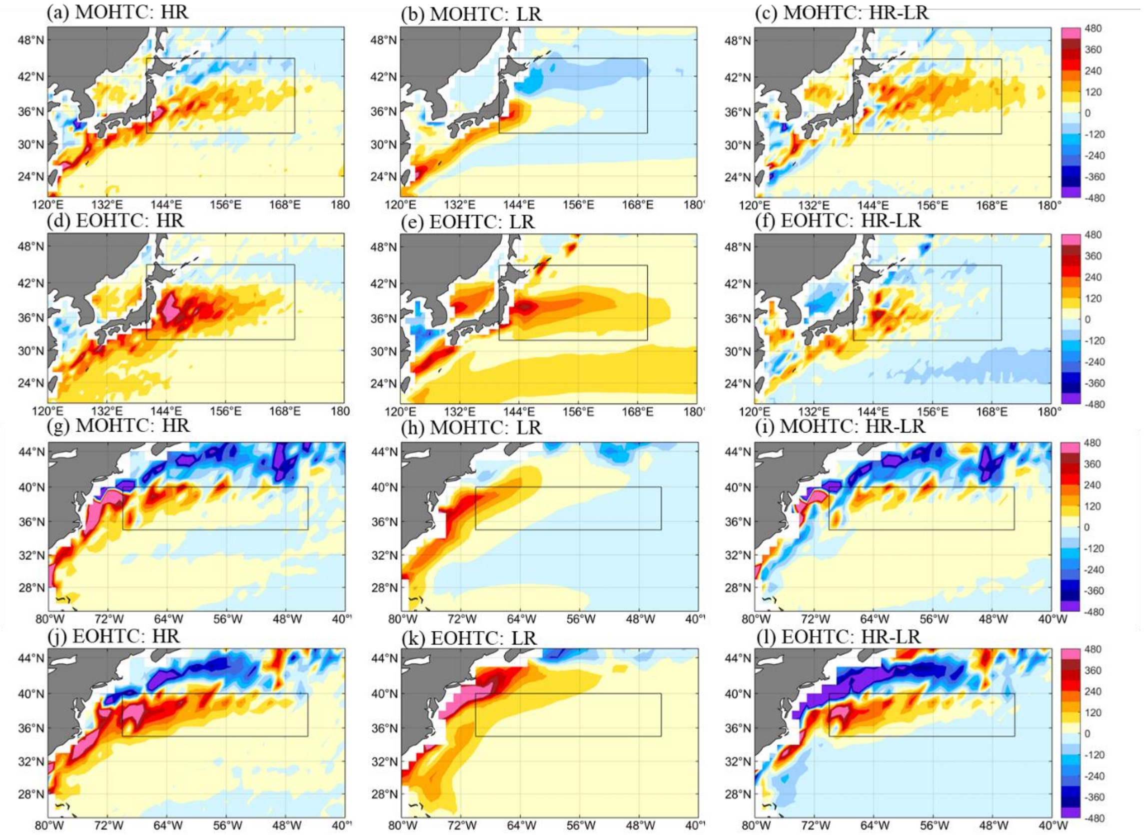

Figure 2.11 **(a)** MOHTC in SPIN-HR **(b)** MOHTC in SPIN-LR, **(c)** MOHTC contrast between SPIN-HR and SPIN-LR, **(d)** EOHTC in SPIN-HR **(e)** EOHTC in SPIN-LR, **(f)** EOHTC contrast between SPIN-HR and SPIN-LR in KE. **(g)-(l)** are similar to (a)-(f) but in GSE. Unit for MOHTC and EOHTC: ^{o}C.

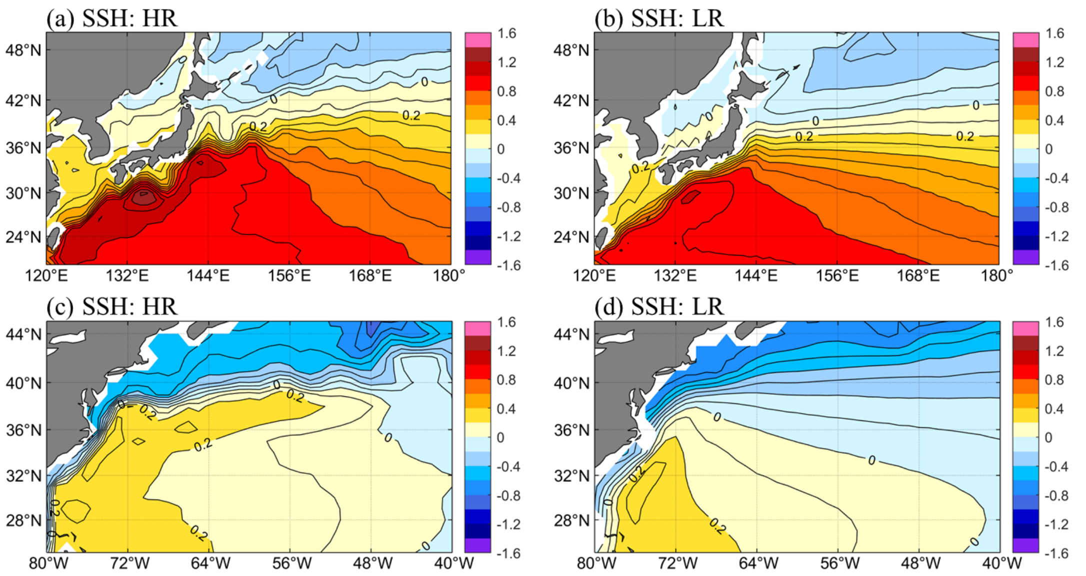

Figure 2.12 SSH simulated in SPIN-HR ((a)(c)) and SPIN-LR ((b)(d)). Unit: m.

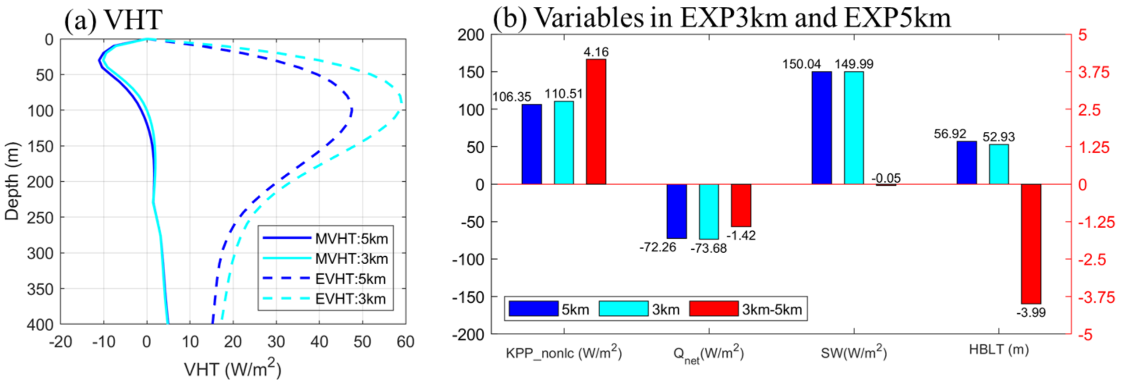

Figure 2.13 50-year averaged **(a)** MVHT (solid) and EVHT (dashed) in EXP5km (blue) and EXP3km (cyan); **(b)** nonlocal KPP flux, Q_{net}, SW at surface, and HBLT (blue), EXP3km (cyan) on left y-axis, and EXP3km minus EXP5km (red) on right y-axis. Results are obtained in KE (145°E-170°E, 34°N-39°N) and GSE (65°W-50°W, 33°N-41°N). Units are shown in brackets following each variable.

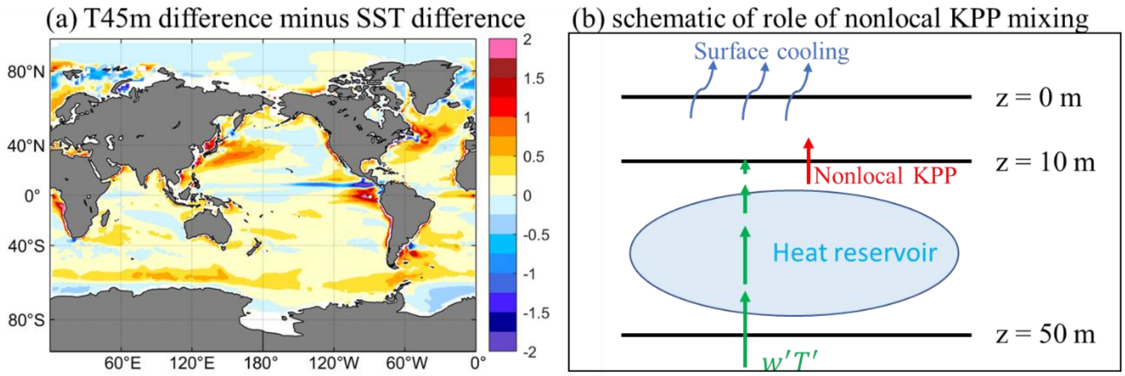
(a) T45m difference minus SST difference

(b) schematic of role of nonlocal KPP mixing

Figure 2.14 **(a)** T45m difference minus SST difference between CNTL-HR and CNTL-LR-HRIC; **(b)** schematic of role of nonlocal KPP mixing in modulating SST.

3. IMPACT OF MODEL HORIZONTAL RESOLUTION ON OCEAN HEAT UPTAKE PROJECTIONS

3.1. Introduction

The ocean is the primary heat reservoir of the Earth system and plays an important role in the climate system. The Fifth Assessment report of the Intergovernmental Panel on Climate Change (IPCC AR5) states that the ocean has absorbed 93% of heat induced by anthropogenic activity over 1972-2010 (Hoegh-Guldberg et al., 2014). The increased heat in the ocean has important implications for the climate system. Warmer temperatures can lead to coral bleaching (Frieler et al., 2013), and also drive marine fishes to migrate poleward (Perry et al., 2005; Pinsky et al., 2013). In addition, thermal expansion of the ocean due to uptake of anthropogenic heat is the principal cause of the increase in sea level at a rate of 3.2 mm yr^{-1} between 1993 and 2010 (Hoegh-Guldberg et al., 2014). The lifetimes and intensities of tropical cyclones are enhanced with the increase of global mean temperature (Emanuel, 2005; Elsner et al., 2008; Knutson et al., 2020), which can lead to more damages to coastal regions (Klotzbach et al., 2018). Therefore, reliable estimates and projections of future ocean heat content (OHC) and ocean stratification changes are vital for societal benefits.

Two methods have been used to calculate ocean heat uptake (OHU). The first method uses radiative fluxes at the top of the atmosphere (TOA). Due to the larger heat capacity of seawater than other Earth system components (air, soil, and rocks), the rate of OHU can be inferred from the radiation imbalance at the top of the atmosphere

(TOA), which can be estimated from satellite observations. In terms of the projected imbalance under transient forcing, the uncertainty of radiation at TOA is still the key focus in climate studies due to the influence of clouds (Boucher et al., 2013). To simulate the effects of transient forcing, climate sensitivity experiment where the CO_2 concentration increases at rate of 1%/yr and doubles its initial value after about 70 years of integration, are typically used as a benchmark for the response of climate to radiative forcing changes. The relationship between TOA imbalance (N) and radiative forcing (F, downward flux) can be written as $N=F+H$, where $H=\lambda\Delta T$ is the upward radiative flux called radiative response, proportional to the globally averaged surface air temperature change (ΔT) and the climate feedback parameter λ (Gregory et al., 2004; Kuuhlbrodt and Gregory, 2012; Rose and Rayborn, 2016). If λ is constant, the relationship between N and ΔT is linear, implying the rate of OHU can be estimated based on F and ΔT. But recent studies find λ varies with time as it can be modulated by the efficiency and spatial variability of OHU through cloud feedbacks (Gregory et al., 2015; Rose et al., 2014; Raper et al., 2002; Senior and Mitchell, 2000; Andrews et al., 2015; Winton et al., 2010; Geoffroy et al., 2013; Armour et al., 2013; Andrews et al., 2012; Andrews and Webb, 2018; Soden and Held, 2006; Williams et al., 2008; Dufresne and Bony, 2008). Furthermore, Deser and Phillips (2009) and Bony et al. (2013) found that the atmosphere circulation and precipitation can be influenced by the radiative forcing directly, as well as clouds (Gregory and Webb, 2008). The associated wind and cloud changes can in turn force the ocean heat content changes (Saenko et al., 2015; Menzel and Merlis, 2019).

Therefore, it is important that we understand OHU processes in the ocean in order to further study the radiation response to radiative forcing.

The second method to estimate the total OHU is to directly computer OHC changes using ocean temperature. This method also allows us to investigate the vertical structures of OHU and its respond to anthropogenic forcing. The surface temperature has been observed by satellites since 1980s (Reynolds et al., 2007; Banzon et al., 2016; Huang et al., 2021). The observations of temperature at the subsurface are scarce until the launch of the Argo Program in 1999 (Roemmich et al., 2009). To date, the Argo Program has deployed more than 3900 floats worldwide to collect temperature and salinity vertical profiles from the surface down to 2000 m. The temperature measured by Conductivity-Temperature-Depth instruments (CTDs) and Expendable Bathythermographs (XBTs) are also used to construct OHC. Despite of the progress in ocean observations, there are large uncertainties in present OHC estimates mainly due to four sources: (i) data quality controlled by environment; (ii) systematic errors of instruments; (iii) construction of climatology; (iv) spatial coverage of measurements (Cheng et al., 2017). Analyses using the observed temperature showed that 87.2% of the total warming from 1960 to 2015 occurred in the upper 2000 m (Cheng at al., 2017). OHC below 2000 m can only be estimated from decadal repeats of hydrographic sections (Purkey et al., 2010; Talley et al., 2016). Within the upper 2000 m, most of the heat was held in the upper 700 m layer before 1990 but is slowly absorbed by the deep ocean in the later period (Chen and Tung, 2014; Cheng at al., 2017).

While the observations cited above have quantified the change of OHC in the upper 2000 m, it remains challenging to assess the physical processes modulating OHU at global scale directly from observations, such as, heat transport and ocean mixing. Numerical models, therefore, have become extremely important tools to assess the relative importance of processes impacting the global OHU, such as, the vertical heat transport (VHT) which is a key process to move the absorbed heat into deep ocean, balancing the heat budget in the ocean (Griffies et al., 2015). VHT is generally discussed in a flux form. In early coarse resolution numerical models that lack eddy parameterizations, globally averaged VHT is a result of compensation between downward heat advection due to mean flow and upward heat flux due to subgrid-scale processes which is parameterized as diffusion (Gregory, 2000). The more recent coarse resolution climate models include Gent-McWilliams mesoscale eddy parameterization (Gent and McWilliams, 1990, hereafter GM90) which is designed to capture tracer fluxes induced by baroclinic mesoscale eddies with a horizontal scale of 50-300 kilometers in non-eddy-resolving climate models. The parameterized eddy transport is found to dominate the subgrid-scale processes in coarse resolution climate models (Gnanadesikan et at., 2005). Other studies confirmed the importance of the parameterized eddy VHT (EVHT) in globally averaged heat balance (Hieronymus and Nycander, 2013; Banks and Gregory, 2005; Brierley et al., 2010; Griffies et al., 2015; von Storch et al., 2016). Furthermore, global simulations with eddy-resolving ocean models (0.1^{o} resolution) yield an upward EVHT that is mostly consistent with the GM90 parameterization (Wolfe et al., 2008). Physically, EVHT is regarded as a counter-gradient process because temperature is cold in the deeper ocean, which acts to reduce the available potential energy (APE) by slumping isopycnals (Griffies et al., 2015). While the GM90 scheme achieves the removal of APE at mesoscales, the submesoscale parameterization by Fox-Kemper et al. (2008) (hereafter FK08) accounts for the conversion of the APE at submesoscales into eddy kinetic energy through mixed-layer baroclinic instability. Similar to GM90, FK08 also generates upward eddy heat transport in climate models (Griffies et al., 2015) which is supported by submesoscale permitting simulations in Su et al. (2018) using a global ocean model at 2 km resolution. As atmospheric CO_2 increases, Gregory (2000) demonstrated that the upward heat fluxes induced by parameterized diffusion is weakened in models with horizontal resolution of 3^o where GM90 and FK08 are absent. Other studies found that parameterized and resolved EVHT are decreased due to reduction of isopycnal temperature gradient in warming climate (Huang et al., 2003; Morrison et al., 2013), indicating that EVHT plays a vital role in OHU projections.

Although parameterizations have been effective in representing EVHT in non-eddy resolving climate models, Griffies et al. (2015) found that the magnitude of model resolved EVHT increases while the parameterized submesoscale EVHT decreases as horizontal ocean model resolution increases from 1^o to 0.1^o, implying that GM90 and FK08 can have strong dependence on horizontal model resolutions. But to the best of our knowledge, there are no studies conducting an explicit comparison of the impacts of EVHT changes on OHU in eddy-resolving and non-eddy-resolving climate models in transient climate subject to anthropogenic forcing. Therefore, the central goal in this chapter is to investigate the role of EVHT in OHU projections in eddy-resolving (0.1^o) and non-eddy-resolving (1^o) CESM.

Another important ocean process modulating the heat redistribution in the ocean is the meridional heat transport (MHT), which transports the heat poleward in a zonally averaged sense (Trenberth et al., 2019). In the Arctic, the stronger MHT leads to more sea ice loss, and thus stronger warming through ice-albedo feedback under climate change (Meehl et al., 2000). Mahlstein and Knutti (2010) also suggested that MHT is an important contributor to projection uncertainties in the Arctic warming. In the Southern Hemisphere, the anomalous equatorward MHT is found to play a crucial role in buffering the warming at the south of ACC (Armour et al., 2016). In the Southern Ocean, Morrison et al. (2015) noted the complexity of MHT changes in deep mixed layer regions: to the south of these regions MHT changes are primarily modulated by the heat content changes, but to the north of these regions MHT changes are driven by eddy processes which are associated with the changes of isopycnal structures. The overturning circulation and gyre circulation in the Atlantic can also modulate MHT changes in the low latitudes and subpolar regions, respectively (Yang and Saenko, 2011; Li et al., 2021).

Bryan et al. (2013) conducted a comparison of MHT changes in 1%-CO_2 climate sensitivity experiments with 1^o and 0.1^o CCSM3.5 in the Southern Ocean. They found that the changes of meridional overturning circulation and MHT show significant differences between 1^o and 0.1^o experiments. In the North Atlantic, finer ocean resolutions generally lead to stronger MHT, as well as lower sea ice area in the Arctic

(Docquier et al., 2019), which can further accelerate the ocean warming. Inspired by these previous studies, a second goal of this work is to provide a careful comparison of the impacts of MHT changes on ocean heat redistributions in HR and LR CESM.

The structure of this chapter is as follows. Section 3.2 provides a description of data and methods used in this work. Section 3.3 introduces the comparison of simulated and observed OHU. Section 3.4 presents the results of globally averaged OHU comparison between HR and LR CESM. Section 3.5 and Section 3.6 show the zonal mean differences of OHU between HR and LR CESM in latitudes. A discussion and summary are provided in Section 3.7.

3.2. Data and Method

3.2.1. Data

The model output used in this study is generated by iHESP, including high-resolution and low-resolution CESM1.3 simulations. Details of these simulations are already introduced in Chang et al. (2020) and here we only give a brief summary. The nominal atmosphere/land and ocean/sea-ice resolution in HR CESM is ~0.25^o and 0.1^o, respectively. Two sets of HR CESM experiments were performed including: (i) PI-Control experiment (PI-CNTL) which is subject to a constant climate forcing in 1850 and run for 500 years, (ii) transient experiment over the period of 1850-2100 (HF-TNST) which is branched from year 250 of PI-CNTL. HF-TNST runs are forced by historical forcing from 1850 to 2005 followed by RCP8.5 forcing from 2006 to 2100. Two other HF-TNST over the period of 1920-2100 are also finished and used in this study. The counterpart LR CESM has an atmosphere/land resolution of ~100 km and the ocean/sea-ice resolution of 1^{o} with GM90 and FK08 parameterizations representing mesoscale and submesoscale eddies, respectively. In contrast to HR, LR HF-TNST constitutes a single run only. To validate the model results, we use estimates of ocean heat content from three sources: (i) Institute of Atmospheric Physics (IAP, Cheng at al., 2017), (ii) Japan Meteorological Agency (JMA, Ishii et al., 2017), and (iii) NOAA (Levitus et al., 2012).

3.2.2. Method

The potential temperature equation is given by

$$\frac{\partial T}{\partial t} = -\frac{\partial(uT)}{\partial x} - \frac{\partial(vT)}{\partial y} - \frac{\partial(wT)}{\partial z} + \frac{1}{c_P\rho}\frac{\partial Q}{\partial z} + \kappa_H\left(\frac{\partial^2}{\partial x^2} + \frac{\partial^2}{\partial y^2}\right)T + \frac{\partial}{\partial z}\kappa_z\left(\frac{\partial T}{\partial z} - \gamma_x\right), \qquad (3.1)$$

where T is the potential temperature; u, v, and w are the velocity components along the x, y, z axes; Q is the heat flux including solar and nonsolar component; c_P is the heat capacity taken as 3996 J/kg/^{o}C; the density of seawater, ρ is assumed to be constant as 1026 kg/m^3; κ_H (assumed to be spatially constant) and κ_z are the horizontal and vertical diffusivities; γ_x represents the nonlocal term in the K-profile parameterization (Large et al., 1994). On the right-hand side of Eq.3.1, the first three terms represent the total advection, defined as the summation of resolved and parameterized advection in LR and only the resolved one in HR, followed by the atmospheric heat flux forcing, horizontal mixing and vertical mixing, respectively.

We will analyze the heat budget (Eq.3.1) by averaging it across an upper layer of depth h and a latitude band y_0~y_1. We first integrate Eq.3.1 is from the surface to depth h:

$$\frac{\partial}{\partial t}\int_h^0 T dz = -\int_h^0 \left(\frac{\partial uT}{\partial x} + \frac{\partial vT}{\partial y}\right) dz + wT|_h + \frac{Q_{net}-SW|_h}{c_P\rho} + \mathcal{M}, \tag{3.2}$$

where $\mathcal{M}$ represents vertical and horizontal mixing with any forms of integrations hereafter, $SW|_h$ is the shortwave penetrative heat flux at depth h which is set to zero below 200 m in CESM, and $c_P\rho\int_h^0 T dz$ is OHC in the upper h m. Eq.3.2 is then integrated over the latitude band y_0~y_1 and zonally from east to west as follows:

$$\frac{\partial}{\partial t}\left(\oiint \int_h^0 T dz\, dA\right) = \int_{west}^{east}\int_h^0 \left(vT|_{y0} - vT|_{y1}\right) dz dx + \oiint \frac{Q_{net}-SW|_h}{c_P\rho} dA + \oiint wT|_h dA + \mathcal{M},$$

where $\oiint \cdot\, dA \equiv \int_{west}^{east}\int_{y0}^{y1} \cdot\, dy dx$. Finally, the equation governing the evolution of OHC (unit: J) averaged as described above can be derived by integrating the above equation in time:

$$c_P\rho \oiint \int_h^0 T(t) - T(0) dz\, dA = \mathcal{H} + \mathcal{F} + \mathcal{V} + \mathcal{M}, \tag{3.3}$$

where $\mathcal{H} \equiv \int_0^t \int_{west}^{east}\int_h^0 c_P\rho\left(vT|_{y0} - vT|_{y1}\right) dz dx\, dt$, $\mathcal{F} \equiv \int_0^t \oiint (Q_{net} - SW|_h) dA dt$, $\mathcal{V} \equiv c_P\rho\int_0^t \oiint wT|_h dA dt$ represent OHC changes induced by MHT, atmosphere forcing, and VHT.

If y0 and y1 in Eq.3.3 are taken as the south and north pole, Eq.3.3 yields the globally averaged OHC budget:

$$\langle OHC(t)\rangle - \langle OHC(0)\rangle = c_P\rho\int_0^t \langle wT|_h\rangle\, dt + \int_0^t \langle Q_{net} - SW|_h\rangle\, dt + \mathcal{M}, \tag{3.4}$$

where horizontal divergences are eliminated and $\langle\cdot\rangle$ represents the horizontal averaging operator. The term on the left-hand side of Eq.3.4 represents the timeseries of OHC anomaly relative to the value at *t=0* and terms on the right-hand side are the globally averaged VHT, heat flux, and mixing induced OHC changes. Unless specified otherwise, in this study, OHU in CESM is defined as the OHC difference between HF-TNST and PI-CNTL to eliminate the impacts of model drift. We define “eddy” as the deviations from the 100-year mean in HR, and the summation of GM90 parametrized eddy and deviations from 100-year mean in LR. Under this definition, the changes in seasonal cycle, interannual and decadal variabilities are included in the “eddy” component. In Section 3.4.2, we will show our conclusions are not sensitive to the “eddy” definition.

3.3. Comparison of OHU in CESM and Observations

This section will introduce a comparison of OHU estimates derived from CESM simulations and those from IAP, JMA and NOAA. Figure 3.1 shows the OHU anomaly (OHUA) in the upper 700 m, and 2000 m relative to the respective time mean over 1960-1970 as the baseline. There are two reasons why we choose 1960-1970 as the baseline. Firstly, the estimates from the IAP dataset are more reliable after 1960 (Cheng et al., 2017). Secondly, the 10-year mean is to minimize the impacts of interannual variability. As demonstrated in Figure 3.1a, three observation datasets show a broad agreement in the upper 700 m with OHUA values around 2.1×10^{23}~2.5×10^{23} J at the end of 2020. The observed values are bounded by HR (2.8×10^{23} J, blue solid) and LR (2.0×10^{23} J, blue dashed). Both models and observations have captured the coolings induced by three largest volcanic eruptions (red triangles) in the twentieth century which occurred in 1963 (Mount Agung), 1982 (El Chichon), and 1991 (Mount Pinatubo). OHUA in HR matches observations well between 1983 and 2005, while LR always underestimates OHUA in the upper 700 m. The observed OHUA is increasing at the rate of 3.8×10^{21} J/year over the 60-year period of 1960-2020, which is in much better agreement with HR (4.0×10^{21} J/year) than LR (3.0×10^{21} J/year), thereby strengthening our confidence in the derived OHU from the HR simulations.

The discrepancy between observed and HR OHUA in the upper 700 m between 1960 and 1983 may be largely attributed to the strong multidecadal oscillation in HR (solid blue) associated with Polynyas in PI-CNTL (Chang et al., 2020). The OHU in CESM defined as the OHC difference between HF-TNST and PI-CNTL values can also be influenced by differences in internal variabilities within HF-TNST and PI-CNTL. Since we are focusing on high CO_2 emission scenario, impacts of internal variabilities on OHU projections will be weaker as the CO_2 concentration rises. For instance, OHUA of upper 700 m in HR and LR without internal variabilities in PI-CNTL, are shown in Figure B9a, which reveals a better simulated OHUA in HR before 1983 than that in Figure 3.1a. The internal variabilities in PI-CNTL can be excluded using Empirical Mode Decomposition (Huang et al., 1998). The OHUA after 2005 in HR is similar to that in Figure 3.1a (blue solid). In 2020, the OHUA without subtracting PI-CNTL from HR and LR are still the upper and lower bounds of among the simulated and observed OHUA. The trend of OHUA in Figure B9a is 4.2×10^{21} J/year in HR and 3.2×10^{21} J/year in LR which is consistent with the corresponding trends in Figure 3.1a. Therefore, we will continue to define OHU as the difference between HF-TNST and PI-CNTL to define OHU for the heat budget analysis in the following sections.

The difference of OHUA in the upper 2000 m between HR and LR is smaller than in the upper 700 m with HR showing more consistency with the observations. LR still underestimates OHUA after 1995 (Figure 3.1b). At the end of 2020, OHUA reaches 3.3×10^{23} J~3.7×10^{23} J in observations, 3.4×10^{23} J in HR, and 3.1×10^{23} J in LR. The observed trend of OHUA is 5.7×10^{21} J/year on average while that in HR and LR are 5.1×10^{21} J/year and 4.8×10^{21} J/year, respectively. The similar performance of HR and LR in simulating OHUA in the upper 2000 m can also be seen without subtracting PI-CNTL from HF-TNST (Figure B9b). Since both HR and LR give a reasonable representation of the observed OHU over the period of 1960-2020, especially in the upper ocean, it is worth comparing OHU in HR and LR over the future period to shed light on the impacts of model resolutions on OHU projections.

3.4. Globally Averaged OHU Projection in HR and LR CESM

3.4.1. Comparison of OHU Projections

Figure 3.2a shows full-depth integrated global OHU in LR (dashed) and HR (solid). The overlap of the dashed and solid line indicates horizontal model resolutions in CESM have negligible impacts on the projected global OHU increase that reaches a value of 2.7×10^{24} J by the end of 2100, which is 7 times larger than the value in 2020. The vertical structure of OHU in HR is shown in Figure 3.2b, indicating injection of anthropogenically induced heat into the ocean, starting from the surface and gradually penetrating the deep ocean to a depth of about 1000 m by the end of 2100. The surface warming is relatively weak before 2000 due to the relatively weak greenhouse gas forcing (GHG). The warming characteristics in HR also hold in LR, but compared with HR, there is less heat in the upper 250 m in LR, especially after 2000, and more heat penetrating below 250 m (Figure 3.2c), implying a different response of OHU to GHG between HR and LR.

Though the OHU difference in the upper 250 m shows strong interannual variability, the time mean averaged between 2000 and 2100 is positive in the upper ocean (Figure 3.2d), with peaks around 30 m and 70 m and gradually decreasing at greater depths to zero at 250 m. The time-averaged OHU in the upper 100 m is about 7.5% larger in HR than LR. Overall, the OHU difference in the upper 250 m is 2.7×10^{22} J over the 2000-2100 period while that below 250 m is -3.3×10^{22} J. This result is consistent with the baroclinic structure in the study by Kuhlbrodt and Gregory (2012), which suggested that CMIP3 and CMIP5 models transport heat too deeply in the ocean compared to the observations. Since the anthropogenic heat is transported into the deep ocean gradually, ocean stratification is always enhanced over time in both HR and LR. Therefore, the stronger OHU in the upper ocean in HR means a more stratified ocean in HR. This has large implications for marine ecosystems because a more stratified ocean can lead to more ocean deoxygenation (Keeling et al., 2010; Breitburg et al., 2018) as well as reduction of upward nutrient flux, which in turn leads to a reduced primary production and export (Fu et al., 2016).

3.4.2. Importance of VHT in OHU Projections

To further investigate the mechanism controlling OHU differences between HR and LR, we computer the globally averaged heat budget (Eq.3.4) in the upper 250 m, where SW is zero in CESM. The evolution of heat budget in the upper 250 m in HR over 2000-2100 (Figure 3.3a) reveals a continuous increase in OHU (red), resulting from an increase in Q_{net}-induced OHU (magenta). The VHT moves heat to the deeper ocean, making a negative contribution to the OHU in the upper 250 m (blue). The contribution from vertical mixing is also negative but weaker in magnitude than VHT (cyan). At the end of 2100, there is about 9.0×10^{23} J anthropogenic heat in the upper 250 m in HR due to 2.6×10^{24} J heating from the atmosphere along with 1.2×10^{24} J and 4.9×10^{23} J cooling from VHT and vertical mixing, respectively.

Figure 3.3b shows the difference of heat budget in the upper 250 m between HR and LR. OHU is stronger in HR except after 2095 (red solid), but the OHU difference is always positive once excluding the all internal variabilities in HF-TNST and PI-CNTL of HR and LR (dashed red), indicating the robustness of stronger OHU response to GHG in HR. The difference of OHU averaged over 2000-2100 is 3.0×10^{22} J, which is mainly attributed to the VHT difference (blue) with a contribution of 9.7×10^{22} J compensated by vertical mixing difference (cyan) of -7.2×10^{22} J, while only 16.7% of OHU difference is attributed to the difference of atmosphere heating. Therefore, the changes of VHT in response to GHG is important for the redistribution of oceanic heat due to anthropogenic activity and for the associated changes in the ocean stratification. The more stratified upper ocean in HR, compared to LR, is a direct result of less downward anomalous VHT in the former.

To investigate in more detailed changes in VHT, the evolution of VHT induced OHU of the upper 250 m in HR PI-CNTL and HF-TNST are shown in Figure 3.4a. In PI-CNTL, VHT warms up the upper 250 m (blue solid) through the compensation between a warming induced by EVHT (blue dashed) and a cooling induced by MVHT (blue dot-dashed). Compared with PI-CNTL, VHT in HF-TNST mitigates the upper ocean warming in the future, showing consistency with Figure 3.3a. In addition, the EVHT induced warming is weaker in the future and MVHT induced cooling is stronger, both of which work together to determine the total change in VHT. As shown in Figure 3.4b, the less downward VHT in HR relative to LR is mainly attributed to the EVHT difference (dashed) while the MVHT difference (dot-dashed) only compensates 30% of the EVHT difference. Combining with Figure 3.4a, the physical interpretation of results in Figure 3.4b is as follows: the warming induced by EVHT is weakened less in response to anthropogenic forcing in HR than in LR, partly compensated by the difference of MVHT changes between HR and LR, leading to relatively more heat trapped in the upper 250 m in HR.

EVHT at 250 m is parameterized by GM90 in LR, where it is calculated as the skew flux based on horizontal gradient of temperature (Griffies, 1998; Smith and Gent, 2002). On the other hand, EVHT in LR is also related to vertical temperature gradient through $\langle w^{*}T\rangle|_{h} = \langle \int_{h}^{0} (w^{*}\, \partial T/\partial z)\, \mathrm{dz}\, \rangle + \langle \int_{h}^{0} (T \partial w^{*}/\partial z)\, \mathrm{dz}\, \rangle$ where w^{*} is the parameterized bolus vertical velocity based on the slope of isopycnal at each grid cell. Inspired by the calculation of EVHT in LR, it is beneficial to quantify the sensitivity of EVHT to temperature gradient changes in HR and LR from a globally averaged perspective. Figure 3.5 shows a scatterplot of globally averaged EVHT versus globally averaged vertical temperature gradient at 250 m. In PI-CNTL, there is no significant change in EVHT with changes in $\partial T/\partial z$ for both HR (green) and LR (cyan). The stratification is weaker in LR than HR while EVHT in LR is stronger than HR, indicating stronger parameterized response of EVHT to $\partial T/\partial z$ in LR. Under GHG, EVHT decreases with the increase of $\partial T/\partial z$ in a linear manner in HR (red) and LR (blue), but the linear regression line is steeper in LR than HR with a slope of -736 W/m^2 per ^{o}C/m in LR and of -531 W/m^2 per ^{o}C/m in HR. To check the sensitivity of results to eddy definitions, we also illustrate a scatterplot with eddies defined based on seasonal mean in HR and GM90 in LR in Figure B10, showing consistent results with Figure 3.5 although the slopes are larger. In conclusion, the parameterized EVHT is more sensitive to $\partial T/\partial z$ changes than the resolved EVHT, which still holds with different eddy definitions. To better capture heat distribution under GHG, it needs more efforts to tune GM90 parameterizations to improve the relation of EVHT and $\partial T/\partial z$ in terms of HR.

3.4.3. Vertical Structures of VHT

Since VHT is important to generate OHU differences between HR and LR, the complete vertical structures of VHT will be discussed in this section. As demonstrated in Figure 3.6a, MVHT is always downward from the surface to deep ocean (dot-dashed) while EVHT transports heat upward (dashed lines), in agreement with Griffies et al. (2015). The MVHT peaks around 100 m with an amplitude of ~2.5 PW (1 PW= 10^{15} W) in HR and ~2.9 PW in LR. The EVHT shows a double-peaked structure in HR (red dashed) with peaks approximately at depths of 50 m and 200 m although the latter peak is weak. The former is generated by the appearance of ocean fronts and surface forcing (Jing et al, 2020) while the latter is associated with the baroclinic eddies around the depth of thermocline. In contrast, only one peak at 50 m depth (blue dashed) can be detected in LR although GM90 is implemented. As a result of compensation between MVHT and EVHT, total VHT peaks at 25 m with upward flux.

VHT changes over 2000-2100 (ΔVHT) defined as the difference between HR-TNST and PI-CNTL are depicted in Figure 3.6b. VHT is more downward in the future (solid) in both LR (blue) and HR (red) with the maximum changes around 250 m. The maximum change in LR is -0.46 PW (0.29 PW in PI-CNTL for reference), while it is -0.38 PW (0.15 PW in PI-CNTL for reference), in HR. The maximum difference of ΔVHT between HR and LR is also around 250 m as shown in Figure B11, indicating a more heat convergence in the upper 250 m and heat divergence under 250 m in HR, which is consistent with the heat difference pattern between HR and LR shown in Figure 3.2c. Furthermore, the weakening of EVHT peaks around 50 m and 250 m in HR corresponding to the two peaks in EVHT in PI-CNTL, but only around 250 m in LR associated with GM90. The change of EVHT (ΔEVHT) at 250 m is -0.29 PW in HR (red dashed in Figure 3.6b, 14.2% of the mean in PI-CNTL) and -0.40 PW in LR (blue dashed in Figure 3.6b, 16.4% of the mean in PI-CNTL), implying the upward EVHT is weakened in the future and the weakening is stronger in LR, confirming the results in Figure 3.4a. Moreover, the downward MVHT at 250 m is strengthened by 0.09 PW in HR (red dot-dashed in Figure 3.6b) and 0.06 PW in LR (blue dot-dashed in Figure 3.6b). The difference of MVHT changes counters the difference of ΔEVHT, but with smaller amplitude (0.03 PW versus 0.11 PW), resulting in a weaker net downward ΔVHT at 250 m in HR than LR, which further comfired the significant difference of EVHT between HR and LR.

Overall, globally averaged heat budget showed that the larger OHU in the upper 250 m in HR is attributed to the less downward EVHT, implying the importance of EVHT in determining vertical structures of OHU. EVHT generally is strong in the midlatitudes, especially in the Kuroshio extension, Gulf Stream extension, and the Southern Ocean, implying OHU differences between HR and LR could vary from region to region. In the following sections, regional analyses are conducted.

3.5. Meridional Distributions of Projected OHU

Since globally averaged OHU is stronger in the upper 250 m in HR than LR, it is worth further investigating which region is responsible for this difference between HR and LR. As a re minder, OHU is still defined as the OHC difference between HF-TNST and PI-CNTL. Figure 3.7a shows OHU difference between HR and LR ($dOHU$) in the upper 250 m averaged over 2000-2100. It reveals generally less OHU in HR than LR to the south of 35^{o}S but generally more to the north of 35^{o}S with abundant finer structures. For instance, more heat in HR can be found in the Arctic, Indian Ocean, Western Pacific, and less heat in the Kuroshio extension, subpolar North Atlantic. To simplify the discussion, it is useful to examine the zonally integrated values of $dOHU$ (Figure 3.7b). The results clearly show that there is less OHU in HR to the south of 35^{o}S (blue) but more OHU in HR to the north of 35^{o}S except at latitudes around 40^{o}N (red) which coincide with the Kuroshio extension as shown in Figure 3.7a. Since $dOHU$ is mostly positive to the north of 35^{o}S and negative to the south of 35^{o}S, it is reasonable to take 35^{o}S as the latitudinal boundary to divide the globe into SubAntarctic (SA) and North Regions (NR).

Vertical profiles of OHU in SA and NR averaged over 2000-2100 are depicted in Figure 3.8a. In SA, less OHU is in HR (dashed red) than in LR (dashed blue) and the difference is nearly uniformly distributed from the surface to the deep ocean, implying small differences in temperature-induced ocean stratification changes between HR and LR. The OHU in the upper 250 m in SA is 3.4×10^{23} J in HR which is 12.1% less than that in LR. In contrast, $dOHU$ in the upper 250 m shows different characteristics in NR with 13.5% more heat in HR (solid red) than in LR (solid blue) while $dOHU$ below 250 m shows an opposite sign but is smaller. Therefore, a more stratified ocean in HR as shown in Figure 3.2d is mainly attributed to NR. In the following, the projected OHU in SA and NR will be discussed separately.

3.5.1. OHU Projection in SA

3.5.1.1. OHU Difference

Since the OHU in SA is nearly uniformly weaker in HR than LR from the surface to the seafloor, it is helpful to investigate the vertically integrated OHU in this region. To diagnose processes controlling OHU in SA, the heat budget shown in Eq.3.3 is used, where $y0=90^oS$, $y1=35^oS$, h is the depth of seafloor and SW is zero. As shown in Figure 3.8b, the difference in OHU in SA between HR (solid red) and LR (solid blue) increases with the increase in GHG forcing, which reaches -1.2×10^{23} J at 2100, about 19.3% of the OHU at 2100 in HR. In addition, MHT buffering ocean warming in SA by transporting heat equatorward in both HR (red dashed) and LR (blue dashed), which is in line with previous studies (Armour et al., 2016; Bryan et al., 2013; Liu et al., 2018). Similar to OHU, the difference of MHT-induced OHU also increases as GHG increases, which reaches -1.1×10^{23} J at 2100, accounting for 92% of the OHU difference between HR and LR at 2100. The summation of OHU induced by Q_{net} and MHT is shown as dot-dashed lines in Figure 3.8b. The consistency between OHU (solid) and the summation (dot-dashed) confirms the accuracy of our budget analysis and also implies that Q_{net} is the source of heat in SA under GHG forcing. Because MHT along the coast of Antarctic is zero, the OHU induced by MHT in SA is only determined by MHT across 35°S. Thus, we will focus on the vertically and zonally integrated MHT across 35°S in the following.

3.5.1.2. MHT across 35°S

As shown in Figure B12, the southward MHT across 35°S in HR PI-CNTL is -715.7 TW (1 TW= 10^{12} W) averaged over 100 years, 77.6% of which is attributed to mean-flow induced MHT (MMHT) where the mean flow is defined to be the 100-year mean. The breakdown of MMHT indicates that the southward transport occurs in the Indian Ocean (-1265.6 TW) countered by the northward MHT in the Pacific (432.0 TW) and Atlantic (278.4 TW). Forget and Ferreira (2019) provided the estimates of MHT across 30°S using ECCOv4 with -1330 TW, 220 TW and 290 TW in the Indian Ocean, the Pacific and the Atlantic, respectively. In addition, Ganachaud and Wunsch (2000) also estimated MHT using transoceanic section dataset from the WOCE program, showing MHT is -1500 TW, 600 TW, and 300 TW around 30°S in the Indian Ocean, the Pacific and the Atlantic, respectively. Comparing with those estimates, HR CESM generates reasonable MHT in each basin.

Figure 3.9a shows the MHT changes (ΔMHT) across 35°S in HR, as well as the decomposition of ΔMHT. Averaged over the 2000-2100 period, the southward MHT is weakened by 19.6% of the averaged value in PI-CNTL, and this weakening is dominated by the southward MMHT which is weakened by 26.1% of MMHT in PI-CNTL while the eddy induced MHT (EMHT) is enhanced only by 3% the EMHT in PI-CNTL, in agreement with Li et al. (2021). Although the weakening of MMHT occurs in all three basins, only the MMHT change (ΔMMHT) in the Indian Ocean (224.3 TW) is in the same direction with total ΔMMHT, and ΔMMHT in the Pacific and Atlantic are southward (respective -59.1 TW and -20.4 TW).

Differences of ΔMHT between HR and LR are shown in Figure 3.9b. Comparing with LR, southward MHT in HR is reduced more by 35.8 TW, which is attributed to ΔMMHT (54.9 TW) while the EMHT change (ΔEMHT) counters ΔMMHT by -19.1 TW. In the Indian Ocean, the difference of ΔMMHT is 99.8 TW, indicating the southward MMHT is more weakened in HR than LR. In comparison, the difference of ΔMMHT in the Atlantic (14.5 TW) is in line with the Indian Ocean but 7 times smaller. The positive difference in the Atlantic implies a weaker reduction of northward MMHT in HR than LR, showing different physics with the Indian Ocean. In the Pacific, ΔMMHT in LR is close to zero, leading to the negative difference of ΔMMHT.

ΔMMHT can be further partitioned into temperature-change induced and circulation-change induced components as following,

$$[(\bar{v}\bar{T})_{tnst} - (\bar{v}\bar{T})_{cntl}] = [(\bar{v}_{tnst} - \bar{v}_{cntl} + \bar{v}_{cntl})(\bar{T}_{tnst} - \bar{T}_{cntl} + \bar{T}_{cntl}) - (\bar{v}\bar{T})_{cntl}] = [\bar{v}_a\bar{T}_a + \bar{v}_a\bar{T}_{cntl} + \bar{v}_{cntl}\bar{T}_a] = [\bar{v}_a\bar{T}_{tnst} + \bar{v}_{cntl}\bar{T}_a]. \tag{3.5}$$

Overbar represents 100-year mean fields and subscript *a* denotes deviation from this mean. Since the nonlinear term $\bar{v}_a\bar{T}_a$ is small with the definition of mean fields here, it will be combined with $\bar{v}_a\bar{T}_{cntl}$ to guarantee the decompositions add up to the total, named $\bar{v}_a\bar{T}_{tnst}$. Therefore, the first and second term on the rightmost are the circulation-change induced and temperature-change induced ΔMMHT. For convenience, we will refer the former as to $V\Delta MMHT$ and the latter as to $T\Delta MMHT$.

The summary of $V\Delta MMHT$ and $T\Delta MMHT$ in HR is shown in the fourth row of Figure 3.9a. revealing $V\Delta MMHT$ and $T\Delta MMHT$ compensate each other in all three basins. The ratio of the amplitude of $T\Delta MMHT$ over $V\Delta MMHT$ varies from the Indian Ocean to the Pacific, and the Atlantic with respective values of 5.2%, 42.5%, and 77.8%, implying the impact of temperature changes on ΔMMHT is smallest in the Indian Ocean than the other two basins. To some extent, the importance of temperature changes can also be confirmed by the nonlinear term $\bar{v}_a\bar{T}_a$, which is 1.8 TW, -9.7 TW, and -12.6 TW in the Indian Ocean, the Pacific, and the Atlantic, respectively. Since the sign of $V\Delta MMHT$ is the same as ΔMMHT in three basins, it is valuable to decompose $V\Delta MMHT$ into gyre and meridional overturning circulation (MOC) components where MOC is defined as zonal mean in each basin. The division of $V\Delta MMHT$ indicates MOC changes dominate $V\Delta MMHT$ in three basins (last row of Figure 3.9a) while the contributions by gyre changes is only 13.0%, 11.5%, and 0.1% of that by MOC changes in the Indian Ocean, the Pacific, and the Atlantic, respectively. Due to the relative importance of $T\Delta MMHT$ in the Atlantic, a similar decomposition into MOC and gyre contributions indicates 98.9% of $T\Delta MMHT$ in HR is induced by MOC with the mean MOC transporting temperature anomalies northward.

The difference of $V\Delta MMHT$ and $T\Delta MMHT$ between HR and LR ($dV\Delta MMHT$ and $dT\Delta MMHT$) are demonstrated in the fourth row of Figure 3.9b. The difference of ΔMMHT is explained by circulation changes in the Indian Ocean and the Pacific, but by temperature changes in the Atlantic. In the Indian Ocean, $dV\Delta MMHT$ can reach 113.5 TW which is compensated by 13.7 TW from $T\Delta MMHT$. Furthermore, MOC and gyre induced $dV\Delta MMHT$ are 99.6 TW and 13.9 TW, respectively, revealing the importance of MOC changes in generating different ΔMMHT in HR and LR in the Indian Ocean. Similar results are also obtained in the Pacific where the difference of gyre component is only -0.3 TW, indicating the similarity of gyre contributions to MHT changes between HR and LR in the Pacific. By comparison, $dT\Delta MMHT$ is stronger than $dV\Delta MMHT$ in the Atlantic, where MOC induced $dT\Delta MMHT$ is 11.6 TW and gyre induced $dT\Delta MMHT$ is 21.5 TW, highlighting the inconsistency of impacts of gyre and MOC changes on MHT between HR and LR in the Atlantic. Since the net difference of ΔMMHT in the Atlantic is much smaller than the Indian Ocean, the detailed HR and LR comparison of circulations in the South Atlantic is beyond the scope of this work.

In summary, 92.0% of the full-depth integrated OHU difference between HR and LR in SA is explained by MHT while only 8.0% is explained by the net surface heat flux. The southward MHT across 35^{o}S is reduced more in HR than LR under GHG forcing, which is mainly attributed to the strong reduction of southward mean-flow induced MHT (i.e., MMHT) in the Indian Ocean. Moreover, the difference of MMHT changes between HR and LR in the Indian Ocean is controlled by circulation changes, especially the meridional overturning circulation.

3.5.2. OHU Projection in NR

MHT is the key connection between OHU in SA and NR. Once more heat in SA is transported into NR, vertical processes in NR will redistribute it (Morrison et al., 2015). Although there is more heat transported into NR from SA in HR, that heat is stored only in the upper 250 m as shown in Figure 3.8a. To diagnose the responsible processes, heat budget is applied to the upper 250 m in NR. Due to the unavailability of vertical profiles of parameterized MHT in LR and vertical mixing in HR, MHT integrated in the upper 250 m will be combined with vertical mixing calculated as the residual. Figure 3.10a demonstrates heat balance in HR where OHU increases continually from 2000 to 2100 at the rate of 7.3×10^{21} J per year (red), which is attributed to atmosphere forcing (magenta) while other processes including VHT (blue), MHT and mixing (cyan) tend to cool down the upper 250 m. The role of each process is similar to the globally averaged results shown earlier (Figure 3.3a).

The difference in the heat budgets between HR and LR is shown in Figure 3.10b. There is 3.6×10^{22} J more heat in HR than LR averaged over the 2000-2100 period (red) mainly contributed by VHT and Q_{net} with values of 8.9×10^{22} J and 1.7×10^{22} J, while the cooling from MHT and mixing is stronger in HR than LR (cyan), compensating the warming induced by VHT and Q_{net}. Moreover, the correlation coefficient of OHU difference and the VHT component is 0.84 from 2000 to 2100 while that associated with Q_{net} is 0.60, indicating VHT at 250 m is more important than Q_{net} in generating OHU differences in NR with the consideration of internal variabilities. Details of VHT in NR are discussed in the following.

The climatological decomposition of VHT in PI-CNTL NR is shown in Figure 3.11a. Similar to globally averaged results (Figure 3.6a), MVHT is downward (dot-dashed) while EVHT is upward (dashed). On the other hand, the total VHT in NR differs from that in Figure 3.6a under 100 m, where VHT in NR is downward while that in Figure 3.6a is upward, implying the strength of MVHT relative to EVHT performs differently in NR and SA with the downward MVHT stronger than the upward EVHT in NR while it is opposite in SA.

Figure 3.11b shows VHT changes over 2000-2100 in NR, indicating downward VHT at 250 m is strengthened (solid) by 0.09 PW in HR and 0.15 PW in LR. Furthermore, downward MVHT is weakened by 0.09 PW in HR and 0.07 PW in LR (dot-dashed) which is different from globally averaged MVHT changes. The difference of MVHT changes between NR and global average suggests the downward MVHT is strongly enhanced in SA. But the difference of MVHT changes between HR and LR is small in NR, as well as global average. Moreover, the upward EVHT is weakened by 0.17 PW in HR and but by 0.23 PW in LR (dashed), which explains ~50% of global EVHT changes. Therefore, the positive difference of VHT changes between HR and LR is mainly attributed to EVHT instead of MVHT, which is consistent with the global results discussed in Section 3.4.

3.6. OHU Projection in the Arctic

Section 3.5 provides a thorough description of OHU differences between HR and LR in SA and NR which is defined based on the zonal integration. Due to the small volume of the Arctic (65^oN-90^oN), it does not stand out in the zonally integrated OHU result. But it is more evident in the spatial distributions of the OHU difference as shown in Figure 3.7a. Further calculation indicates the Arctic accounts for 26.32% of total OHU difference in NR although its volume is only 4% of total volume of NR in the upper 250 m, suggesting the Arctic is the most dominant region in generating OHU differences between HR and LR. In this section, we will investigate in more details about the OHU projection difference between HR and LR in the Arctic.

The vertical profiles of OHU in NR shown in Figure 3.8a can be further divided into 35^{o}S-65^{o}N and the Arctic, which are illustrated in Figure B13. OHU in the Arctic is stronger in HR than LR distributed from the surface to the seafloor although the difference gets smaller and smaller as depth increases. Therefore, it is reasonable to investigate the OHU integrated from the surface to the bottom, which is similar to the discussion in SA. As shown in Figure 3.12, OHU difference between HR and LR becomes larger and larger (red and blue solid) as time increases, and the OHU in HR is 69.54% stronger than in LR averaged over the 2000-2100 period and doubles the value in LR by the end of 2100. In HR, the increased OHU (red solid) is mainly attributed to MHT process (red dashed) whereas the contribution from Q_{net} is almost zero which can be estimated by the difference between the dot-dashed and dashed red line in Figure 3.12. In contrast, the OHU change in LR (solid blue) is attributed to Q_{net} whilst MHT generates cooling effect (dashed blue), suggesting the fundamental differences of mechanisms regulating MHT changes in HR and LR in the Arctic. Mahlstein and Knutti (2010) also proposed MHT contributes to the uncertainty of Arctic warming in climate models. Burgard and Notz (2017) found the Arctic warming is attributed to net surface flux in 11 of 26 CMIP5 models and MHT in another 11 models, which underlies the uncertainties of the cause of Arctic warming in climate models. Therefore, it is beneficial to provide a thorough comparison of MHT changes between HR and LR.

Figure B14a shows the evolution of MHT at 65^{o}N in HR and LR simulations from 2000 to 2100. In PI-CNTL, MHT is 240 TW in LR (blue dotted) and 340 TW HR (red dotted) on average. In terms of the projected change, little difference is found in LR between HF-TNST (blue solid) and PI-CNTL (blue dotted), while stronger MHT is shown in HR HF-TNST (red solid) comparing with HR PI-CNTL (red dotted). On average, MHT in HR is strengthened by 11.8% (40 TW) under GHG. In HR, MHT changes is attributed to MMHT with a value of 42 TW while ΔEMHT only compensates ΔMMHT by -2 TW (Figure 3.13a). The compensation between ΔEMHT and ΔMMHT is much stronger in LR, leading to weak ΔMHT (Figure 3.13b), As a result of the different compensation strength of ΔMMHT and ΔEMHT, the northward MHT is enhanced in HR but reduced in LR.

Since only zonally integrated EMHT is available in LR, it is not possible to further investigate ΔEMHT in different basins. But it is still valuable to dive into the details of ΔMMHT. As shown in Figure 3.13, ΔMMHT in the Pacific is three times larger in HR than LR with values of 16 TW and 5 TW, respectively. Further decompositions illustrate ΔMMHT in Pacific is fully explained by $T\Delta MMHT$ in HR and LR, implying the impartance of temperature changes and time mean velocity. In the Atlantic, ΔMMHT is 26 TW in HR and 24 TW in LR as a result of compensation between $T\Delta MMHT$ and $V\Delta MMHT$. Though ΔMMHT in the Atlantic behaves similarly in HR and LR, the role of

$T\Delta MMHT$ and $V\Delta MMHT$ are different. $V\Delta MMHT$ is 60 TW in HR but -5 TW in LR which is compensated by $T\Delta MMHT$, indicating the circulation change dominates ΔMMHT in HR while the temperature change is dominant in LR. The division of ΔMMHT in the Atlantic in HR CESM agrees with van der Linden et al. (2019) which is based on EC-Earth model although they performed the analysis at 70^{o}N instead of 65^{o}N.

The heat budget over 70^{o}N~90^{o}N shows consistent role of MHT with that over 65^{o}N~90^{o}N in HR, but Q_{net} becomes the sink of the ocean heat. In LR, MHT term works together with Q_{net} as the heat source over 70^{o}N~90^{o}N (Figure B15a), but it becomes a heat sink over a large region of 65^{o}N~90^{o}N. Over 70^{o}N~90^{o}N, MHT-induced warming is weaker in LR than HR. As shown in Figure B15b&c, ΔMHT at 70^{o}N is three times larger in HR than LR on average in 2000-2100, which is attributed to ΔMMHT in both the Pacific and the Atlantic. The contributions of temperature changes and circulation changes to ΔMMHT show a consistency between HR and LR, agreeing with van der Linden et al. (2019) as well. The changes of MHT contributions to OHU from 65^{o}N~90^{o}N to 70^{o}N~90^{o}N suggests the complexity of MHT changes around 65^{o}N. The time mean ΔMHT changes as a function of latitudes averaged over 2000-2100 in HR and LR are shown in Figure B16. The transition zone, defined as the latitude where ΔMHT changes sign, is around 60^{o}N in HR and 65^{o}N in LR, acting as the main cause of inconsistency of heat budget in 65^{o}N~90^{o}N and 70^{o}N~90^{o}N. However, ΔMHT is larger in HR than LR no matter which latitude we choose to define the Arctic, and thus more heat is transported into the Arctic in HR. In the future, more works need to be done to investigate the possible mechanisms controlling the transition zone in HR and LR.

3.7. Summary and Discussion

This Chapter investigated the impacts of horizontal model resolutions on the projected OHU based on iHESP CESM experiments. Compared with observations, OHU in the upper 700 m and 2000 m are more realistic in HR than LR during the historic period of 1960-2020. In terms of projected future changes, the OHU averaged over the entire ocean shows small differences between HR and LR. But vertical distributions of OHU show significant differences between HR and LR with more heat in the upper 250 m in HR and less heat below 250 m. Further analysis implies that the difference in EVHT is the key factor in generating the differences of vertical heat distributions between HR and LR.

Regional analysis shows that the zonally integrated OHU in the upper 250 m can be divided into two regions: to the north of 35^{o}S, i.e., NR, the OHU is larger in HR than LR, and to the south of 35^{o}S, i.e., SA, the OHU is smaller in HR than LR. In SA, OHU in HR is less than LR not only in the upper 250 m, but also in the deep ocean. Full-depth integrated heat budget analysis indicates that the OHU difference can reach 19.3% of OHU in HR at the end of 2100. 92.0% of the OHU difference between HR and LR is attribued to MHT differences while net surface heat flux has a minor influence on the OHU difference. Further analysis of MHT across 35^{o}S illustrates that the southward MHT is reduced more in HR than LR under GHG, mainly modulated by the larger reduction in the southward MMHT in the Indian Ocean and the less reduced northward MMHT in the Atlantic, although the contribution of the former is 7 times larger than that of the latter. The difference in MMHT changes between HR and LR in the Indian Ocean occurs primarily due to circulation-induced changes, especially the MOC change. In contrast, temperature changes are more important than circulation changes in the Atlantic, where MOC and gyre circulation both contribute to the difference of temperature change induced heat transport between HR and LR.

In NR, there is 13.5% more heat in HR than LR in the upper 250 m on averaged over the 2000-2100 period. Since more heat is transported into NR from SA in HR, the difference of downward VHT changes is vital to different heat structures in HR and LR in NR. Our results indicate that the downward VHT at 250 m is less strengthened in the future in HR than LR. Further decomposition shows that the upward EVHT is significantly less reduced in HR while MVHT changes at 250 m have small differences between HR and LR, which is consistent with the global average results.

The Arctic (65^oN-90^oN) is a special region where the OHU difference in the upper 250 m accounts for 26.3% of that in NR although the volume is only 4.0% of that of NR, implying stronger Arctic Amplification in HR which can influence the extreme weather in mid-latitudes (Francis and Vavrus, 2012). Our results show that the OHU difference monotonically decreases with depth in the Arctic. Similar to SA, the full-depth integrated heat budget indicates the MHT change modulates the OHU difference, where the northward MHT is strongly enhanced in HR but changes little in LR in the future as consequence of the compensiation between MMHT and EMHT. The ΔMMHT and ΔEMHT both show large differences across 65^oN between HR and LR, while the difference of ΔMMHT mainly takes place in the Pacific which is modulated by temperature changes. In the Atlantic, though ΔMMHT shows similarity in HR and LR, the circulation changes and temperature changes play an opposite role in ΔMMHT in HR and LR.

As discussed in Burgard and Notz (2017), the MHT change is an important factor to the uncertainty of Arctic warming in climate models, which is also confirmed by HR and LR CESM. A transition zone, where MHT changes from negative to positive, occurs near 60°N in HR and near 65°N in LR. Therefore, further investigation is needed to reveal the mechanism underlying the MHT changes within the transition zone to understand Arctic warming uncertainty.

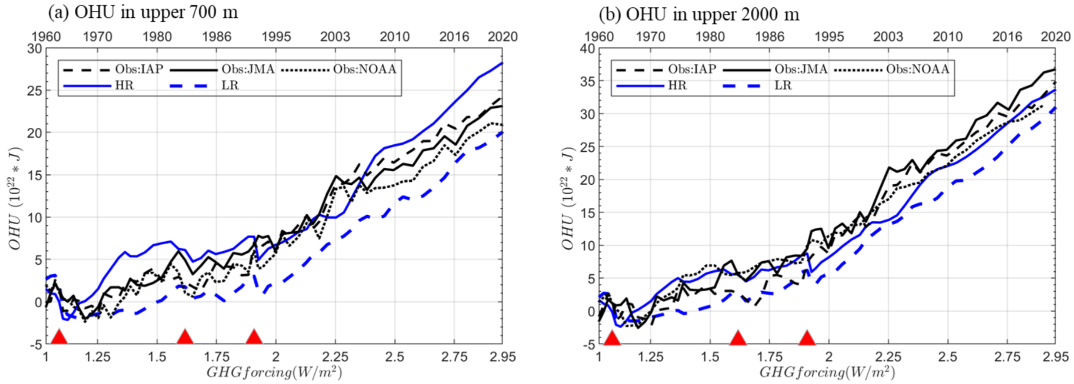

Figure 3.1 OHU in the upper **(a)** 700 m and **(b)** 2000 m from IAP (black dashed), JMA (black solid), NOAA (black dotted), HR (blue solid) and LR (blue dashed) CESM with the time mean over 1960-1970 as the baseline. Three largest volcanic eruptions in twentieth century are labeled with red triangles in 1963, 1982, and 1991 named as Agung, El Chichon, and Pinatubo, respectively.

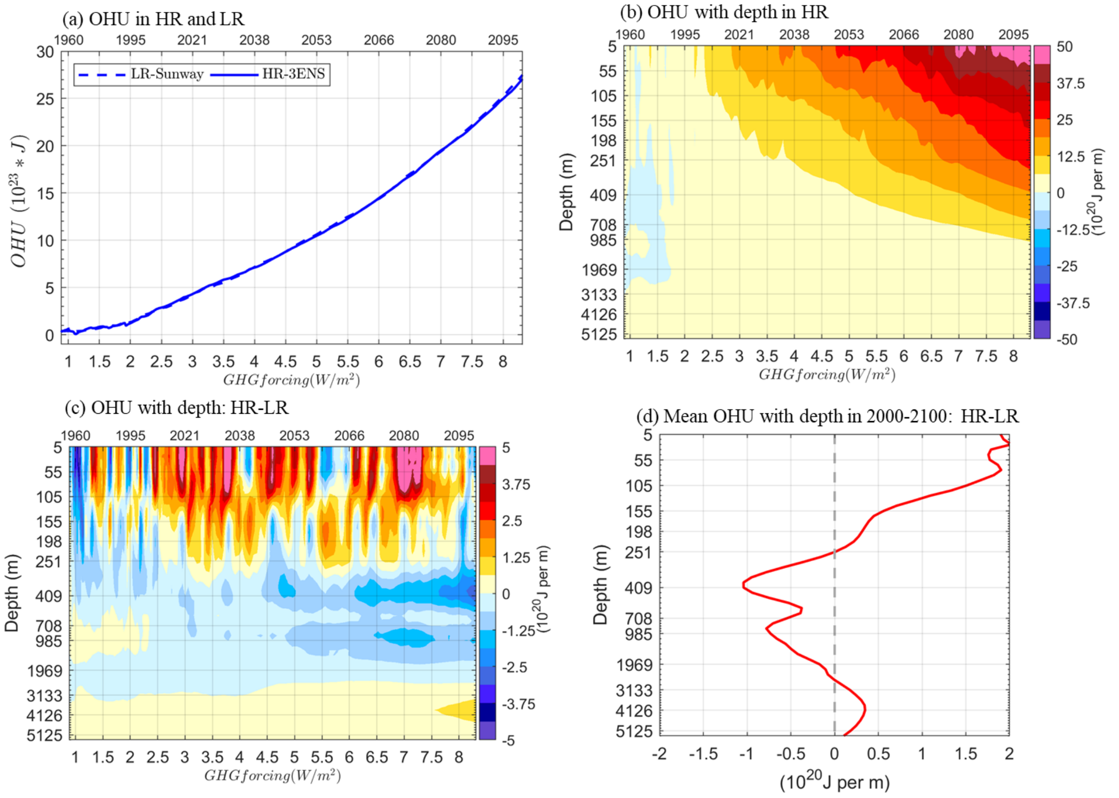

Figure 3.2 **(a)** OHU in LR (dashed) and HR (solid) CESM; **(b)** OHU as a function of depth in HR; **(c)** similar to (b) but for HR minus LR; **(d)** time-averaged OHU difference between HR and LR over 2000-2100.

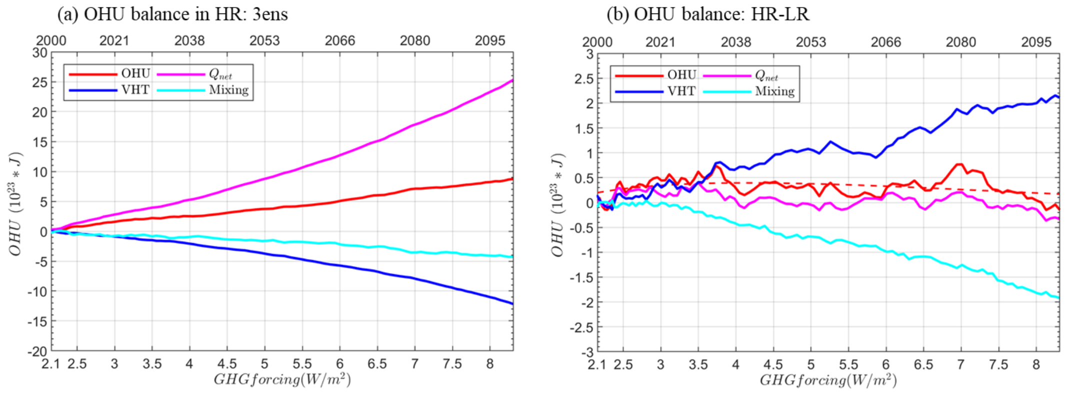

Figure 3.3 Globally averaged OHU balance in **(a)** HR CESM, **(b)** difference between HR and LR CESM, red for OHU, magenta for TFC, blue for VHTC, and cyan for mixing. Dashed red for OHU difference excluding internal variability.

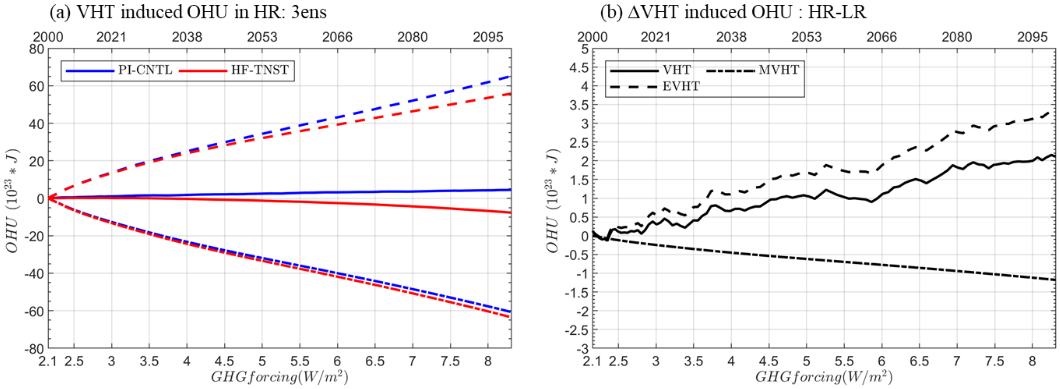

Figure 3.4 **(a)** OHU induced by VHT in HR PI-CNTL (blue) and HF-TNST (red); **(b)** Decomposition of VHT-induced OHU differences between HR and LR. Solid for total VHT, dot-dashed for MVHT, and dashed for EVHT.

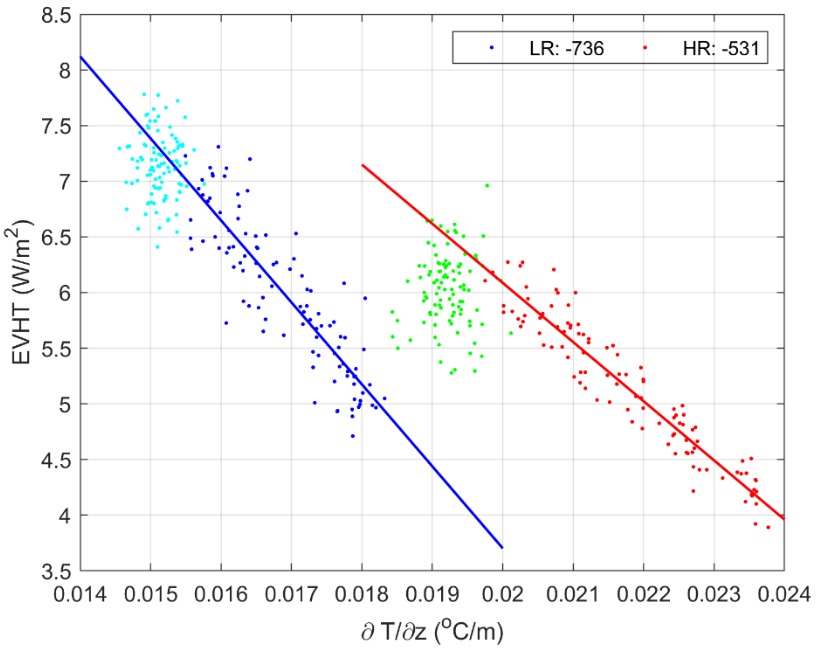

Figure 3.5 Scatterplot of globally averaged EVHT versus vertical temperature gradient in PI-CNTL LR (cyan), HR (green), and HF-TNST LR (blue), HR (red). The linear regression slope of EVHT and temperature gradient in HF-TNST are labeled in the legend.

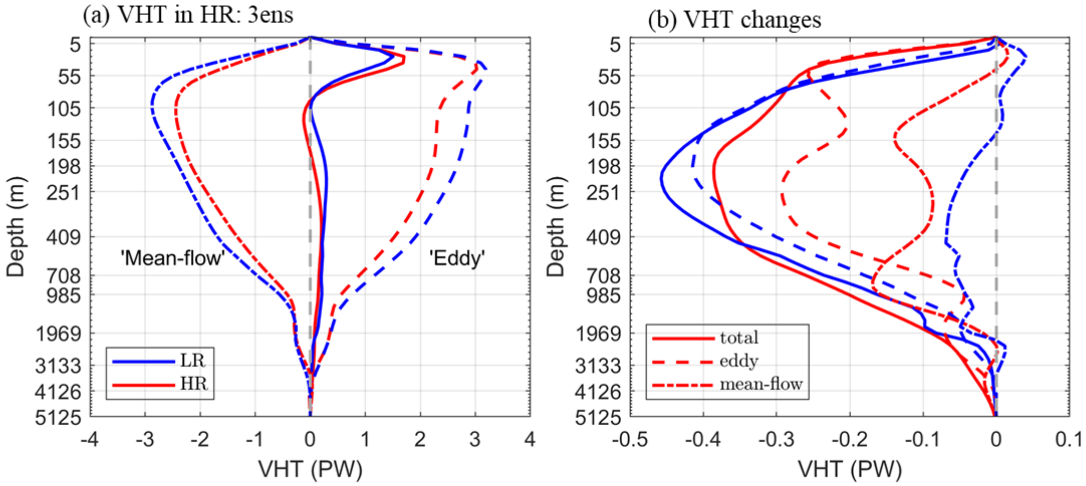

Figure 3.6 **(a)** total VHT (solid), mean-flow induced VHT (dot-dashed), eddy-induced VHT (dashed) in HR (red) and LR (blue) in PI-CNTL averaged over year 400-500; **(b)** changes of total VHT, MVHT, and EVHT between HR (red) and LR (blue) CESM averaged over 2000-2100.

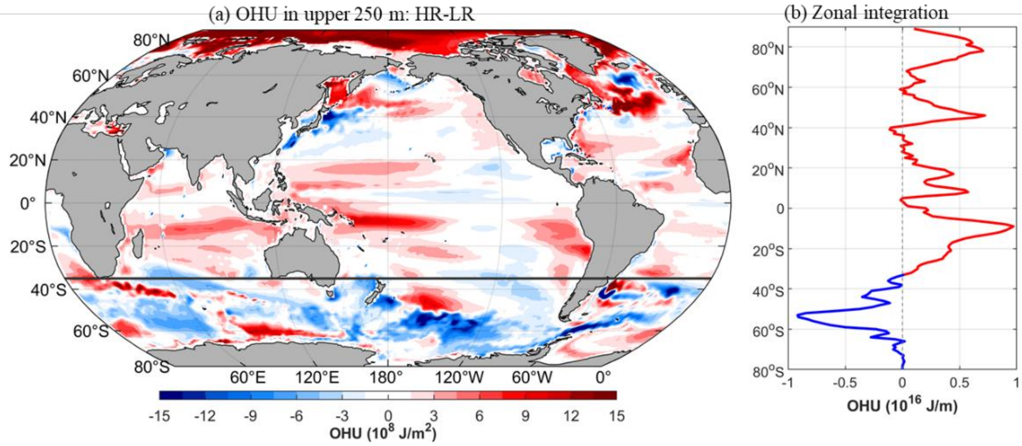

Figure 3.7 **(a)** OHU difference between HR and LR in the upper 250 m; **(b)** zonally integrated OHU difference in the upper 250 m, red (blue) for north (south) of 35^{o}S. Results are the average over 2000-2100.

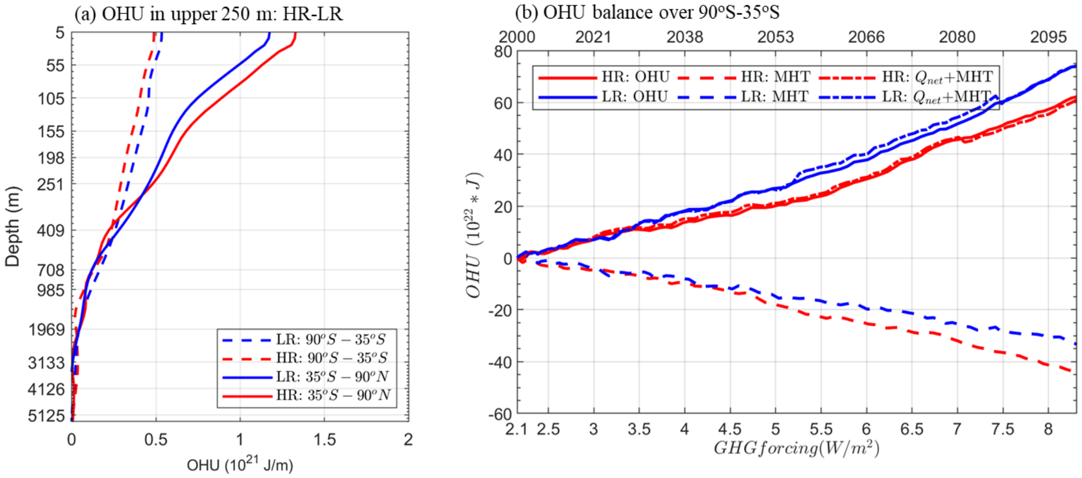

Figure 3.8 **(a)** Vertical profile of time-averaged OHU in 2000-2100 over 90ºS-35ºS (dashed) and 35ºS-90ºN (solid) in HR (red) and LR (blue); **(b)** heat balance over 90ºS-35ºS, solid for OHU, dashed for MHT induced OHU, and dot-dashed for the summation of MHT and Q_{net} induced OHU in HR (red) and LR (blue).

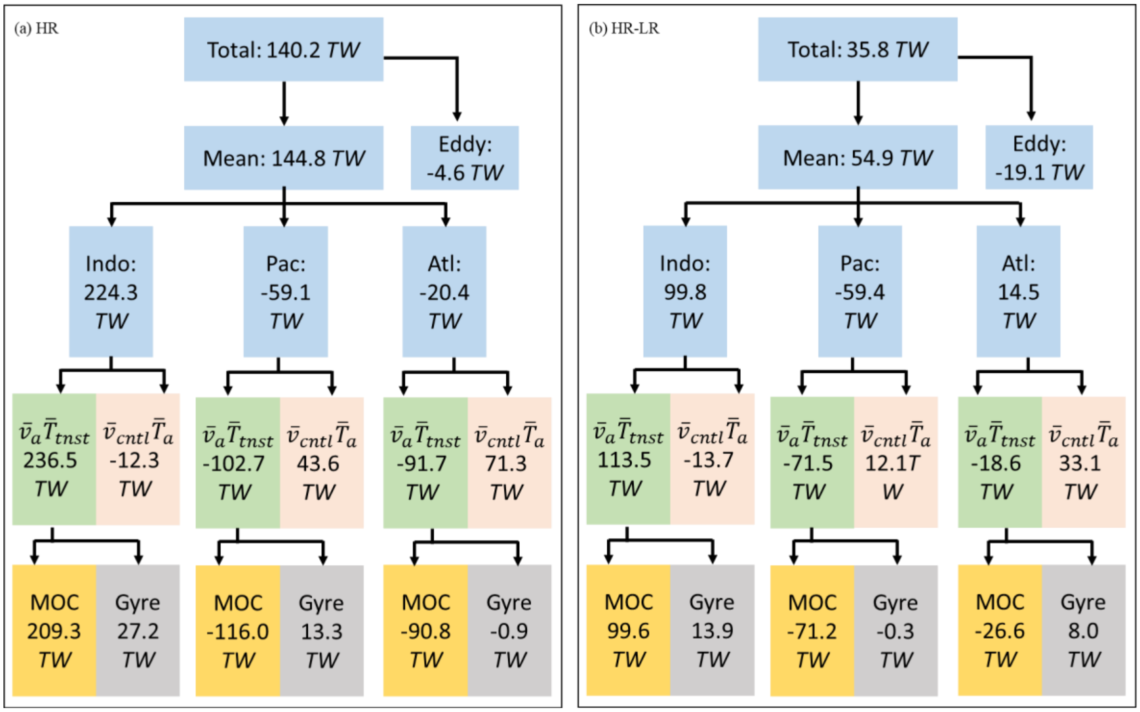

Figure 3.9 **(a)** MHT changes across 35ºS in HR; **(b)** difference of MHT changes between HR and LR.

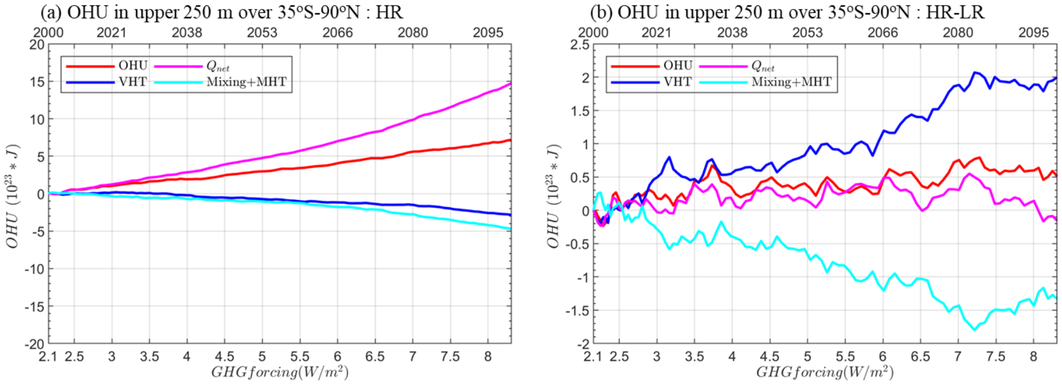

Figure 3.10 **(a)** Heat balance in the upper 250 m over 35^{o}S-90^{o}N (i.e., NR) in HR, red for OHU, magenta for Q_{net} induced OHU, blue for VHT induced OHU, and cyan for MHT and mixing indued OHU; **(b)** same with (a) but for the difference of HR and LR.

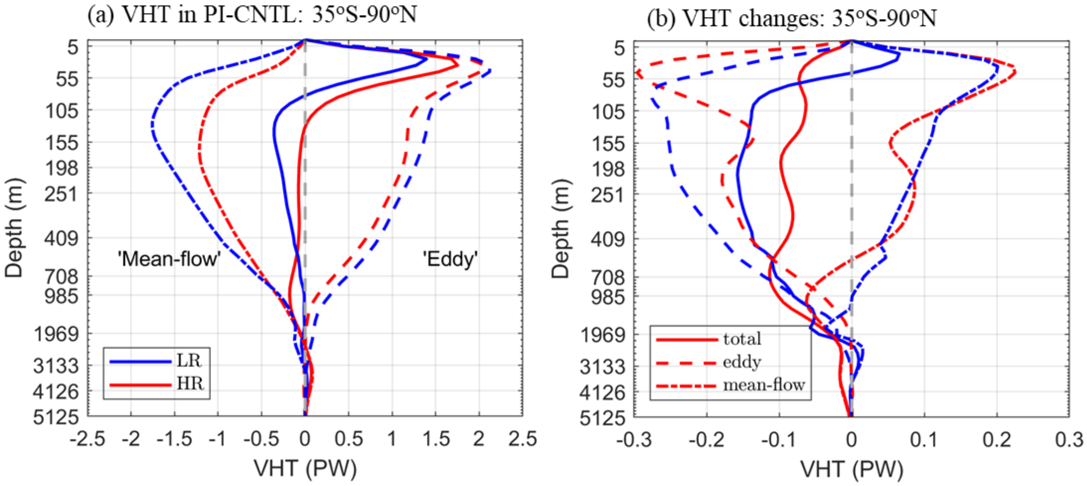

Figure 3.11 **(a)** VHT in NR averaged over year 400-500 in PI-CNTL; **(b)** VHT changes in NR. Red for HR, blue for LR, solid for total VHT, dashed for E VHT, and dot-dashed for MVHT.

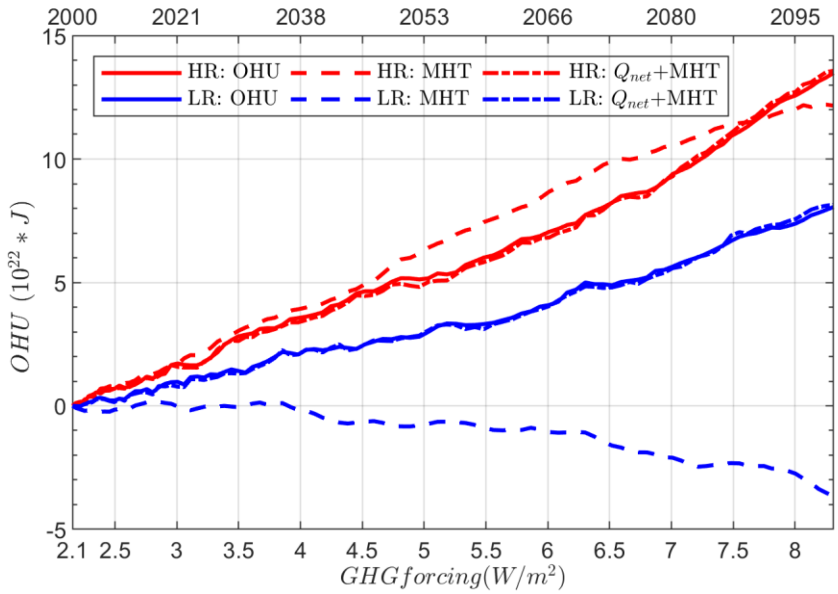

Figure 3.12 Heat balance over 65°N-90°N, solid for OHU, dashed for MHT induced OHU, and dot-dashed for the summation of MHT and Q_{net} induced OHU in HR (red) and LR (blue).

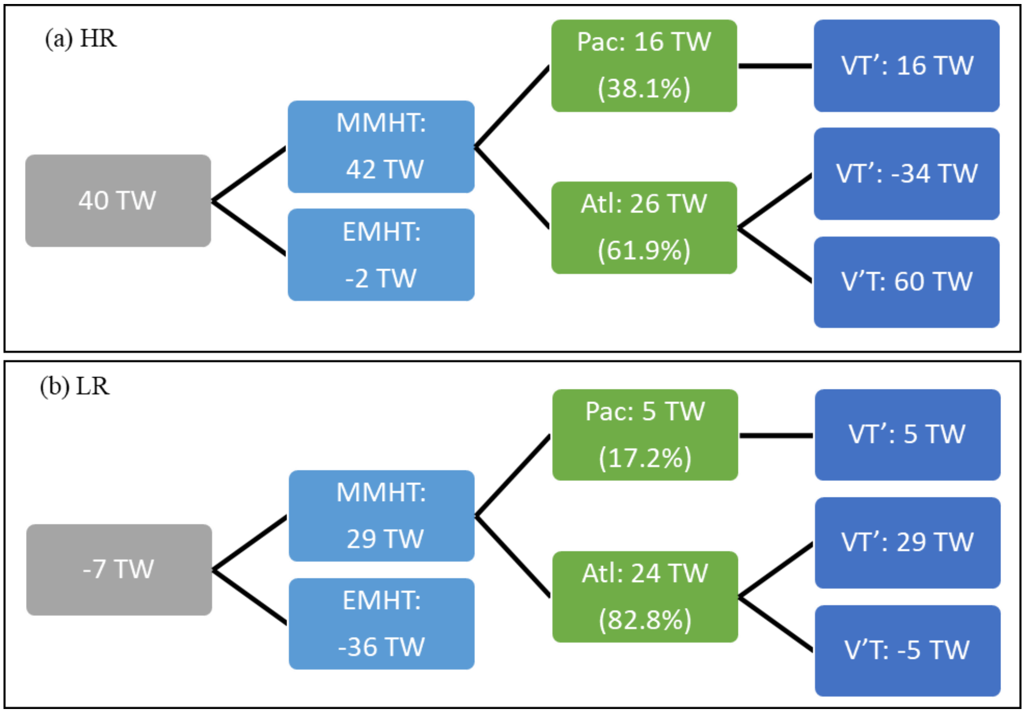

Figure 3.13 MHT changes across 65°N in **(a)** HR and **(b)** LR.

4. CONCLUSIONS AND FUTURE WORK

In order to reliably project future climate change at global and regional scales, realistic simulations of sea surface temperature and ocean heat uptake (OHU) are necessary. However, existing CMIP-class coarse resolution (LR, ~1^{o}) models have severe limitations in simulating them. In this dissertation, the advantages of high-resolution (HR, ~0.1^{o}) global climate models in simulating these important ocean variables are explored by comparing identical long-term HR and LR climate simulations. Improvements in SST simulation resulting from increased horizontal resolution are presented in Chapter II. Multi-model comparisons (ocean resolutions ranging from 1^{o} to 1/12^{o}) with observations have been used for this purpose. Then, a detailed investigation of the mechanisms behind SST biases in CESM simulations has been carried out from global average and regional perspective. The importance of KPP mixing in reducing SST biases in eddy-active regions is identified. With the availability of multi-century HR CESM transient climate simulations generated by iHESP, impacts of increasing model resolutions on OHU are explored in Chapter III. To evaluate the model performance, a comparison of model-simulated and observed OHU is performed. Contributions of different physical processes to heat redistributions in HR and LR are studied to understand the differences in projected OHU changes between HR and LR. The main conclusions draw from the detailed analysis in Chapter II and III of this dissertation are summarized below. An outline for future research on SST biases and OHU in global climate simulations based on the main outcomes of this dissertation are provided at the end.

4.1. Conclusions

4.1.1. Impacts of Model Horizontal Resolutions on SST Biases

A major finding from this dissertation work is that increasing model horizontal resolutions (from 1^o to $<0.25^o$) is confirmed to reduce SST biases, including the warm bias in EBUS and cold bias in the western basins and tropics. The consistency of improvements is revealed by multiple models, including CESM, HadGEM3-GC31, AWI-CM, ECMWF, and MPI-ESM1.2. The globally averaged SST in CESM is 1^oC warmer in HR than LR. The globally averaged heat budget indicates atmospheric fluxes (i.e., AFC) and oceanic vertical mixing (i.e., VMFC) dominate the near-surface heat balance in both HR and LR, while vertical advection (i.e., VHTC) plays a secondary role. AFC generates cooling in the upper 10 m because the warming induced by solar heat flux cannot completely compensate the cooling induced by nonsolar heat flux. Therefore, VMFC is important to close the balance by generating warming in the upper 10 m. VMFC is parameterized by KPP, which includes nonlocal and local mixing components. Further analysis indicates that the warming induced by vertical mixing is attributed to the nonlocal KPP mixing, which brings heat from the subsurface to the uppermost layer. The difference of globally averaged heat budget between HR and LR reveals that stronger solar heat flux and nonlocal vertical mixing account for the 1^oC warmer SST in HR. The importance of nonlocal vertical mixing in reducing SST bias is highlighted for the first time, which makes this work distinct from others.

The difference of 2-D surface ocean heat budget between HR and LR shows that the stronger nonlocal vertical mixing and solar heat flux in HR mainly occur in eddy-active regions and the tropics. In eddy-active regions, the nonlocal vertical mixing contributes the most to the warmer SST in HR, followed by the advection and solar heat flux. Based on the formula of nonlocal KPP flux, it is found that the stronger nonlocal vertical mixing is mainly induced by the direct impact of nonsolar heat flux instead of indirect impact via shape function in a nonlinear manner. In the tropics, nonlocal vertical mixing and solar heat have similar contributions to warmer SST in HR, which is consistent with globally averaged results. Different from eddy-active regions, both the direct and indirect impact of nonsolar heat flux on nonlocal KPP flux are important in the tropics, accounting for 60% and 40% of the nonlocal KPP flux difference, respectively. In both eddy-active regions and the tropics, the difference of the other important process, solar heat flux, is likely induced by the cloud difference, which may be related to model resolution impacts on cloud parameterization.

Combining with the recent findings by Jing et al. (2020), we proposed a physical mechanism explaining the nonlinear relationship between nonsolar heat flux and nonlocal KPP flux as follows. A stronger heat loss at the surface leads to a stronger upward eddy heat transport, $w'T'$, in HR through turbulent thermal wind balance (Jing et al., 2020). $w'T'$ peaks around 50 m and decreases to zero at the surface, which causes a strong heat convergence between 10 m and 50 m in the vertical direction, and a warming in this region. Meanwhile, the strong surface heat loss causes convective instability near the surface, strengthening nonlocal vertical mixing at 10 m and bringing warmer temperature between 10 m and 50 m to the surface layer. This process is absent in LR because eddies and sharp fronts are absent and turbulent thermal wind balance is not operating. Therefore, this work further advances the theory of Jing et al. (2020) by identifying the important role of nonlocal KPP mixing in SST simulations.

4.1.2. Impacts of Model Horizontal Resolutions on Ocean Heat Uptake

The assessment of globally averaged ocean heat uptake (i.e., OHU) in HR and LR reveals that simulated OHU in the upper 700 m and 2000 m are more realistic in HR than LR during the 1960-2020 period. In terms of future projection, the depth-integrated OHU in HR and LR shows little differences. But large differences can be seen in the vertical heat distributions, showing larger OHU in the upper 250 m in HR and smaller OHU below 250 m. In HR and LR, the net surface heat flux is the heat source of the upper 250 m while vertical heat transport (i.e., VHT) and vertical mixing transport the heat to the deep ocean under GHG forcing. The more downward VHT in the future is a result of more downward mean-flow induced VHT (i.e., MVHT) and less upward eddy induced VHT (i.e., EVHT). Regarding the HR and LR difference, the larger OHU in the upper 250 m in HR is attributed to VHT caused by the less reduced upward EVHT in HR than LR. Further analysis indicated that the weakening of upward EVHT at 250 m is a result of stronger sensitivity of EVHT to the enhanced ocean stratification in LR than HR, implying a fundamental difference between resolved and parameterized EVHT response to future ocean warming. The identification of the importance of EVHT in generating different vertical structures of OHU between HR and LR makes this work distinct from other OHU studies.

The comparison of zonally integrated OHU within the upper 250 m shows larger OHU in HR to the north of 35°S (i.e., NR) and weaker OHU in HR to the south of 35°S (i.e., SA). In SA, less OHU in HR is found not only in the upper 250 m, but also in the deep ocean. The OHU difference between HR and LR integrated from the surface to the seafloor can reach to 19.3% of the OHU in HR at the end of 2100, 92.0% of which is explained by the meridional heat transport (i.e., MHT) difference and 8.0% is explained by the net surface heat flux. The southward MHT across 35ºS is more reduced in HR than LR under GHG forcing as a result of the stronger reduction of southward mean-flow induced MHT (i.e., MMHT) in the Indian Ocean and the less reduced northward MMHT in the Atlantic. The contribution of the Indian Ocean MMHT is seven times larger than the Atlantic. Moreover, the difference of MMHT changes in the Indian Ocean between HR and LR is controlled by the difference in circulation change, especially the change in meridional overturning circulation. In contrast to the Indian Ocean, temperature changes dominate the difference of MMHT changes in the Atlantic. In NR, there is 13.5% more anthropogenic heat in HR than LR in the upper 250 m averaged over the 2000-2100 period. Similar to globally averaged results, different vertical structures between HR and LR in NR are also attributed to the difference in EVHT.

The Arctic (65ºN-90ºN) is a special region where the OHU differences in the upper 250 m account for 26.3% of those in NR although the volume of the Arctic is only 4.0% of the NR volume. The OHU differences in the Arctic monotonically decrease with depth. The heat budget for the whole water column in the Arctic suggests the MHT changes control the OHU differences between HR and LR. Further analyses of MHT show the northward MHT across 65ºN is strongly enhanced in HR but has small changes in LR under GHG forcing. The difference of changes in MHT across 65^{o}N between HR and LR is mainly caused by MMHT in the Pacific, which is governed by temperature changes advected by the time-mean circulation

4.2. Future Work

Although results in this dissertation have advanced our understanding of SST biases and OHU projection using HR and LR CESM, there are still some limitations of current study. This section aims to list these limitations and the further analyses needed to be conducted to test the robustness of the results found in this dissertation.

In Chapter II, we proposed the mechanism which demonstrates how nonlocal KPP mixing responds to surface cooling. Although LR sensitivity experiments show response of nonlocal vertical mixing flux to vertical heat transport which is supportive of this mechanism, the strength of the response is relatively small, and thus the robustness of the finding needs further studies. One possible reason is that the parameterized vertical heat transport lacks the direct response to surface cooling induced by synoptic winter storms as proposed in Jing et al. (2020). To further verify this mechanism, composite analyses should be performed in the future, using 3-D daily model output in HR to examine the time evolution of the nonlocal KPP mixing development in response to synoptic winter storms.

In Chapter III, the sensitivity of EVHT to changes of ocean stratification is shown to be stronger in LR than HR, leading to strong reduction of EVHT at 250 m in LR. But the analysis is based on global average. Since the EVHT strength varies spatially and seasonally, it is beneficial to conduct regional and seasonal comparisons of the response of EVHT to ocean stratification changes in HR and LR. Additionally, since the parametrized EVHT in LR is obtained based on the horizontal temperature gradient, it is useful to compare the relationship between EVHT and horizontal temperature gradient in HR and LR to further evaluate the parameterized EVHT.

The discussion of MHT across 35^{o}S confirmed the importance of MOC changes in determining the HR and LR difference of MHT changes in the Indian Ocean in Chapter III. As shown in Ma et al. (2020), the change of Agulhas current in the Southern Indian Ocean compensates the change of Indonesian throughflow (ITF), which connects the Pacific to the Indian Ocean. Future works are needed to address the impacts of ITF on the HR and LR difference of MOC changes in the Indian Ocean.

APPENDIX A

SUPPLEMENTARY FIGURES FOR CHAPTER 2

Table A1 Model information of 25 models in CMIP5 piControl simulations

Model name	Nation	Atmospheric model Atmosphere resolution	Ocean model Ocean resolution
ACCESS1-0	Australia	HadGEM2 r1.1 N96 (~1.875˚ x 1.25˚); 38 levels	MOM4p1 Nominal 1˚ x 1˚; 50 levels
ACCESS1-3	Australia	Global Atmosphere 1.0 N96 (~1.875˚ x 1.25˚); 38 levels	MOM4p1 Nominal 1˚ x 1˚; 50 levels
CanESM2	Canada	CanAM4 ~2.8˚ x 2.8˚; 35 levels	CanOM4 256 x 192 longitude/latitude; 40 levels
CMCC-CESM	Italy	ECHAM5 T159 (0.75˚ x 0.75˚); 31 levels	OPA8.2 2˚ average, 0.5˚ at the equator; 31 levels
CMCC-CM	Italy	ECHAM5 T159 (0.75˚ x 0.75˚); 31 levels	OPA8.2 2˚ average, 0.5˚ at the equator; 31 levels
CNRM-CM5	France	ARPEGE-Climat V5.2.1 T127 (~1.4˚x1.4˚); 31 levels	NEMO 3.2 ~1˚ x 1˚; 42 levels
CSIRO-Mk3-6-0	Australia	AGCM v7.3.4 T63 (~1.875˚x1.875˚); 18 levels	MOM2.2 ~1.875˚x0.9375˚; 31 levels
GFDL-CM3	USA	AM3 2.5˚ x 2˚; 48 levels	MOM4p1 Tripolar 360 x 200; 50 levels
GFDL-ESM2G	USA	AM2 2.5˚ x 2˚; 24 levels	TOPAZ1p2 Tripolar 360 x 210; 63 levels
GISS-E2-H	USA	Included 2.5˚ x 2˚; 40 levels	HYCOM Ocean 1˚ longitude x 1˚ latitude HYCOM; 26 levels
GISS-E2-R	USA	Included 2.5˚ x 2˚; 40 levels	Russell Ocean 1.25˚ x 1˚; 32 levels
HadGEM2-CC	UK	HadGAM2 N96 (1.875˚x1.25˚); 60 levels	HadGOM2 1˚ longitude x 0.3˚ to 1˚ latitude; 40 levels

Table A1 Continued

Model name	Nation	Atmospheric model Atmosphere resolution	Ocean model Ocean resolution
HadGEM2-ES	UK	HadGAM2 N96 (1.875˚x1.25˚); 38 levels	HadGOM2 1˚ longitude x 0.3˚ to 1˚ latitude; 40 levels
INM-CM4	Russia	Included 2˚ x 1.5˚; 21 levels	Included 1˚ x 0.5˚; 40 levels
IPSL-CM5A-LR	France	LMDZ5 95 x 96 equivalent to 3.75˚x1.9˚; 39 levels	NEMO 3.2 2˚ longitude x 0.5˚ to 2˚ latitude; 31 levels
IPSL-CM5A-MR	France	LMDZ5 143 x 144 equivalent to 1.25˚x2.5˚; 39 levels	NEMO 3.2 2˚ longitude x 0.5˚ to 2˚ latitude; 31 levels
IPSL-CM5B-LR	France	LMDZ5 95 x 96 equivalent to 3.75˚x1.9˚; 39 levels	NEMO 3.2 2˚ longitude x 0.5˚ to 2˚ latitude; 31 levels
MIROC5	Japan	MIROC-AGCM6 T85 (1.40625˚x1.40625˚); 40 levels	COCO4.5 1.4˚ longitude x 0.5˚-1.4˚ latitude; 50 levels
MIROC-ESM	Japan	MIROC-AGCM T42 (2.8125˚x2.8125˚); 80 levels	COCO3.4 1.4˚ longitude x 0.5˚-1.4˚ latitude; 44 levels
MPI-ESM-LR	Germany	ECHAM6 T63 (~1.8˚x1.8˚); 47 levels	MPIOM Average 1.5˚; 40 levels
MPI-ESM-MR	Germany	ECHAM6 T63 (~1.8˚x1.8˚); 95 levels	MPIOM ~0.4˚x 0.4˚; 40 levels
MPI-ESM-P	Germany	ECHAM6 T63 (~1.8˚x1.8˚); 47 levels	MPIOM Average 1.5˚; 40 levels
MRI-CGCM3	Japan	MRI-AGCM3.3 TL159 (320x160); 48 levels	MRI.COM3 1˚ x 0.5˚; 50 levels + 1 bottom boundary layer
NorESM1-M	Norway	CAM4-Oslo 2.5˚x 1.9˚; 26 levels	NorESM-Ocean 1.125˚along the equator; 53 levels
NorESM1-ME	Norway	CAM4-Oslo 2.5˚x 1.9˚; 26 levels	NorESM-Ocean 1.125˚along the equator; 53 levels

Table A2 Model information of 34 models in CMIP6 piControl simulations

Model name	Nation	Atmospheric model Atmosphere resolution	Ocean model Ocean resolution
ACCESS-CM2	Australia	HadGEM2 r1.1 N96 (~1.875˚ x 1.25˚); 38 levels	MOM4p1 Nominal 1˚ x 1˚; 50 levels
ACCESS-ESM1-5	Australia	Global Atmosphere 1.0 N96 (~1.875˚ x 1.25˚); 38 levels	MOM4p1 Nominal 1˚ x 1˚; 50 levels
AWI-ESM-1-1-LR	Germany	ECHAM6.3.04p1 T63 (~ 1.875° × 1.875°); 47 levels	FESOM 1.4 Unstructured grid in the horizontal with 126859 wet nodes; 46 levels
AWI-CM-1-1-MR	Germany	ECHAM6.3.04p1 T127 (~ 0.94° × 0.94°); 95 levels	FESOM 1.4 Unstructured grid in the horizontal with 830305 wet nodes; 46 levels
CanESM5	Canada	CanAM5 ~2.8˚ x 2.8˚; 49 levels	NEMO3.4.1 1° with refinement to 1/3° in 20° S–20° N; 45 levels
CESM2	USA	CAM6 Finite volume grid (0.9° × 1.25°); 32 levels	POP2 320 × 384 longitude/latitude; 60 levels
CESM2-WACCM	USA	CAM6 Finite volume grid (0.9° × 1.25°); 32 levels	POP2 320 × 384 longitude/latitude; 60 levels
CMCC-CM2-SR5	Italy	ECHAM5 T159 (0.75˚ x 0.75˚); 31 levels	OPA8.2 2˚ average, 0.5˚ at the equator;31 levels
CMCC-ESM2	Italy	ECHAM5 T159 (0.75˚ x 0.75˚); 31 levels	OPA8.2 2˚ average, 0.5˚ at the equator; 31 levels
CNRM-CM6-1	France	ARPEGE-Climat V5.2.1 T127 (~1.4˚x1.4˚); 31 levels	NEMO 3.2 ~1˚ x 1˚; 42 levels
CNRM-CM6-1-HR	Australia	AGCM v7.3.4 T63 (~1.875˚x1.875˚); 18 levels	MOM2.2 ~1.875˚x0.9375˚; 31 levels
EC-Earth3-Veg-LR	European countries	IFS cy36r4 TL159 (~ 125 km); 91 levels	NEMO3.6 Primarily 1°; 362 × 294 longitude/latitude; 75 levels
EC-Earth3-LR	European countries	IFS cy36r4 TL255 (~ 125 km); 62 levels	NEMO3.6 Primarily 1°; 362 × 294 longitude/latitude; 75 levels
EC-Earth3-CC	European countries	IFS cy36r4 TL255 (~ 70 km); 91 levels	NEMO3.6 Primarily 1°; 362 × 294 longitude/latitude; 75 levels
CNRM-ESM2-1	France	Arpege 6.3 T127 (~ 100 km); 91 levels	NEMO3.6 Primarily 1°; 362 × 294 longitude/latitude; 75 levels

Table A2 Continued

Model name	Nation	Atmospheric model Atmosphere resolution	Ocean model Ocean resolution
E3SM-1-0	USA	EAM v1.0 1° average grid spacing; 72 levels	MPAS-Ocean v6 Variable resolution 60–30 km; 60 levels
E3SM-1-1	USA	EAM v1.1 1° average grid spacing; 72 levels	MPAS-Ocean v6 Variable resolution 60–30 km; 60 levels
GFDL-CM4	USA	AM4.0.1 1˚ x 1˚; 33 levels	MOM6 Tripolar 0.25º; 1442 × 1080 longitude/latitude; 75 levels
GFDL-ESM4	USA	AM4.1 1˚ x 1˚; 49 levels	MOM6 Tripolar 0.5º; 720 × 576 longitude/latitude; 75 levels
GISS-E2-1-G	USA	GISS-E2.1 2.5˚ x 2˚; 40 levels	GISS Ocean 1.25° × 1°; 32 levels
GISS-E2-1-H	USA	GISS-E2.1 2.5˚ x 2˚; 40 levels	HYCOM Ocean ~ 1° × 1°; 26 levels
HadGEM3-GC31-LL	UK	MetUM-HadGEM3-GA7.1 N96 (1.875° × 1.25°); 85 levels	NEMO-HadGEM3-GO6.0 Primarily 1° with meridional refinement down to 1/3° in the tropics; 75 levels
HadGEM3-GC31-MM	UK	MetUM-HadGEM3-GA7.1 N216 (~ 0.83° × 0.55°); 85 levels	HadGOM2 1˚ longitude x 0.3˚ to 1˚ latitude; 40 levels
INM-CM4-8	Russia	INM-AM4-8 2˚ x 1.5˚; 21 levels	INM-OM5 360 x 318 longitude/latitude; 40 levels
INM-CM5-0	Russia	INM-AM5-0 2˚ x 1.5˚; 73 levels	INM-OM5 720 x 720 longitude/latitude; 40 levels
MIROC-ES2L	Japan	CCSR AGCM T42 (~ 2.8125° × 2.8125°); 42 levels	COCO4.9 Primarily 1°; 360 × 256 longitude/latitude; 63 levels
MPI-ESM1-2-HAM	Germany	ECHAM6.3 T63 (~1.8˚x1.8˚); 47 levels	MPIOM1.63 ~1.5˚; 40 levels
MPI-ESM1-2-LR	Germany	ECHAM6.3 T63 (~1.8˚x1.8˚); 47 levels	MPIOM1.63 ~1.5˚; 40 levels
MPI-ESM1-2-HR	Germany	ECHAM6.3 T127 (0.94° × 0.94°); 95 levels	MPIOM1.63 Approximately 0.4°; 802 × 404 longitude/latitude; 40 levels
MRI-ESM2-0	Japan	MRI-AGCM3.5 TL159 (320x160); 80 levels	MRI.COM4.4 ~1˚ x 0.5˚; 360 x 364 longitude/latitude; 61 levels
NorCPM1	Norway	CAM-OSLO4.1 ~ 2.5° × 2; 26 levels	MICOM1.1 1˚; 320 × 384 longitude/latitude; 53 levels

Table A2 Continued

Model name	Nation	Atmospheric model Atmosphere resolution	Ocean model Ocean resolution
NorESM1-F	Norway	CAM4 ~ 2.5° × 2°; 32 levels	MICOM 1°; 360 × 384 longitude/latitude; 70 levels
NorESM2-MM	Norway	CAM-OSLO ~1°; 70 levels	MICOM 1°; 360 × 384 longitude/latitude; 70 levels
UKESM1-0-LL	UK	MetUM-HadGEM3-GA7.1 N96 (1.875° × 1.25°); 85 levels	NEMO-HadGEM3-GO6.0 Primarily 1° with meridional refinement down to 1/3° in the tropics; 75 levels

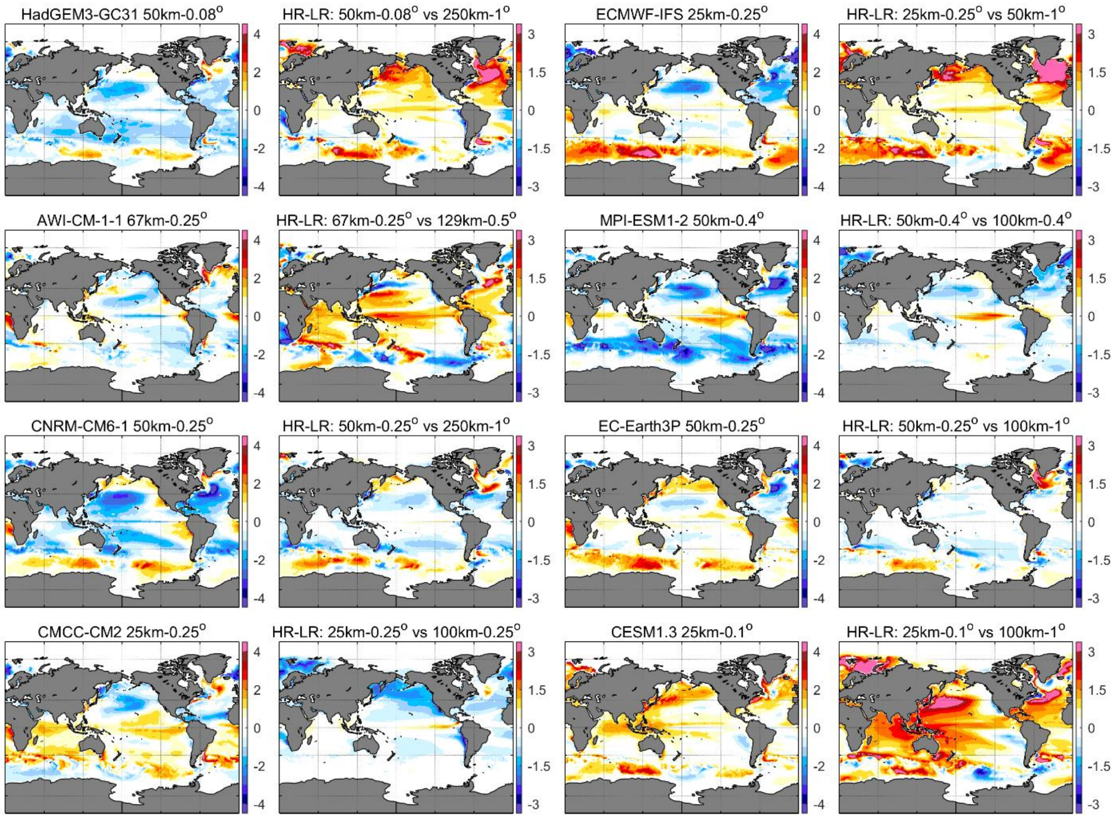

Figure A1 First column is the SST bias in CNTL-HR runs from HadGEM3-GC31, AWI-CM1-1, CNRM-CM6-1, CMCC-CM2, respectively. The second column is the SST difference between HR and LR corresponding with the models in the first column. The third column is similar to the first column but in ECMWF-IFS, MPI-ESM1-2, EC-Earth3P and CESM1.3, respectively. The last column the SST difference between HR and LR corresponding with the models in the third column (unit: ^{o}C). The observation is taken as the climatological SST in 1950-1960 from HadISST1.0.

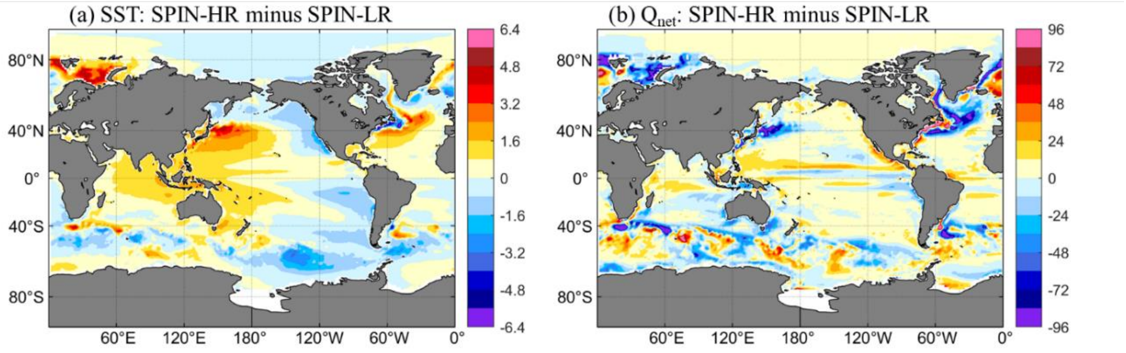

Figure A2 Differences of **(a)** SST and **(b)** Qnet between SPIN-HR and SPIN-LR.

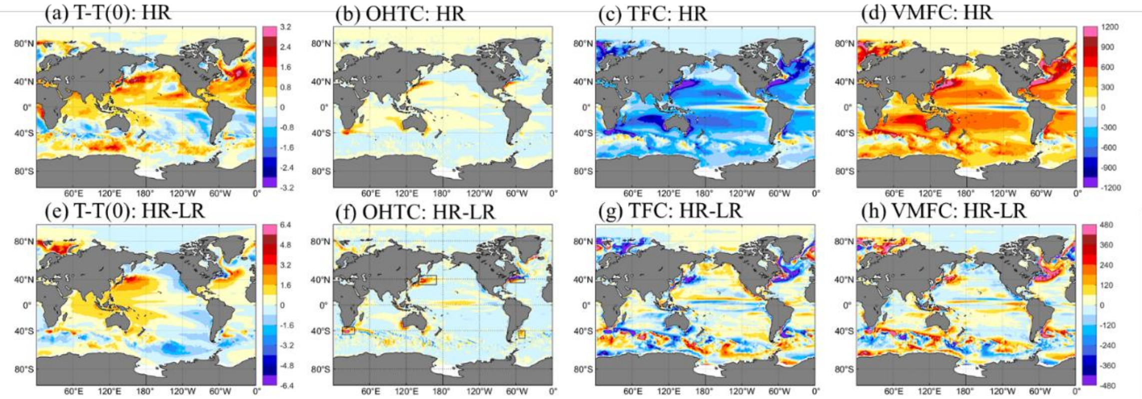

Figure A3 Similar to Figure 2.4, but for 20-years SPIN-HR and SPIN-LR.

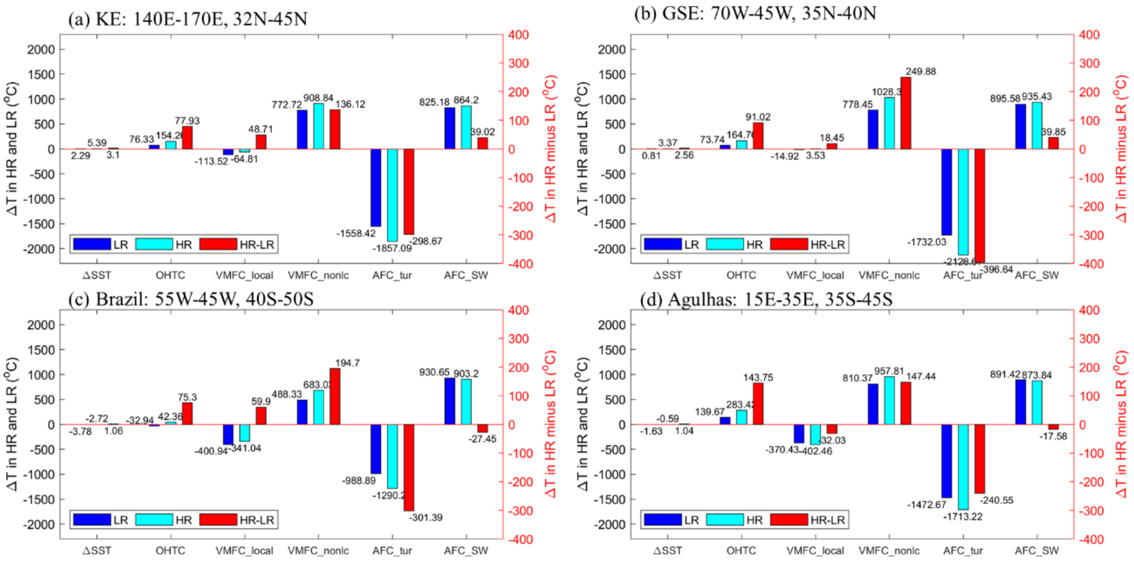

Figure A4 20-year mean of heat balance in four eddy-active regions labelled by black boxes in Figure 2.4f.

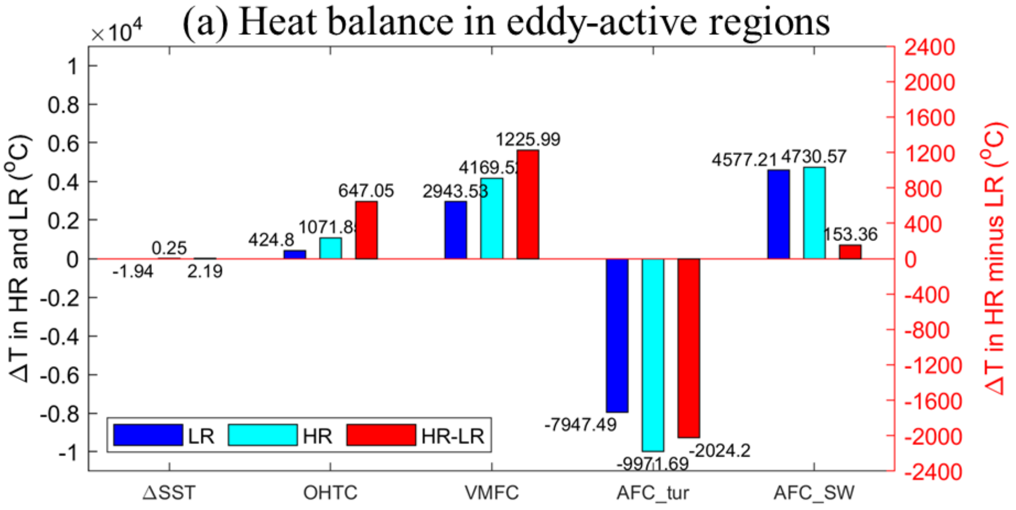

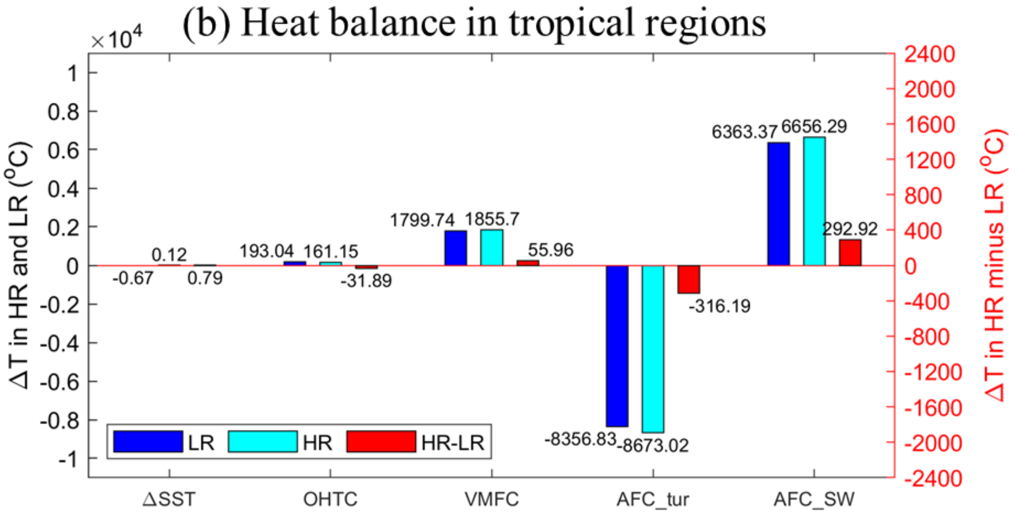

Figure A5 106-year mean of heat balance (CNTL-HR and CNTL-LR-HRIC) in eddy-active regions **(a)** and the tropics **(b)**.

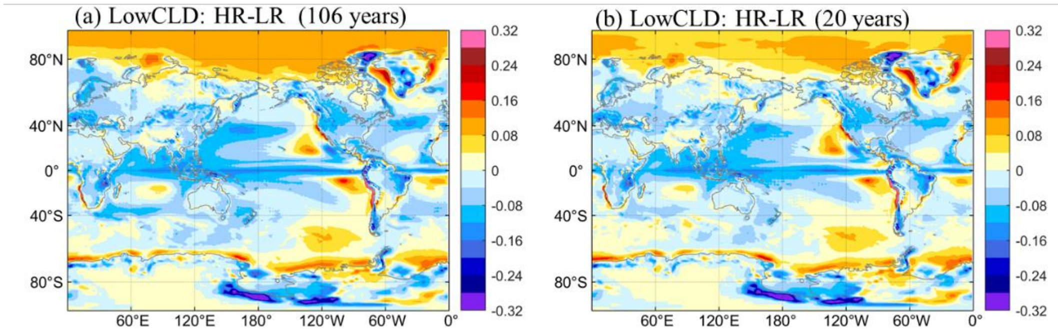

Figure A6 Low cloud difference **(a)** between CNTL-HR and CNTL-LR-HRIC; **(b)** between SPIN-HR and SPIN-LR.

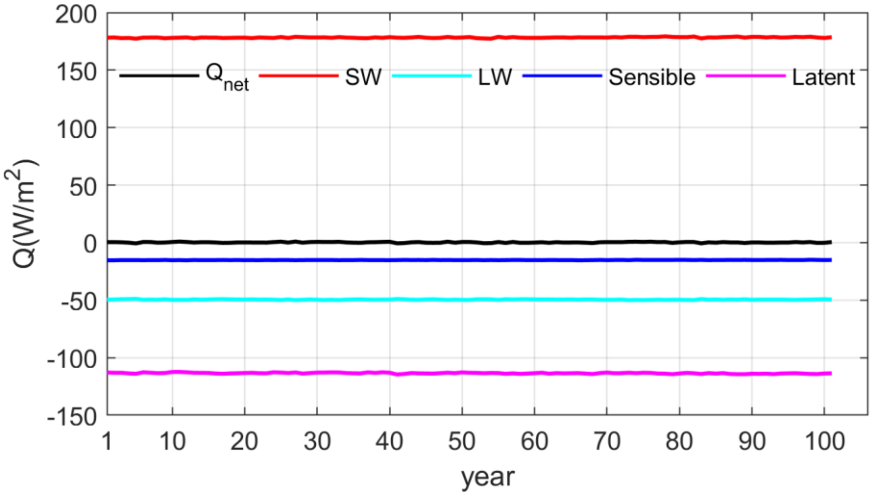

Figure A7 Decomposition of net surface heat flux in HR CNTL-CESM simulation, black for Q_{net} , red for shortwave heat flux, cyan for longwave heat flux, blue for sensible heat flux and magenta for latent heat flux.

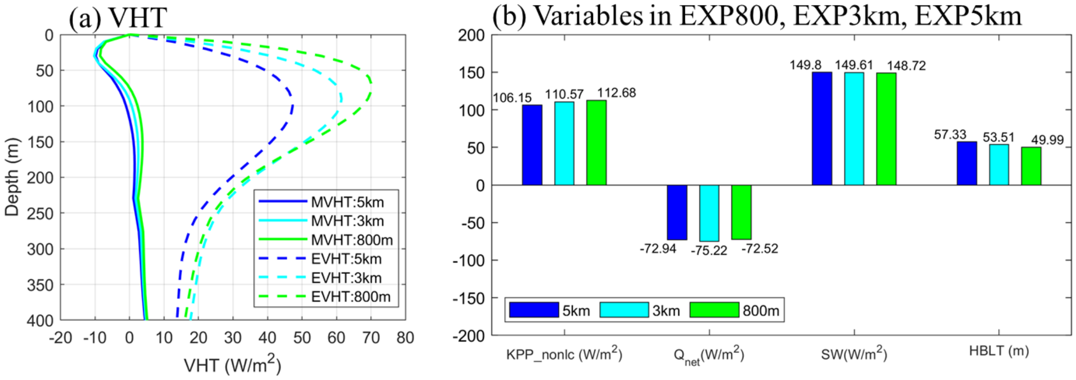

Figure A8 20-year averaged **(a)** MVHT (solid) and EVHT (dashed) in EXP5km (blue), EXP3km (cyan), and EXP800m (yellow); **(b)** nonlocal KPP flux, Q_{net}, SW at surface, and HBLT (blue), EXP3km (cyan), and EXP800m (yellow). Results are obtained in KE (145^{o}E-170^{o}E, 34^{o}N-39^{o}N) and GSE (65^{o}W-50^{o}W, 33^{o}N-41^{o}N).

APPENDIX B

SUPPLEMENTARY FIGURES FOR CHAPTER 3

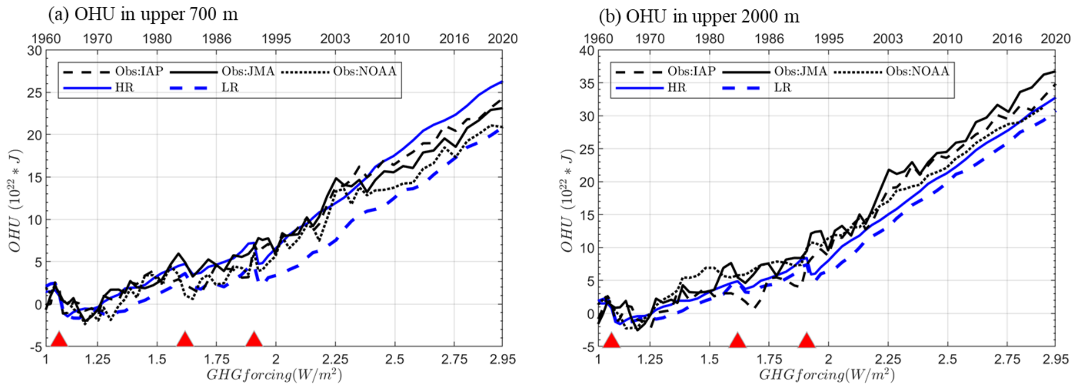

Figure B9 Similar to Figure 3.1 but with internal variabilities in PI-CNTL excluded by EMD method.

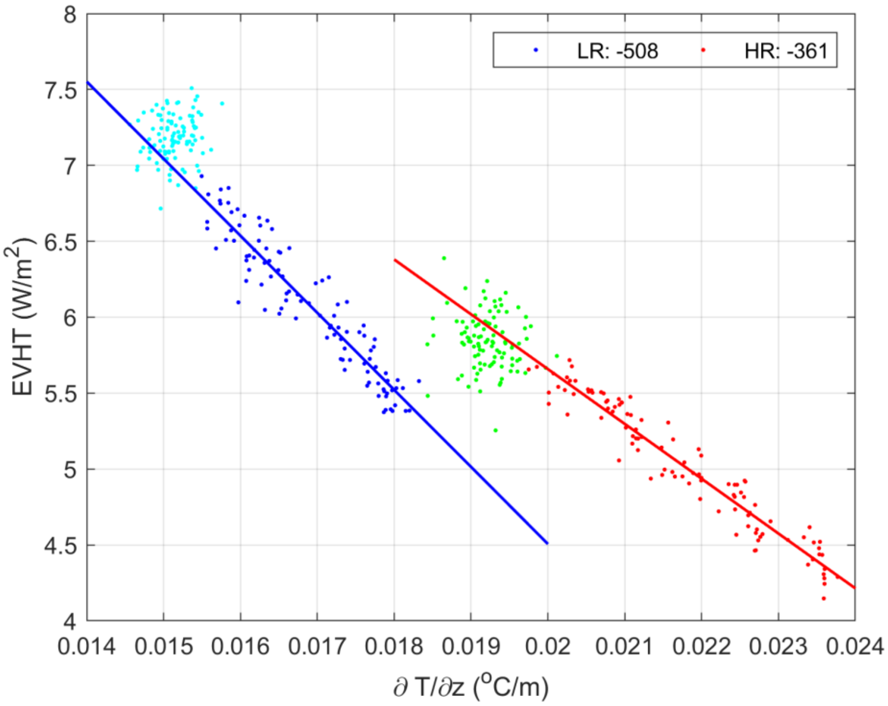

Figure B10 Similar to Figure 3.5 but with eddy defined as GM90 in LR and deviation from seasonal mean in HR.

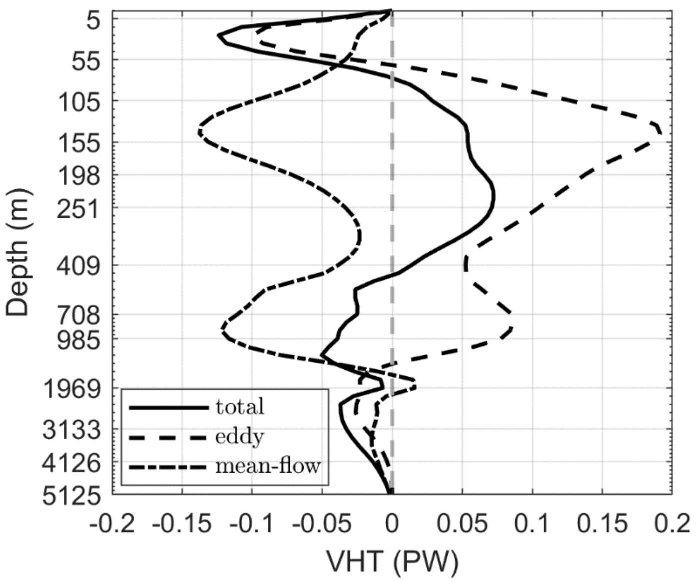

Figure B11 Difference of changes in VHT (solid), EVHT (dashed), and MVHT (dot-dashed) between HR and LR with mean defined as long-term mean.

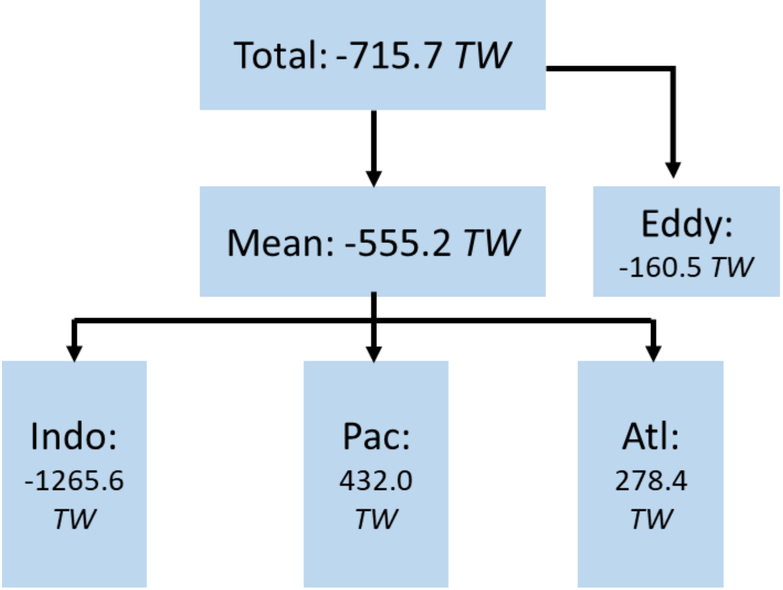

Figure B12 MHT across 35°S in PI-CNTL averaged over year 400-500.

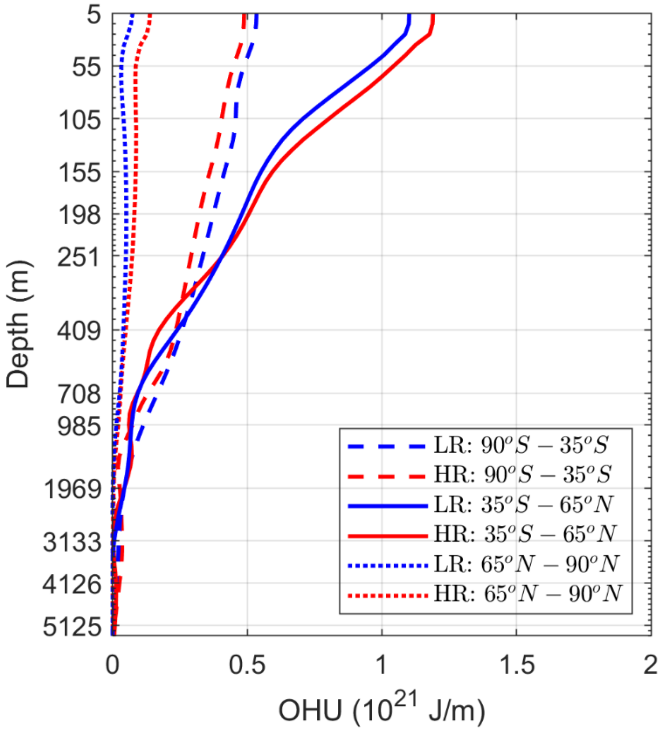

Figure B13 OHU in HR (red) and LR (blue) in SA (dashed), 35°S-65°N (solid), and the Arctic (dotted) averaged over 2000-2100.

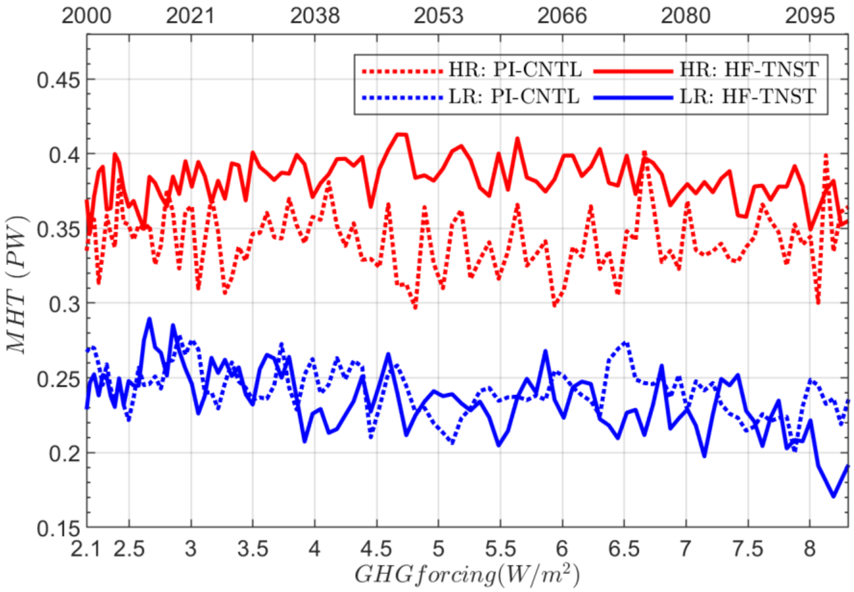

Figure B14 MHT across 65°N in HR PI-CNTL (red dotted), HF-TNST (red solid), LR PI-CNTL (blue dotted), and HF-TNST (blue solid).

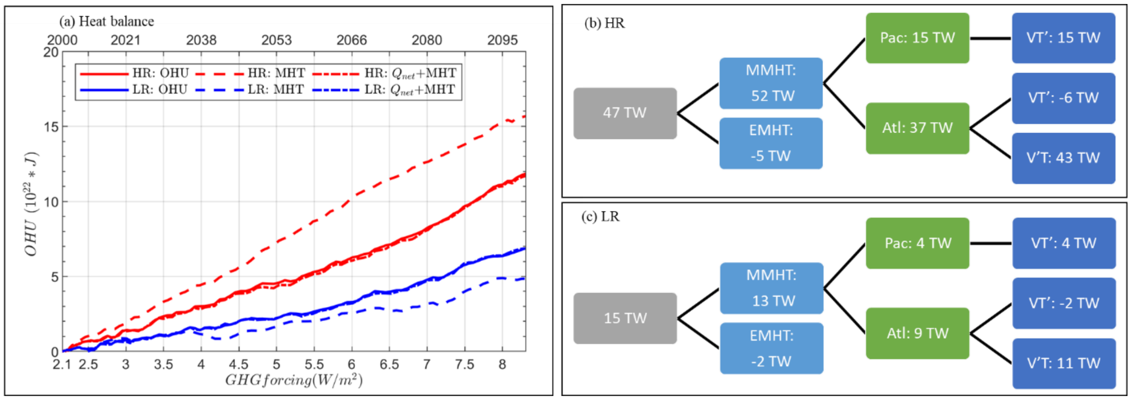

Figure B15 **(a)** Similar to Figure 3.11 but for 70^{o}N-90^{o}N; **(b)(c)** similar to Figure 3.12 but for 70^{o}N.

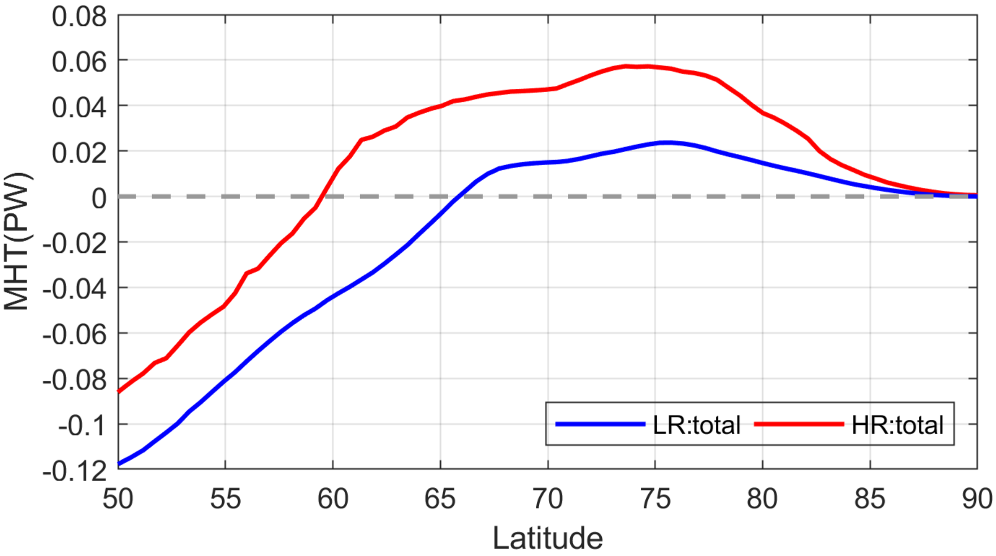

Figure B16 Time mean MHT changes defined as the difference of HF-TNST and PI-CNTL averaged over 2000-2100.

REFERENCES

Alexander, M. A., Bladé, I., Newman, M., Lanzante, J. R., Lau, N. C., & Scott, J. D. (2002). The atmospheric bridge: The influence of ENSO teleconnections on air–sea interaction over the global oceans. *Journal of Climate*, *15*(16), 2205-2231.

Andrews T, Gregory JM, Webb MJ. (2015). The dependence of radiative forcing and feedback on evolving patterns of surface temperature change in climate models. *Journal of Climate.* **28**, 1630–1648.

Andrews, T., & Webb, M. J. (2018). The dependence of global cloud and lapse rate feedbacks on the spatial structure of tropical Pacific warming. *Journal of Climate*, *31*(2), 641-654.

Andrews, T., Gregory, J. M., Webb, M. J., & Taylor, K. E. (2012). Forcing, feedbacks and climate sensitivity in CMIP5 coupled atmosphere-ocean climate models. *Geophysical Research Letters*, *39*(9).

Armour KC, Bitz CM, Roe GH. (2013). Time-varying climate sensitivity from regional feedbacks. *Journal of Climate.* **26**, 4518–4534.

Armour, K. C., Marshall, J., Scott, J. R., Donohoe, A., & Newsom, E. R. (2016). Southern Ocean warming delayed by circumpolar upwelling and equatorward transport. *Nature Geoscience*, *9*(7), 549-554.

Ashfaq, M., Skinner, C. B., & Diffenbaugh, N. S. (2011). Influence of SST biases on future climate change projections. *Climate Dynamics*, 36(7-8), 1303-1319.

Bane Jr, J. M., & Osgood, K. E. (1989). Wintertime air-sea interaction processes across the Gulf Stream. *Journal of Geophysical Research: Oceans*, *94*(C8), 10755-10772.

Banks, H. T., & Gregory, J. M. (2006). Mechanisms of ocean heat uptake in a coupled climate model and the implications for tracer based predictions of ocean heat uptake. *Geophysical Research Letters*, *33*(7).

Banzon, V., Smith, T. M., Chin, T. M., Liu, C., & Hankins, W. (2016). A long-term record of blended satellite and in situ sea-surface temperature for climate monitoring, modeling and environmental studies. *Earth System Science Data*, *8*(1), 165-176.

Barnett, T. P., Pierce, D. W., AchutaRao, K. M., Gleckler, P. J., Santer, B. D., Gregory, J. M., & Washington, W. M. (2005). Penetration of human-induced warming into the world's oceans. *Science*, *309*(5732), 284-287.

Bayr, T., Domeisen, D. I., & Wengel, C. (2019). The effect of the equatorial Pacific cold SST bias on simulated ENSO teleconnections to the North Pacific and California. *Climate Dynamics*, *53*(7), 3771-3789.

Befus, K. M., Barnard, P. L., Hoover, D. J., Finzi Hart, J. A., & Voss, C. I. (2020). Increasing threat of coastal groundwater hazards from sea-level rise in California. *Nature Climate Change*, *10*(10), 946-952.

Bishop, S. P., Small, R. J., & Bryan, F. O. (2020). The Global Sink of Available Potential Energy by Mesoscale Air-Sea Interaction. *Journal of Advances in Modeling Earth Systems*, *12*(10), e2020MS002118.

Bleuel, J., Pennino, M. G., & Longo, G. O. (2021). Coral distribution and bleaching vulnerability areas in Southwestern Atlantic under ocean warming. *Scientific Reports*, *11*(1), 1-12.

Bony, S., Bellon, G., Klocke, D., Sherwood, S., Fermepin, S., & Denvil, S. (2013). Robust direct effect of carbon dioxide on tropical circulation and regional precipitation. *Nature Geoscience*, *6*(6), 447-451.

Boucher, O., D. Randall, P. Artaxo, C. Bretherton, G. Feingold, P. Forster, V.-M. Kerminen, Y. Kondo, H. Liao, U. Lohmann, P. Rasch, S.K. Satheesh, S. Sherwood, B. Stevens and X.Y. Zhang, 2013: Clouds and Aerosols. In: Climate Change 2013: The Physical Science Basis. Contribution of Working Group I to the Fifth Assessment Report of the Intergovernmental Panel on Climate Change [Stocker, T.F., D. Qin, G.-K. Plattner, M. Tignor, S.K. Allen, J. Boschung, A. Nauels, Y. Xia, V. Bex and P.M. Midgley (eds.)]. Cambridge University Press, Cambridge, United Kingdom and New York, NY, USA

Breitburg, D., Levin, L. A., Oschlies, A., Grégoire, M., Chavez, F. P., Conley, D. J., ... & Zhang, J. (2018). Declining oxygen in the global ocean and coastal waters. *Science*, *359*(6371), eaam7240.

Brierley, C. M., Collins, M., & Thorpe, A. J. (2010). The impact of perturbations to ocean-model parameters on climate and climate change in a coupled model. *Climate Dynamics*, *34*(2), 325-343.

Bruun, P. (1962). Sea-level rise as a cause of shore erosion. *Journal of the Waterways and Harbors division*, *88*(1), 117-130.

Bryan, F. O., Gent, P. R., & Tomas, R. (2014). Can Southern Ocean eddy effects be parameterized in climate models?. *Journal of Climate*, *27*(1), 411-425.

Bryan, F. O., Hecht, M. W., & Smith, R. D. (2007). Resolution convergence and sensitivity studies with North Atlantic circulation models. Part I: The western boundary current system. *Ocean Modelling*, *16*(3-4), 141-159.

Buchanan, M. K., Kulp, S., Cushing, L., Morello-Frosch, R., Nedwick, T., & Strauss, B. (2020). Sea level rise and coastal flooding threaten affordable housing. *Environmental Research Letters*, *15*(12), 124020.

Burgard, C., & Notz, D. (2017). Drivers of Arctic Ocean warming in CMIP5 models. *Geophysical Research Letters*, *44*(9), 4263-4271.

Burls, N. J., Muir, L., Vincent, E. M., & Fedorov, A. (2017). Extra-tropical origin of equatorial Pacific cold bias in climate models with links to cloud albedo. *Climate Dynamics*, *49*(5), 2093-2113.

Camargo, S. J. (2013). Global and regional aspects of tropical cyclone activity in the CMIP5 models. *Journal of Climate*, *26*(24), 9880-9902.

Cantin, N. E., Cohen, A. L., Karnauskas, K. B., Tarrant, A. M., & McCorkle, D. C. (2010). Ocean warming slows coral growth in the central Red Sea. *Science*, *329*(5989), 322-325.

Chang, P., Saravanan, R., Ji, L., & Hegerl, G. C. (2000). The effect of local sea surface temperatures on atmospheric circulation over the tropical Atlantic sector. *Journal of Climate*, *13*(13), 2195-2216.

Chang, P., Yamagata, T., Schopf, P., Behera, S. K., Carton, J., Kessler, W. S., ... & Xie, S. P. (2006). Climate fluctuations of tropical coupled systems—the role of ocean dynamics. *Journal of Climate*, *19*(20), 5122-5174.

Chang, P., Zhang, S., Danabasoglu, G., Yeager, S. G., Fu, H., Wang, H., ... & Wu, L. (2020). An unprecedented set of high-resolution earth system simulations for understanding multiscale interactions in climate variability and change. *Journal of Advances in Modeling Earth Systems*, *12*(12), e2020MS002298.

Chassignet, E. P., & Marshall, D. P. (2008). Gulf Stream separation in numerical ocean models. *Geophysical Monograph Series*, *177*.

Chelton, D. B., Esbensen, S. K., Schlax, M. G., Thum, N., Freilich, M. H., Wentz, F. J., ... & Schopf, P. S. (2001). Observations of coupling between surface wind stress and sea surface temperature in the eastern tropical Pacific. *Journal of Climate*, *14*(7), 1479-1498.

Cornillon, P. (1986). The effect of the New England Seamounts on Gulf Stream meandering as observed from satellite IR imagery. *J. Phys. Oceanogr, 16*(2), 386-389.

Cox, P. M., Betts, R. A., Jones, C. D., Spall, S. A., & Totterdell, I. J. (2000). Acceleration of global warming due to carbon-cycle feedbacks in a coupled climate model. *Nature*, *408*(6809), 184-187.

Danabasoglu, G., Large, W. G., & Briegleb, B. P. (2010). Climate impacts of parameterized Nordic Sea overflows. *Journal of Geophysical Research: Oceans,* 115(C11).

Deser, C., & Phillips, A. S. (2009). Atmospheric circulation trends, 1950–2000: The relative roles of sea surface temperature forcing and direct atmospheric radiative forcing. *Journal of Climate*, *22*(2), 396-413.

Di Lorenzo, E., & Mantua, N. (2016). Multi-year persistence of the 2014/15 North Pacific marine heatwave. *Nature Climate Change*, *6*(11), 1042-1047.

Docquier, D., Grist, J. P., Roberts, M. J., Roberts, C. D., Semmler, T., Ponsoni, L., ... & Fichefet, T. (2019). Impact of model resolution on Arctic sea ice and North Atlantic Ocean heat transport. *Climate Dynamics*, *53*(7), 4989-5017.

Docquier, D., Koenigk, T., Fuentes-Franco, R., Karami, M. P., & Ruprich-Robert, Y. (2021). Impact of ocean heat transport on the Arctic sea-ice decline: a model study with EC-Earth3. *Climate Dynamics*, *56*(5), 1407-1432.

Domingues, C. M., Church, J. A., White, N. J., Gleckler, P. J., Wijffels, S. E., Barker, P. M., & Dunn, J. R. (2008). Improved estimates of upper-ocean warming and multi-decadal sea-level rise. *Nature, 453*(7198), 1090-1093.

Dufresne, J. L., & Bony, S. (2008). An assessment of the primary sources of spread of global warming estimates from coupled atmosphere–ocean models. *Journal of Climate*, *21*(19), 5135-5144.

Dutheil, C., Lengaigne, M., Bador, M., Vialard, J., Lefèvre, J., Jourdain, N. C., ... & Menkès, C. (2020). impact of projected sea surface temperature biases on tropical cyclones projections in the South Pacific. *Scientific Reports,* 10(1), 1-12.

Eaton, B. (2011). User's guide to the Community Atmosphere Model CAM-5.1. *NCAR. URL http://www. cesm. ucar. edu/models/cesm1. 0/cam*.

Elsner, J. B., Kossin, J. P., & Jagger, T. H. (2008). The increasing intensity of the strongest tropical cyclones. *Nature, 455*(7209), 92-95.

Emanuel, K. (2005). Increasing destructiveness of tropical cyclones over the past 30 years. *Nature, 436*(7051), 686-688.

Emanuel, K. (2017). Assessing the present and future probability of Hurricane Harvey's rainfall. *Proceedings of the National Academy of Sciences*, *114*(48), 12681-12684.

Forget, G., & Ferreira, D. (2019). Global ocean heat transport dominated by heat export from the tropical Pacific. *Nature Geoscience, 12*(5), 351-354.

Francis, J. A., & Vavrus, S. J. (2012). Evidence linking Arctic amplification to extreme weather in mid-latitudes. *Geophysical Research Letters*, *39*(6).

Fu, W., Randerson, J. T., & Moore, J. K. (2016). Climate change impacts on net primary production (NPP) and export production (EP) regulated by increasing stratification and phytoplankton community structure in the CMIP5 models. *Biogeosciences, 13*(18), 5151-5170.

Ganachaud, A., & Wunsch, C. (2000). Improved estimates of global ocean circulation, heat transport and mixing from hydrographic data. *Nature*, *408*(6811), 453-457.

Garfinkel, C. I., White, I., Gerber, E. P., & Jucker, M. (2020). The impact of SST biases in the tropical east Pacific and Agulhas current region on atmospheric stationary waves in the Southern Hemisphere. *Journal of Climate,* 33(21), 9351-9374.

Gent, P. R., Yeager, S. G., Neale, R. B., Levis, S., & Bailey, D. A. (2010). Improvements in a half degree atmosphere/land version of the CCSM. *Climate Dynamics*, 34(6), 819-833.

Geoffroy O, Saint-Martin D, Bellon G, Voldoire A, Olivié DJL, Tytéca S. 2013Transient climate response in a two-layer energy-balance model. II. Representation of the efficacy of deep-ocean heat uptake and validation for CMIP5 AOGCMs. *Journal of Climate.* **26**, 1859–1876.

Gleckler, P. J., Santer, B. D., Domingues, C. M., Pierce, D. W., Barnett, T. P., Church, J. A., ... & Caldwell, P. M. (2012). Human-induced global ocean warming on multidecadal timescales. *Nature Climate Change, 2*(7), 524-529.

Good, P., Lowe, J. A., & Rowell, D. P. (2009). Understanding uncertainty in future projections for the tropical Atlantic: relationships with the unforced climate. *Climate Dynamics*, 32(2), 205-218.

Gregory, J., Ingram, W. J., Palmer, M. A., Jones, G. S., Stott, P. A., Thorpe, R. B., ... & Williams, K. D. (2004). A new method for diagnosing radiative forcing and climate sensitivity. *Geophysical Research Letters*, *31*(3).

Griffies, S. M. (1998). The gent–mcwilliams skew flux. *Journal of Physical Oceanography*, *28*(5), 831-841.

Griffies, S. M., Winton, M., Anderson, W. G., Benson, R., Delworth, T. L., Dufour, C. O., ... & Zhang, R. (2015). Impacts on ocean heat from transient mesoscale eddies in a hierarchy of climate models. *Journal of Climate*, 28(3), 952-977.

Gutjahr, O., Putrasahan, D., Lohmann, K., Jungclaus, J. H., Storch, J. S. V., Brüggemann, N., ... & Stössel, A. (2019). Max Planck Institute Earth System Model (MPI-ESM1. 2) for the High-Resolution Model Intercomparison Project (HighResMIP). *Geoscientific Model Development*, 12(7), 3241-3281.

Haarsma, R. J., Roberts, M. J., Vidale, P. L., Senior, C. A., Bellucci, A., Bao, Q., ... & Storch, J. S. V. (2016). High resolution model intercomparison project (HighResMIP v1. 0) for CMIP6. *Geoscientific Model Development*, 9(11), 4185-4208.

Hasumi, H. (2014). A review on ocean resolution dependence of climate biases in AOGCMs. CLIVAR Exchanges, 65, 7-9.

He, J., & Soden, B. J. (2016). The impact of SST biases on projections of anthropogenic climate change: A greater role for atmosphere‐only models?. *Geophysical Research Letters*, 43(14), 7745-7750.

Heberger, M., Cooley, H., Herrera, P., Gleick, P. H., & Moore, E. (2011). Potential impacts of increased coastal flooding in California due to sea-level rise. *Climatic Change*, *109*(1), 229-249.

Hieronymus, M., & Nycander, J. (2013). The budgets of heat and salinity in NEMO. *Ocean Modelling*, *67*, 28-38.

Houghton, E. (1996). *Climate change 1995: The science of climate change: contribution of working group I to the second assessment report of the Intergovernmental Panel on Climate Change* (Vol. 2). Cambridge University Press.

Houghton, J. T., Ding, Y. D. J. G., Griggs, D. J., Noguer, M., van der Linden, P. J., Dai, X., ... & Johnson, C. A. (Eds.). (2001). *Climate change 2001: the scientific basis: contribution of Working Group I to the third assessment report of the Intergovernmental Panel on Climate Change*. Cambridge university press.

Hsu, W. C., Patricola, C. M., & Chang, P. (2019). The impact of climate model sea surface temperature biases on tropical cyclone simulations. *Climate Dynamics*, 53(1), 173-192.

Huang, B., Liu, C., Banzon, V., Freeman, E., Graham, G., Hankins, B., ... & Zhang, H. M. (2021). Improvements of the daily optimum interpolation sea surface temperature (DOISST) version 2.1. *Journal of Climate*, *34*(8), 2923-2939.

Huang, N. E., Shen, Z., Long, S. R., Wu, M. C., Shih, H. H., Zheng, Q., ... & Liu, H. H. (1998). The empirical mode decomposition and the Hilbert spectrum for nonlinear and non-stationary time series analysis. *Proceedings of the Royal Society of London. Series A: mathematical, physical and engineering sciences*, *454*(1971), 903-995.

Hyder, P., Edwards, J. M., Allan, R. P., Hewitt, H. T., Bracegirdle, T. J., Gregory, J. M., ... & Belcher, S. E. (2018). Critical Southern Ocean climate model biases traced to atmospheric model cloud errors. *Nature Communications*, 9(1), 1-17.

Ishii, M., Fukuda, Y., Hirahara, S., Yasui, S., Suzuki, T., & Sato, K. (2017). Accuracy of global upper ocean heat content estimation expected from present observational data sets. *Sola*, *13*, 163-167.

Jia, Y., Furue, R., & McCreary Jr, J. P. (2015). Impacts of regional mixing on the temperature structure of the equatorial Pacific Ocean. Part 2: Depth-dependent vertical diffusion. *Ocean Modelling*, *91*, 112-127.

Jia, Y., Richards, K. J., & Annamalai, H. (2021). The impact of vertical resolution in reducing biases in sea surface temperature in a tropical Pacific Ocean model. *Ocean Modelling*, *157*, 101722.

Jing, Z., Wang, S., Wu, L., Chang, P., Zhang, Q., Sun, B., ... & Wan, X. (2020). Maintenance of mid-latitude oceanic fronts by mesoscale eddies. *Science Advances*, *6*(31), eaba7880.

Johnson, N. C., Krishnamurthy, L., Wittenberg, A. T., Xiang, B., Vecchi, G. A., Kapnick, S. B., & Pascale, S. (2020). The impact of sea surface temperature biases on North American precipitation in a high-resolution climate model. *Journal of Climate*, 33(6), 2427-2447.

Joseph, P. V., & Pillai, P. V. (1984). Air-sea interaction on a seasonal scale over north Indian Ocean-Part I: Inter-annual variations of sea surface temperature and Indian summer monsoon rainfall. *Mausam*, *35*(3), 323-330.

Keeling, R. F., Körtzinger, A., & Gruber, N. (2010). Ocean deoxygenation in a warming world. *Annual Review of Marine Science*, *2*, 199-229.

Klotzbach, P. J., Bowen, S. G., Pielke, R., & Bell, M. (2018). Continental US hurricane landfall frequency and associated damage: Observations and future risks. *Bulletin of the American Meteorological Society*, *99*(7), 1359-1376.

Knutson, T., Camargo, S. J., Chan, J. C., Emanuel, K., Ho, C. H., Kossin, J., ... & Wu, L. (2020). Tropical cyclones and climate change assessment: Part II: Projected response to anthropogenic warming. *Bulletin of the American Meteorological Society, 101*(3), E303-E322.

Krishnamurthy, L., & Krishnamurthy, V. J. C. D. (2014). Influence of PDO on South Asian summer monsoon and monsoon–ENSO relation. *Climate Dynamics*, *42*(9-10), 2397-2410.

Krishnamurti, T. N., Oosterhof, D. K., & Mehta, A. V. (1988). Air–sea interaction on the time scale of 30 to 50 days. *Journal of the Atmospheric Sciences*, *45*(8), 1304-1322.

Kurian, J., Li, P., Chang, P., Patricola, C. M., & Small, J. (2021). Impact of the Benguela coastal low-level jet on the southeast tropical Atlantic SST bias in a regional ocean model. *Climate Dynamics*, 1-28.

Large, W. G., McWilliams, J. C., & Doney, S. C. (1994). Oceanic vertical mixing: A review and a model with a nonlocal boundary layer parameterization. *Reviews of Geophysics*, *32*(4), 363-403.

Last, P. R., White, W. T., Gledhill, D. C., Hobday, A. J., Brown, R., Edgar, G. J., & Pecl, G. (2011). Long-term shifts in abundance and distribution of a temperate fish fauna: a response to climate change and fishing practices. *Global Ecology and Biogeography*, *20*(1), 58-72.

Leatherman, S. P., Zhang, K., & Douglas, B. C. (2000). Sea level rise shown to drive coastal erosion. *Eos, Transactions American Geophysical Union*, *81*(6), 55-57.

Lee, R. W., Woollings, T. J., Hoskins, B. J., Williams, K. D., O'Reilly, C. H., & Masato, G. (2018). Impact of Gulf Stream SST biases on the global atmospheric circulation. *Climate Dynamics,* 51(9), 3369-3387.

Legeckis, R. (1977). Long waves in the eastern equatorial Pacific Ocean: A view from a geostationary satellite. *Science, 197*(4309), 1179-1181.

Levitus, S., Antonov, J. I., Boyer, T. P., & Stephens, C. (2000). Warming of the world ocean. *Science*, *287*(5461), 2225-2229.

Levitus, S., Antonov, J. I., Boyer, T. P., Baranova, O. K., Garcia, H. E., Locarnini, R. A., ... & Zweng, M. M. (2012). World ocean heat content and thermosteric sea level change (0–2000 m), 1955–2010. *Geophysical Research Letters*, *39*(10).

Li, C., von Storch, J. S., & Marotzke, J. (2013). Deep-ocean heat uptake and equilibrium climate response. *Climate Dynamics*, *40*(5-6), 1071-1086.

Li, G., & Xie, S. P. (2012). Origins of tropical-wide SST biases in CMIP multi-model ensembles. *Geophysical Research Letters*, *39*(22).

Li, Q., Luo, Y., & Liu, F. (2021). Asymmetric responses of the meridional ocean heat transport to climate warming and cooling in CESM. *Climate Dynamics*, 1-19.

Liang, X., Spall, M., & Wunsch, C. (2017). Global ocean vertical velocity from a dynamically consistent ocean state estimate. *Journal of Geophysical Research: Oceans*, *122*(10), 8208-8224.

Lindzen, R. S., & Nigam, S. (1987). On the role of sea surface temperature gradients in forcing low-level winds and convergence in the tropics. *Journal of Atmospheric Sciences*, *44*(17), 2418-2436.

Link, J. S., Nye, J. A., & Hare, J. A. (2011). Guidelines for incorporating fish distribution shifts into a fisheries management context. *Fish and Fisheries*, *12*(4), 461-469.

Liu, W., Lu, J., Xie, S. P., & Fedorov, A. (2018). Southern Ocean heat uptake, redistribution, and storage in a warming climate: The role of meridional overturning circulation. *Journal of Climate*, *31*(12), 4727-4743.

Loeb, N. G., Lyman, J. M., Johnson, G. C., Allan, R. P., Doelling, D. R., Wong, T., ... & Stephens, G. L. (2012). Observed changes in top-of-the-atmosphere radiation and upper-ocean heating consistent within uncertainty. *Nature Geoscience*, *5*(2), 110-113.

Lyman, J. M., Good, S. A., Gouretski, V. V., Ishii, M., Johnson, G. C., Palmer, M. D., ... & Willis, J. K. (2010). Robust warming of the global upper ocean. *Nature*, *465*(7296), 334-337.

Mahlstein, I., & Knutti, R. (2011). Ocean heat transport as a cause for model uncertainty in projected Arctic warming. *Journal of Climate*, *24*(5), 1451-1460.

Manabe, S., & Stouffer, R. J. (1980). Sensitivity of a global climate model to an increase of CO2 concentration in the atmosphere. *Journal of Geophysical Research: Oceans*, *85*(C10), 5529-5554.

Manabe, S., & Wetherald, R. T. (1975). The effects of doubling the CO 2 concentration on the climate of a general circulation model. *Journal of Atmospheric Sciences*, *32*(1), 3-15.

Manganello, J. V., & Huang, B. (2009). The influence of systematic errors in the Southeast Pacific on ENSO variability and prediction in a coupled GCM. *Climate Dynamics*, *32*(7), 1015-1034.

McCabe, G. J., Palecki, M. A., & Betancourt, J. L. (2004). Pacific and Atlantic Ocean influences on multidecadal drought frequency in the United States. *Proceedings of the National Academy of Sciences*, *101*(12), 4136-4141.

McGregor, S., Stuecker, M. F., Kajtar, J. B., England, M. H., & Collins, M. (2018). Model tropical atlantic biases underpin diminished pacific decadal variability. *Nature Climate Change*, 8(6), 493-498.

Meehl, G. A., Collins, W. D., Boville, B. A., Kiehl, J. T., Wigley, T. M. L., & Arblaster, J. M. (2000). Response of the NCAR Climate System Model to increased CO2 and the role of physical processes. *Journal of Climate*, *13*(11), 1879-1898.

Meehl, G. A., Yang, D., Arblaster, J. M., Bates, S. C., Rosenbloom, N., Neale, R., ... & Danabasoglu, G. (2019). Effects of model resolution, physics, and coupling on Southern Hemisphere storm tracks in CESM1. 3. *Geophysical Research Letters*, *46*(21), 12408-12416.

Minobe, S., Kuwano-Yoshida, A., Komori, N., Xie, S. P., & Small, R. J. (2008). Influence of the Gulf Stream on the troposphere. *Nature*, *452*(7184), 206-209.

Mitchell, J. F. B., Davis, R. A., Ingram, W. A., & Senior, C. A. (1995a). On surface temperature, greenhouse gases, and aerosols: Models and observations. *Journal of Climate*, *8*(10), 2364-2386.

Mitchell, J. F., Johns, T. C., Gregory, J. M., & Tett, S. F. B. (1995b). Climate response to increasing levels of greenhouse gases and sulphate aerosols. *Nature*, *376*(6540), 501-504.

Morrison, A. K., Saenko, O. A., Hogg, A. M., & Spence, P. (2013). The role of vertical eddy flux in Southern Ocean heat uptake. *Geophysical Research Letters*, *40*(20), 5445-5450.

Moum, J. N., Perlin, A., Nash, J. D., & McPhaden, M. J. (2013). Seasonal sea surface cooling in the equatorial Pacific cold tongue controlled by ocean mixing. *Nature*, *500*(7460), 64-67.

Myhre, G., D. Shindell, F.-M. Bréon, W. Collins, J. Fuglestvedt, J. Huang, D. Koch, J.-F. Lamarque, D. Lee, B. Mendoza, T. Nakajima, A. Robock, G. Stephens, T. Takemura and H. Zhang, 2013: Anthropogenic and Natural Radiative Forcing. In: Climate Change 2013: The Physical Science Basis. Contribution of Working Group I to the Fifth Assessment Report of the Intergovernmental Panel on Climate Change [Stocker, T.F., D. Qin, G.-K. Plattner, M. Tignor, S.K. Allen, J. Boschung, A. Nauels, Y. Xia, V. Bex and P.M. Midgley (eds.)]. Cambridge University Press, Cambridge, United Kingdom and New York, NY, USA

O’Neill, L. W., Chelton, D. B., & Esbensen, S. K. (2012). Covariability of surface wind and stress responses to sea surface temperature fronts. *Journal of Climate*, *25*(17), 5916-5942.

O'Neill, B. C., Tebaldi, C., Vuuren, D. P. V., Eyring, V., Friedlingstein, P., Hurtt, G., ... & Sanderson, B. M. (2016). The scenario model intercomparison project (ScenarioMIP) for CMIP6. *Geoscientific Model Development*, 9(9), 3461-3482.

Pachauri, R. K., & Reisinger, A. (2008). Climate change 2007. Synthesis report. Contribution of Working Groups I, II and III to the fourth assessment report.

Pachauri, R. K., Allen, M. R., Barros, V. R., Broome, J., Cramer, W., Christ, R., ... & van Ypserle, J. P. (2014). *Climate change 2014: synthesis report. Contribution of Working Groups I, II and III to the fifth assessment report of the Intergovernmental Panel on Climate Change* (p. 151). IPCC.

Pandey, L. K., & Dwivedi, S. (2021). Comparing the performance of turbulent kinetic energy and k-profile parameterization vertical parameterization schemes over the tropical Indian Ocean. *Marine Geodesy, 44*(1), 42-69.

Perry, A. L., Low, P. J., Ellis, J. R., & Reynolds, J. D. (2005). Climate change and distribution shifts in marine fishes. *Science, 308*(5730), 1912-1915.

Pinsky, M. L., Worm, B., Fogarty, M. J., Sarmiento, J. L., & Levin, S. A. (2013). Marine taxa track local climate velocities. *Science*, *341*(6151), 1239-1242.

Purkey, S. G., & Johnson, G. C. (2010). Warming of global abyssal and deep Southern Ocean waters between the 1990s and 2000s: Contributions to global heat and sea level rise budgets. *Journal of Climate*, *23*(23), 6336-6351.

Reimann, L., Vafeidis, A. T., Brown, S., Hinkel, J., & Tol, R. S. (2018). Mediterranean UNESCO World Heritage at risk from coastal flooding and erosion due to sea-level rise. *Nature Communications*, *9*(1), 1-11.

Reynolds, R. W., Smith, T. M., Liu, C., Chelton, D. B., Casey, K. S., & Schlax, M. G. (2007). Daily high-resolution-blended analyses for sea surface temperature. *Journal of Climate*, *20*(22), 5473-5496.

Richter, I., & Tokinaga, H. (2020). An overview of the performance of CMIP6 models in the tropical Atlantic: mean state, variability, and remote impacts. *Climate Dynamics*, 55(9), 2579-2601.

Roberts, M. J., Baker, A., Blockley, E. W., Calvert, D., Coward, A., Hewitt, H. T., ... & Vidale, P. L. (2019). Description of the resolution hierarchy of the global coupled HadGEM3-GC3. 1 model as used in CMIP6 HighResMIP experiments. *Geoscientific Model Development*, 12(12), 4999-5028.

Roemmich, D. (1992). Ocean warming and sea level rise along the southwest US coast. *Science*, *257*(5068), 373-375.

Roemmich, D., Alford, M. H., Claustre, H., Johnson, K., King, B., Moum, J., ... & Yasuda, I. (2019). On the future of Argo: A global, full-depth, multi-disciplinary array. *Frontiers in Marine Science*, *6*, 439.

Roemmich, D., Johnson, G. C., Riser, S., Davis, R., Gilson, J., Owens, W. B., ... & Ignaszewski, M. (2009). The Argo Program: Observing the global ocean with profiling floats. *Oceanography*, *22*(2), 34-43.

Ropelewski, C. F., & Halpert, M. S. (1987). Global and regional scale precipitation patterns associated with the El Niño/Southern Oscillation. *Monthly weather review*, *115*(8), 1606-1626.

Senior, C. A., & Mitchell, J. F. (2000). The time-dependence of climate sensitivity. *Geophysical Research Letters*, *27*(17), 2685-2688.

Smale, D. A. (2020). Impacts of ocean warming on kelp forest ecosystems. *New Phytologist*, *225*(4), 1447-1454.

Small, R. D., deSzoeke, S. P., Xie, S. P., O'neill, L., Seo, H., Song, Q., ... & Minobe, S. (2008). Air–sea interaction over ocean fronts and eddies. *Dynamics of Atmospheres and Oceans*, *45*(3-4), 274-319.

Small, R. J., Bacmeister, J., Bailey, D., Baker, A., Bishop, S., Bryan, F., ... & Vertenstein, M. (2014). A new synoptic scale resolving global climate simulation using the Community Earth System Model. *Journal of Advances in Modeling Earth Systems*, *6*(4), 1065-1094.

Small, R. J., Curchitser, E., Hedstrom, K., Kauffman, B., & Large, W. G. (2015). The Benguela upwelling system: Quantifying the sensitivity to resolution and coastal wind representation in a global climate model. *Journal of Climate*, *28*(23), 9409-9432.

Small, R. J., Msadek, R., Kwon, Y. O., Booth, J. F., & Zarzycki, C. (2019). Atmosphere surface storm track response to resolved ocean mesoscale in two sets of global climate model experiments. *Climate Dynamics*, 52(3), 2067-2089.

Small, R. J., Tomas, R. A., & Bryan, F. O. (2014). Storm track response to ocean fronts in a global high-resolution climate model. *Climate Dynamics*, *43*(3-4), 805-828.

Smith, R., & Gent, P. (2002). Reference manual for the parallel ocean program (POP). *Los Alamos unclassified report LA-UR-02-2484*.

Smith, R., Jones, P., Briegleb, B., Bryan, F., Danabasoglu, G., Dennis, J., ... & Yeager, S. (2010). The parallel ocean program (POP) reference manual ocean component of the community climate system model (CCSM) and community earth system model (CESM). *LAUR-01853*, *141*, 1-140.

Smith, S. R., Alory, G., Andersson, A., Asher, W., Baker, A., Berry, D. I., ... & Vinogradova-Shiffer, N. (2019). Ship-based contributions to global ocean, weather, and climate observing systems. *Frontiers in Marine Science*, *6*, 434.

Soden, B. J., & Held, I. M. (2006). An assessment of climate feedbacks in coupled ocean–atmosphere models. *Journal of Climate*, *19*(14), 3354-3360.

Song, X., & Zhang, G. J. (2009). Convection parameterization, tropical Pacific double ITCZ, and upper-ocean biases in the NCAR CCSM3. Part I: Climatology and atmospheric feedback. *Journal of Climate*, *22*(16), 4299-4315.

Su, Z., Torres, H., Klein, P., Thompson, A. F., Siegelman, L., Wang, J., ... & Hill, C. (2020). High-frequency submesoscale motions enhance the upward vertical heat transport in the global ocean. *Journal of Geophysical Research: Oceans*, *125*(9), e2020JC016544.

Su, Z., Wang, J., Klein, P., Thompson, A. F., & Menemenlis, D. (2018). Ocean submesoscales as a key component of the global heat budget. *Nature Communications*, *9*(1), 1-8.

Taylor, K. E., & Penner, J. E. (1994). Response of the climate system to atmospheric aerosols and greenhouse gases. *Nature*, *369*(6483), 734-737.

Trenberth, K. E., Fasullo, J. T., & Kiehl, J. (2009). Earth's global energy budget. *Bulletin of the American Meteorological Society*, *90*(3), 311-324.

Trenberth, K. E., Zhang, Y., Fasullo, J. T., & Cheng, L. (2019). Observation-based estimates of global and basin ocean meridional heat transport time series. *Journal of Climate*, *32*(14), 4567-4583.

van der Linden, E. C., Le Bars, D., Bintanja, R., & Hazeleger, W. (2019). Oceanic heat transport into the Arctic under high and low CO_2 forcing. *Climate Dynamics*, *53*(7), 4763-4780.

Van Roekel, L., Adcroft, A. J., Danabasoglu, G., Griffies, S. M., Kauffman, B., Large, W., ... & Schmidt, M. (2018). The KPP boundary layer scheme for the ocean: Revisiting its formulation and benchmarking one-dimensional simulations relative to LES. *Journal of Advances in Modeling Earth Systems*, 10(11), 2647-2685.

Vecchi, G. A., Delworth, T., Gudgel, R., Kapnick, S., Rosati, A., Wittenberg, A. T., ... & Zhang, S. (2014). On the seasonal forecasting of regional tropical cyclone activity. *Journal of Climate*, *27*(21), 7994-8016.

Vergés, A., Doropoulos, C., Malcolm, H. A., Skye, M., Garcia-Pizá, M., Marzinelli, E. M., ... & Steinberg, P. D. (2016). Long-term empirical evidence of ocean warming leading to tropicalization of fish communities, increased herbivory, and loss of kelp. *Proceedings of the National Academy of Sciences*, *113*(48), 13791-13796.

von Storch, J. S., Haak, H., Hertwig, E., & Fast, I. (2016). Vertical heat and salt fluxes due to resolved and parameterized meso-scale eddies. *Ocean Modelling*, *108*, 1-19.

Wang, B., Luo, X., & Liu, J. (2020). How robust is the Asian precipitation–ENSO relationship during the industrial warming period (1901–2017)?. *Journal of Climate*, *33*(7), 2779-2792.

Wang, L., Li, T., & Zhou, T. (2012). Intraseasonal SST variability and air–sea interaction over the Kuroshio Extension region during boreal summer. *Journal of Climate*, *25*(5), 1619-1634.

Winton M, Takahashi K, Held IM. 2010Importance of ocean heat uptake efficacy to transient climate change. *Journal of Climate*. **23**, 2333–2344.

Woelfle, M. D., Yu, S., Bretherton, C. S., & Pritchard, M. S. (2018). Sensitivity of coupled tropical Pacific model biases to convective parameterization in CESM1. *Journal of Advances in Modeling Earth Systems*, *10*(1), 126-144.

Wolfe, C. L., Cessi, P., McClean, J. L., & Maltrud, M. E. (2008). Vertical heat transport in eddying ocean models. *Geophysical Research Letters*, *35*(23).

Woodruff, J. D., Irish, J. L., & Camargo, S. J. (2013). Coastal flooding by tropical cyclones and sea-level rise. *Nature*, *504*(7478), 44-52.

Woodruff, S. D., Diaz, H. F., Worley, S. J., Reynolds, R. W., & Lubker, S. J. (2005). Early ship observational data and ICOADS. *Climatic Change*, *73*(1), 169-194.

Wu, P., Roberts, M., Martin, G., Chen, X., Zhou, T., & Vidale, P. L. (2019). The impact of horizontal atmospheric resolution in modelling air–sea heat fluxes. *Quarterly Journal of the Royal Meteorological Society*, *145*(724), 3271-3283.

Xiang, B., Wang, B., Ding, Q., Jin, F. F., Fu, X., & Kim, H. J. (2012). Reduction of the thermocline feedback associated with mean SST bias in ENSO simulation. *Climate Dynamics*, *39*(6), 1413-1430.

Xie, S. P., Xu, H., Kessler, W. S., & Nonaka, M. (2005). Air–sea interaction over the eastern Pacific warm pool: Gap winds, thermocline dome, and atmospheric convection. *Journal of Climate*, *18*(1), 5-20.

Xu, Z., Chang, P., Richter, I., & Tang, G. (2014). Diagnosing southeast tropical Atlantic SST and ocean circulation biases in the CMIP5 ensemble. *Climate Dynamics*, *43*(11), 3123-3145.

Yang, H., Li, Q., Wang, K., Sun, Y., & Sun, D. (2015). Decomposing the meridional heat transport in the climate system. *Climate Dynamics*, *44*(9), 2751-2768.

Ying, J., Huang, P., Lian, T., & Tan, H. (2019). Understanding the effect of an excessive cold tongue bias on projecting the tropical Pacific SST warming pattern in CMIP5 models. *Climate Dynamics*, *52*(3), 1805-1818.

Zhang, R., Delworth, T. L., Rosati, A., Anderson, W. G., Dixon, K. W., Lee, H. C., & Zeng, F. (2011). Sensitivity of the North Atlantic Ocean circulation to an abrupt change in the Nordic Sea overflow in a high resolution global coupled climate model. *Journal of Geophysical Research: Oceans*, 116(C12).

Zhu, Y., & Zhang, R. H. (2018). An argo-derived background diffusivity parameterization for improved ocean simulations in the tropical pacific. *Geophysical Research Letters*, *45*(3), 1509-1517.

Zhu, Y., Zhang, R. H., & Sun, J. (2020). North Pacific upper-ocean cold temperature biases in CMIP6 simulations and the role of regional vertical mixing. *Journal of Climate*, 33(17), 7523-7538.